

ULTRASONIC AND ELECTRICAL PROPERTIES OF
HYDRATE-BEARING SEDIMENTS

by

Mathias Pohl

A thesis submitted to the Faculty and the Board of Trustees of the Colorado School of Mines in partial fulfillment of the requirements for the degree of Doctor of Philosophy (Geophysics).

Golden, Colorado

Date _____

Signed: _____
Mathias Pohl

Signed: _____
Dr. Manika Prasad
Thesis Advisor

Golden, Colorado

Date _____

Signed: _____
Dr. John Bradford
Professor and
Department Head of Geophysics

ABSTRACT

There is a need to estimate the amount of gas hydrates occurring in the subsurface to establish the potential of natural gas hydrates as, for example, gas resource, geo-hazards, or climate change factors. Controlled laboratory measurements of the seismic properties of pure hydrate and hydrate-bearing sediment are critical to calibrate seismic and more importantly well-logging methods used to estimate gas hydrate accumulations. In general, the presence of hydrates is accompanied by an increase in acoustic velocity and attenuation. The stiffening effect of hydrate formation in unconsolidated sediment strongly depends on hydrate habit: hydrate formation along the grain surfaces increases velocities already at low ($S_h \sim 3\%$) hydrate saturation, whereas hydrate located in the pore space will increase velocity only at high ($S_h > 20\%$) hydrate saturation.

I measured ultrasonic P- and S-wave velocity and attenuation in pure tetrahydrofuran (THF) hydrate and THF hydrate-bearing sediment as functions of pressure and temperature. In addition, I measured complex electrical conductivity in a methane hydrate-bearing sandstone during multiple cycles of hydrate formation and dissociation. These combined measurements allow us to understand the effect of hydrate growth on geophysical properties, interactions between sediment – water – hydrate and hydrate – water interfaces, and provide a better understanding of why an increase in hydrate saturation in sediment is accompanied by an increase in wave attenuation in well log data.

The ultrasonic measurements show that presence of liquid water between hydrate grains increases attenuation in pure THF hydrates and sand-clay mixtures with varying hydrate saturation (0, 40, 60, and 80%). The observations suggest that trapped water within the hydrate causes the heightened attenuation. A comparison with laboratory data obtained using methane as a hydrate

former verifies that acoustic properties of THF hydrate-bearing sediments are comparable to the methane hydrate-bearing sediments found in nature, demonstrating that THF hydrate is an appropriate proxy for methane hydrate. After an increase in pressure from 435 to 2175psi, the loss-diagram shows that samples with various hydrate saturation (0, 40, 60, and 80%) converge to the same linear behavior; as the hydrate saturations increase, the $K_i - \mu_i$ ratios decrease, implying a change in loss mechanisms. These findings help make a better prediction on the effects of hydrate saturation in the subsurface on the sediment properties and can be used to interpret field seismic observations.

Similar to acoustic attenuation, electrical conductivity is sensitive to the existence and amount of free water. Hydrate formation results in a thin hydrate layer along the grains. The conductivity data suggest that small layers of unreacted free water are present between the thin layer of hydrate and the sediment grains. This is very important because residual water has a significant effect on wave attenuation. Hydrate formation consumes pure H_2O which, during the onset of hydrate formation, results in an increase of temperature due to the exothermic reaction. This is observed as a sudden increase in electrical conductivity. Further cooling results in the observed decrease in conductivity. The reverse effect is detected during hydrate dissociation. Combined, these two processes could be used to monitor the hydrate formation or dissociation front in the subsurface.

TABLE OF CONTENTS

ABSTRACT	iii
LIST OF FIGURES.....	viii
LIST OF TABLES	xiii
LIST OF ABBREVIATIONS	xv
LIST OF SYMBOLS	xvi
ACKNOWLEDGMENTS.....	xviii
CHAPTER 1 INTRODUCTION.....	1
1.1 Background, Motivation, and Objectives	1
1.2 Organization of Thesis.....	4
1.3 List of Publications.....	6
1.4 References	7
CHAPTER 2 ULTRASONIC ATTENUATION OF PURE THF HYDRATES	10
2.1 Abstract.....	10
2.2 Introduction	11
2.3 Experimental Setup & Procedure	13
2.4 Results	16
2.5 Discussion.....	21
2.6 Conclusions	27
2.7 Acknowledgement.....	27

2.8 References	27
CHAPTER 3 INVESTIGATING THE INFLUENCE OF CLAY CONTENT ON ULTRASONIC VELOCITIES AND ATTENUATION OF THF HYDRATE- BEARING SEDIMENT	30
3.1 Abstract.....	30
3.2 Introduction	31
3.3 Samples Used & Procedure	34
3.4 Results	41
3.4.1 Ultrasonic Velocity Measurements.....	41
3.4.2 Ultrasonic Attenuation Measurements.....	50
3.5 Discussion.....	52
3.5.1 Ultrasonic Velocities.....	52
3.5.2 Ultrasonic Attenuation.....	56
3.6 Conclusions	58
3.7 Acknowledgement.....	59
3.8 References	59
3.9 Appendix A.....	63
3.10 Appendix B.....	68
CHAPTER 4 DETECTING CEMENTATION AND POROSITY LOSS FROM A LOSS-DIAGRAM.....	72
4.1 Abstract.....	72

4.2 Introduction	72
4.3 Methodology.....	73
4.4 Results	74
4.5 Discussion.....	77
4.6 Conclusion.....	79
4.7 Acknowledgement	80
4.8 References	77
CHAPTER 5 EFFECT OF METHANE HYDRATE FORMATION ON COMPLEX CONDUCTIVITY MEASUREMENTS IN SANDSTONE	82
5.1 Abstract.....	82
5.2 Introduction	83
5.3 Background – Low-Frequency Complex Conductivity Principles.....	86
5.4 Experimental Setup and Procedure.....	88
5.5 Results	90
5.6 Discussion.....	93
5.7 Conclusions	103
5.8 Acknowledgement	104
5.9 References	104
CHAPTER 6 CONCLUSIONS.....	109

LIST OF FIGURES

Figure 1-1	“Relationship between gas hydrate saturation estimated from the resistivity log (quick look Archie) and (a) sonic attenuation and (b) sonic velocity. Solid circles are compressional values (Q_p^{-1} and V_p), open symbols are shear data (Q_s^{-1} and V_s). Regression coefficients for the least squares linear fits are in brackets.” from Guerin & Goldberg (2002)	4
Figure 2-1	A) Schematic of sample B) Photograph showing the transducer and receiver holders. The wires extending from the sample are clipped before measurements and sealed with soft epoxy. Tubing is sealed against transducer and receiver using a metal wire.	14
Figure 2-2	Raw waveforms of the first cycles of the P-waves in aluminum standard (black), frozen sample (red), only hydrate-bearing (green), and liquid (blue). The aluminum and liquid samples were measured at room temperature ($\sim 25\text{ }^\circ\text{C}$), Hydrate samples at $1\text{ }^\circ\text{C}$ and frozen samples at $-10\text{ }^\circ\text{C}$. All measurements were conducted at atmospheric pressure. Multiple lines at the same conditions mark repeat measurements. Note that the amplitude of the waveform through aluminum is the smallest of all the measured samples due to transducer design. These transducers are impedance matched to measure low impedance materials such as unconsolidated sands. Consequently, the high impedance contrast between the PEEK end caps and the aluminum causes parts of the signal to reflect off the aluminum instead of being transmitted through it.....	18
Figure 2-3	Frequency spectra of waveforms shown in Figure 2-2 for different samples to ensure repeatability. A) liquid sample B) hydrate sample C) frozen sample D) Comparison of Liquid, Hydrate, and Frozen frequencies. Time progression of the experiments were day 0 = Liquid data, day 3 = Hydrate data, and day 4 = Frozen data.	19
Figure 2-4	Overview of the calculated attenuation Q for the liquid, hydrate and frozen samples. Lines represent the time elapsed between measurements. Blue symbols correspond to the first set of measurements, green symbols to the second set of measurements, and the red symbols to the third set of measurements.	20
Figure 2-5	A) Raw data for a sample containing “100%” THF hydrate. Continuous measurements show an increase in amplitude and longer relaxation times which are a result of the dissociation of the hydrate and therefore the availability of more free hydrogen. B) Inversion of a sample containing “100%” THF hydrate. Comparison of the First Run at $1\text{ }^\circ\text{C}$ with a measurement performed after hydrates	

were completely dissolved. Inverted signals below an amplitude of 0.01 should not be considered since they may result from inversion artifacts. C) First arrivals for the sample containing only hydrates (green) which corresponds to the first measurement of the NMR and the first arrival of the sample in the liquid stage (blue) which corresponds to the 13th measurement of the NMR.....25

Figure 2-6 Red line shows the relaxation time for a sample containing “100%” THF Hydrate at -10 °C (frozen), green line shows the relaxation time for a sample containing “100%” THF hydrate at 1 °C (hydrate), and blue line shows the relaxation time for a sample containing THF-water mixture (liquid). Note: a subtle difference in relaxation time of Frozen and Hydrate sample.....26

Figure 3-1 Micro X-Ray CT images of (a) dry Ottawa sand, (b) dry Ottawa sand mixed with 30 wt% clay, (c) fluid saturated Ottawa sand with 30 wt% clay, and (d) dried Ottawa sand mixed with 30 wt% clay38

Figure 3-2 Experimental setup for ultrasonic velocity measurements in hydrate-bearing sediments under reservoir conditions (after Rydzy et al., 2013).35

Figure 3-3 a) Example of a collected S-waveform through a clean quartz sand sample saturated with liquid THF-water b) Example of a collected S-waveform through aluminum standard c) Normalized frequency content of the same S-wave (a) in blue and aluminum standard (b) in green, d) ratio between frequency content of aluminum and sample, the slope between the two black bars is γ40

Figure 3-4 P- and S-wave velocities before and after hydrate formation for different hydrate saturation (0, 40, 60, and 80%) and at different differential pressures (435 and 2175 psi) in pure sand samples. Each sample was first measured at 435 psi differential pressure and at room temperatures (Stage I). Stage II was measured with hydrates in the sediment, while Stages I and III were measured in the host sediment before and after hydrate formation, respectively.43

Figure 3-5 Vp-Vs ratio changes before and after hydrate formation for different hydrate saturation (0%, 40% (green triangles), 60% (red circles), and 80% (blue squares)) and at different confining pressures (435 psi and 2175 psi). Samples are considered consolidated if they fall below the dotted line (Vp-Vs ratio < 2). Note that the stages mentioned here are the same as in Figure 3-4.44

Figure 3-6 Compressional (squares) and shear (circles) wave velocities as a function of porosity for samples with 0, 10, and 30 wt% clay before and after THF hydrate formation for 80% THF hydrate saturation. Percentages given are a proportional change in velocity.....46

Figure 3-7 Compressional (squares) and shear (circles) wave velocities as a function of porosity for samples with 0, 10, and 30 wt% clay before and after THF hydrate formation for 60% THF hydrate saturation. Percentages given are a proportional change in velocity.....47

Figure 3-8 Compressional (squares) and shear (circles) wave velocities as a function of porosity for samples with 0, 10, and 30 wt% clay before and after THF hydrate formation for 40% THF hydrate saturation. Percentages given are a proportional change in velocity.....48

Figure 3-9 Vp-Vs ratios for samples containing 30, 10 and 0 wt% of clay for samples containing:49

Figure 3-10 Qp and Qs values for clean sand samples containing 80 (a), 60 (b), and 40% (c) hydrate saturation. For all three plots, the numbers on the x-axis correspond to the stages:51

Figure 3-11 Seismic losses (Qs and Qp) in sands containing various amounts of clay (0, 10, and 30 wt%) before hydrate formation (yellow squares) and after hydrate dissociation (yellow triangles). Note the significant difference between the sands without hydrates (yellow symbols) and with 80% hydrate saturation (blue symbols).53

Figure B-1 Collected and overlaid waveforms for two separate samples with 70 wt% Ottawa Sand and 30 wt% clay. a & b – fluid saturated samples at 535 psi, c & d – samples containing 40% hydrate at 535 psi, e & f – samples containing 40% hydrate at elevated pressure (2275 psi), g & h – samples containing 40% hydrate after reducing pressures back to 535 psi, i & j – samples after hydrate dissociation at 535 psi70

Figure B-2 Comparison for ultrasonic raw p-waveforms for clean sand (a,c,e) and sand with 30 wt% clay (b,d,f) containing 40% THF hydrate saturation. a, c, and e contain three raw waveforms each (blue, green, red). b, d, and f contain two waveforms each (blue and green). Clean sand samples with 40% THF hydrate saturation do not show a visible change in their waveforms after elevated pressures (comparing a and e), whereas samples with 30 wt% clay show a visible decrease in amplitude after elevated confining pressures (comparing b and f)71

Figure 4-1 Comparisons of loss mechanisms in sands with varying hydrate concentrations. Modeled ratios of shear (μ_1) to bulk (K_1) losses are shown by solid gray lines, while symbols depict data. The saturated sands show high bulk losses ($K_1=15-20 \mu_1$). Hydrate presence changes and increases shear losses proportionally to hydrate

	saturation. Percentages indicate hydrate saturation. Sources: i: Prasad and Meissner (1992), ii: Priest et al., 2006, iii: Priest et al., 2009, iv: Guerin and Goldberg (2002), v: this study. The gray shaded box indicates the zoomed in part shown in Figure 4-2.	75
Figure 4-2	Loss Diagram with THF-water mixture samples (grey box from Figure 4-1): Before THF hydrate formation (blue circles), THF hydrate-bearing sands at 535 psi (red circles) and 2275 psi (purple stars) confining pressure. The purple line is a linear regression for the purple stars. Grey lines show the relationship between K_i and μ_i . Yellow triangles are fully water saturated Berea Sandstone data (Mapeli, 2018).	76
Figure 5-1	(a) Schematic of the sandstone sample with current electrodes on the top and the bottom and potential electrodes in the middle of the sample. (b) Schematic of the experimental setup (courtesy of Ahmad Majid).	90
Figure 5-2	(a) Overview of the measured electrical conductivities for the entire duration of the test. Letters are used in the following figures and displayed here to mark when changes occurred. I marks the event of hydrate formation, II marks the freezing of the hydrate-bearing sample, III marks the thawing of the ice in the ice-hydrate-bearing sample, and IV marks the hydrate dissociation event. Different colors denote different frequencies. The data displayed ranges from 1.5 Hz–12000 Hz. (b) Schematic of temperature and pressure changes during the duration of the experiment.	94
Figure 5-3	(a) Schematic of temperature and pressure changes during Cycle I. (b) Real (blue) and Imaginary (black) part of the conductivity measurements for the first complete measurement cycle, displayed for a single frequency (94 Hz). The arrows mark distinct stages: Arrow I – Cooling Stage with the onset of hydrate formation, Arrow II – Freezing Stage with ice formation, Arrow III – Thawing Stage, Arrow IV – Warming Stage with the onset of hydrate dissociation. Zoomed in plots for I Cooling Stage (c), II Freezing Stage (d), III Thawing Stage (e), and IV Warming Stage for Real (blue) and Imaginary (black) conductivity at 94Hz. ...	95
Figure 5-4	(a) Schematic of temperature and pressure changes during Cycle I. Grey boxes and arrows point at the four stages that are displayed in b, c, d, and e. A comparison between higher (6000 Hz for real conductivity (blue), 375 Hz for imaginary conductivity (green)), and lower (1.5 Hz for both real and imaginary conductivity (brown)) frequencies is displayed for (b) I Cooling Stage, (c) II Freezing Stage, (d) III Thawing Stage, and (e) IV Warming Stage.	96
Figure 5-5	(a) Real part of the conductivity over time and frequency for the initial hydrate formation. The amplitude in the electrical conductivity is frequency dependent	

during hydrate formation, and the formation process can be detected for up to 30 min for higher frequencies. Lower frequencies stop seeing hydrate formation after 15 min. (b) Imaginary part of the conductivity over time and the frequency for the initial hydrate formation. Conductivity values drop quickly once hydrate formation starts. The solid black line marks the onset of hydrate formation. Dotted lines and letters correspond to data plotted in (c) and (d). (c) and (d) show conductivity and quadrature conductivity values, respectively, over a range of frequencies before, during, and after hydrate formation.97

Figure 5-6 Real part (a) and Imaginary part (b) of the conductivity over time and frequency for the IV Warming Stage (hydrate dissociation). The amplitude in electrical conductivity is frequency dependent during hydrate dissociation, and the dissociation process can be detected for up to 170 min. (c) and (d) show conductivity and quadrature conductivity values, respectively, over a range of frequencies before, during, and after hydrate dissociation (A, B, and C correspond to A, B, and C in (a) and (b)). A peak in the imaginary conductivity (d) at 23 Hz can be observed during hydrate dissociation (B).....98

LIST OF TABLES

Table 2-1	Impedance calculations.....	15
Table 2-2	Summary of calculated velocities, peak frequencies, and peak-to-peak amplitudes for all the samples.....	22
Table 3-1	Overview of ultrasonic velocity measurements on various sediments from the literature.....	33
Table 3-2	Water – THF mixtures used to achieve 40, 60, and 80% hydrate saturation in the sediments	34
Table 3-3	Overview of the temperature and pressure conditions for different stages during the experiments.....	37
Table 3-4	Overview of the number of measurements made on samples for the various cases discussed here.	37
Table A-1	Summary of compressional wave velocities with varying clay content and 80% THF hydrate saturation.....	63
Table A-2	Summary of shear wave velocities with varying clay content and 80% THF hydrate saturation	63
Table A-3	Summary for V_p - V_s ratio with varying clay content and 80% THF hydrate saturation	63
Table A-4	Summary of compressional wave velocities with varying clay content and 60% THF hydrate saturation.....	64
Table A-5	Summary of shear wave velocities with varying clay content and 60% THF hydrate saturation	64
Table A-6	Summary for V_p - V_s ratio with varying clay content and 60% THF hydrate saturation	64

Table A-7 Summary of compressional wave velocities with varying clay content and 40% THF hydrate saturation.....65

Table A-8 Summary of shear wave velocities with varying clay content and 40% hydrate THF saturation.....65

Table A-9 Summary for Vp-Vs ratios with varying clay content and 40% THF hydrate saturation65

Table A-10 Quality factor Qp for 80% THF hydrate saturation with varying clay content.66

Table A-11 Quality factor Qs for 80% THF hydrate saturation with varying clay content.66

Table A-12 Quality factor Qp for 60% THF hydrate saturation with varying clay content.66

Table A-13 Quality factor Qs for 60% hydrate saturation with varying clay content.....67

Table A-14 Quality factor Qp for 40% THF hydrate saturation with varying clay content.67

Table A-15 Quality factor Qs for 40% THF hydrate saturation with varying clay content.67

LIST OF ABBREVIATIONS

BSR	Bottom Simulating Reflector
BHSZ.....	Bottom of Hydrate Stability Zone
GHSZ	Gas Hydrate Stability Zone
VP.....	Compressional Wave Velocity
P-wave.....	Compressional Wave Velocity
S-wave.....	Shear Wave Velocity
DI.....	Deionized
THF	Tetrahydrofuran
NMR.....	Nuclear Magnetic Resonance
PEEK.....	Polyether Ether Ketone
IP	Induced Polarization
CR.....	Complex Resistivity
CC.....	Complex Conductivity
SIP	Spectral Induced Polarization
ICP-MS.....	Inductively Coupled Plasma Mass Spectrometry
CSEM	Controlled Source Electromagnetics

LIST OF SYMBOLS

V_p	Compressional Wave Velocity
V_s	Shear Wave Velocity
Q	Quality Factor
Q^{-1}	Attenuation
K	Bulk Modulus
μ	Shear Modulus
K_i	Bulk Loss
μ_i	Shear Loss
Q_p	Compressional Quality Factor
Q_s	Shear Quality Factor
π	pi
l	Length
γ	Slope of the Frequency Ratios
v	Ultrasonic Velocities
ρ	Electrical Resistivity
σ	Electrical Conductivity
R	Resistance
C	Conductance
G	Geometric Factor

S_w	Water Saturation
S_h	Hydrate Saturation
n	Saturation Exponent
F	Formation Factor
σ_w	Water Conductivity
σ	Bulk Conductivity
a	Tortuosity Factor
ϕ	Porosity
m	Cementation Factor
σ'	Real Part of Conductivity, In-Phase Conductivity
σ''	Imaginary Part of Conductivity, Quadrature Conductivity
φ	Phase Angle
i	Imaginary Number

ACKNOWLEDGMENTS

It is a pleasure to thank the many people who made this thesis possible.

First and foremost, I would like to express my sincere gratitude to Prof. Michael Lee Batzle, who, although no longer with us, had a major impact on my life and therefore on my Ph.D. study and research. His patience, motivation, enthusiasm, and immense knowledge helped to overcome the daily struggles of breaking semiconductor gages on a regular basis. I could not have imagined having a better advisor and mentor for this thesis study.

I would also like to express my deep appreciation to Manika Prasad who stepped in during one of the darkest times a student can possibly go through. Thank you for taking me in and thank you for giving me the freedom to research in my own way.

I feel privileged to have worked and interacted with all the members of my thesis committee: Azra Tutuncu, Carolyn Koh, Timothy Collett, William Waite, and Brandon Dugan.

Also, I would like to thank the Department of Energy for providing the financial support for this project, Award Number DE-FE 0009963. In addition, this study was funded by the DHI/Fluids consortium.

Thanks to the CSM Geophysics Department, past and present Rock Abusers, as well as Michelle Szobody for creating a friendly work environment.

I would also like to thank Kurt Peter Livo for his encouragement and insightful comments, ahhh who am I kidding, thanks for all the “complaining together” and philosophizing about the “why are we doing this?”.

Sincere thanks also go to all the friends I made along the way. JJ and Carolyne for helping me get through the last stretch of my Ph.D. Patrick, for always being ready to go on an adventure.

I would also like to thank my wife, Carolyn, who made countless sacrifices to help me get to this point. Thank you for all your love and support.

Last but not the least; I would like to thank my family: my parents Marion Pohl and Thomas Pohl for always believing in me. I would also like to show my gratitude to my grandma who showed great support over the last several years.

The difference between screwing around
and science, is writing it down.

Adam Savage

CHAPTER 1

INTRODUCTION

1.1 Background, Motivation, and Objectives

Gas hydrates are ice-like substances consisting of water cages and encapsulated guest molecules, in nature most commonly methane molecules (CH_4) (Sloan & Koh, 2008), in the following “hydrate” will refer to methane hydrate. Their high energy density (A unit volume of hydrate contains up to 164 volumes of methane gas, at standard temperature and pressure) and their widespread occurrence over the globe makes them a broadly available potential natural gas resource. Gas hydrates are stable at low temperatures and elevated pressures. Other requirements for hydrate formation that need to be fulfilled are the availability of gas (free or dissolved) and water. Such conditions can be found in permafrost regions, continental margins, and inland seas (e.g., the Black Sea (Korasakov et al., 1991)) and freshwater lakes (e.g., Lake Baikal (Khlystov et al., 2013)).

To allow the production of natural gas stored in hydrates, it is necessary to locate and assess these reservoirs. Geophysical techniques such as seismic surveys, coupled with drilling and well logging can help evaluate hydrate reservoirs. In seismic surveys, the so-called bottom simulating reflector (BSR) can indicate the presence of hydrates. The BSR is a strong reverse –polarity seismic reflection which resembles the shape of the ocean bottom and is caused by the high impedance contrast between the hydrate-bearing sediments and the free gas below (Hyndman and Spence, 1992; Bünz et al., 2003). It is also characterized by a phase inversion relative to the seafloor reflection event, and it crosscuts the local seismic stratigraphy (Berndt et al., 2004). The BSR is thought to represent the bottom of the hydrate stability zone (Hyndman et. al. 1992). The gas

hydrate stability zone (GHSZ) above the BSR shows strong attenuation in seismic images (so-called blanking), which results in a reduction of seismic amplitudes. Although the BSR indicates the existence of hydrates, it does not allow any conclusions about the hydrate saturation in the sediment. Thus, we need to calibrate seismic data by using rock physics models guided by laboratory experiments that describe how hydrate and sediment interact and how hydrate formation affects geophysical signals (e.g., Waite et al., 2004, Yun et al., 2005, Rydzy, 2013).

The formation of a hydrate from the free or dissolved gas phase affects the location of hydrate nucleation in the pore space. Hydrates formed out of the dissolved gas phase develop in the pore space away from the grains (Tohidi et al., 2009) whereas hydrates formed from the free gas phase nucleate preferentially at the water-gas interface. Priest et al. (2006) showed experimentally that acoustic velocities increased significantly in samples with a limited supply of water as hydrates cement the grains. This method is called the excess gas method. On the other hand, if the gas supply was limited, it was found that velocities were much less sensitive after hydrate formation (Priest et al., 2009), this is called excess water method. The excess water method results in hydrates formation away from the grains in the pore space.

In nature, gas hydrates can occur in various forms in sediments; finely disseminated between grains, in shape of nodules, veins or layers, and as massive hydrate outcrops exposed on the seafloor (Boswell and Collett, 2006). Characterization of these natural materials is challenging. On the one hand, it is costly and technically difficult to obtain samples from the field because the original characteristics can easily be disturbed by pressure and temperature changes. On the other hand, making hydrate samples in the laboratory to mimic natural formations is also challenging (Katsuki et al., 2007). Due to the low solubility of methane in water, the formation of gas hydrates in the laboratory would require weeks to even months to deliver sufficient methane gas for hydrate

accumulation in sediments (Spangenberg et al. 2005). Also, creating a homogeneous hydrate distribution within the sample is difficult (Yang et al., 2008). To overcome these difficulties, synthesized hydrates from water-soluble proxies such as tetrahydrofuran (THF) (Pearson et al., 1986, Collett, 2000, Kunerth et al., 2001, Yun et al., 2005, Lee et al., 2010, Rydzy, 2013) or carbon dioxide (Katsuki et al., 2006) are used.

To evaluate gas hydrate saturation from seismic data, the properties of pure gas hydrate, as well as gas hydrate-bearing sediment, need to be known. Therefore as part of this thesis, I first investigate the ultrasonic attenuation properties of pure THF-hydrates. The results will help understand why increasing hydrate saturation in sediment is accompanied by an increase in wave attenuation in well log data (Figure 1-1). In the second part of my thesis, I build on the results from pure hydrate. I present ultrasonic velocity and attenuation measurements on unconsolidated clean sand and sand-clay mixtures to determine how THF hydrate formation changes the properties of the sediment. I then compare my ultrasonic velocity and attenuation data with laboratory data obtained using methane as a hydrate former. This comparison ensures that acoustic properties of THF hydrate-bearing sediments are comparable to methane hydrate-bearing sediments found in nature. The similarity between the two hydrate formers demonstrates that THF is an appropriate proxy for methane hydrates. The acoustic data are presented in a so-called Loss-Diagram to distinguish between shear and bulk loss mechanisms. The findings help predict how hydrate saturation in the subsurface affects the sediment properties and could be used to interpret seismic field observations. In Chapter 5, low-frequency electrical conductivity responses during methane hydrate formation and dissociation in sandstone are analyzed. Additional experiments where the methane hydrate-bearing sandstone was exposed to sub-cooling temperature ($< 0^{\circ}\text{C}$) were conducted to study if all of the available water was converted into hydrates. Both the acoustic

attenuation and electrical conductivity, are sensitive to the presence of water. Therefore, knowing the residual amount of water enables us to make a better prediction about mechanical and electrical properties of hydrate-bearing sediments.

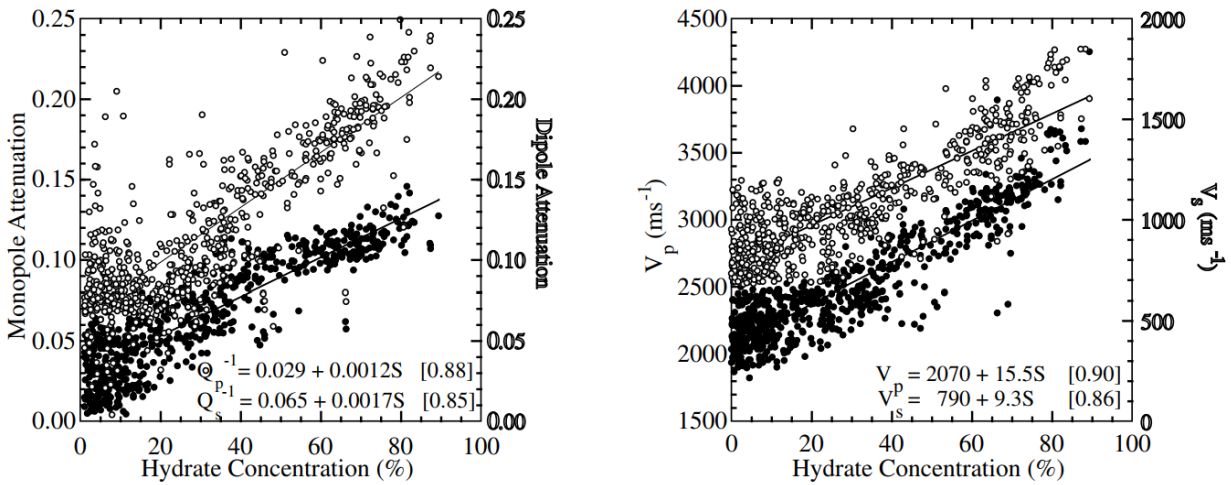


Figure 1-1 “Relationship between gas hydrate saturation estimated from the resistivity log (quick look Archie) and (a) sonic attenuation and (b) sonic velocity. Solid circles are compressional values (Q_p^{-1} and V_p), open symbols are shear data (Q_s^{-1} and V_s). Regression coefficients for the least squares linear fits are in brackets.” from Guerin & Goldberg (2002)

1.2 Organization of Thesis

This thesis consists of six chapters. A brief explanation of each chapter is given as follows:

Chapter 1: presents a general introduction to thesis motivations, objectives, problems to be addressed, followed by the structure of the thesis and a list of publications and references.

Chapter 2: concentrates on acoustic wave attenuation properties for pure THF-hydrates. Ultrasonic velocities were used in conjunction with the spectral ratio method to calculate ultrasonic attenuation. The results help to understand the attenuation increase in hydrate-bearing sediments.

Chapter 2 is published in *EAGE's Geophysical Prospecting* (Pohl, M., Prasad, M., Batzle, M.[†], Ultrasonic attenuation of pure THF hydrates).

Chapter 3: focuses on the experimental study of velocity and attenuation changes in unconsolidated sands and sand-clay mixtures before and after THF hydrate formation as functions of hydrate saturation and pressure. Chapter 3 will be submitted to *AGU's Journal of Geophysical Research* (Pohl, M., Prasad, M., Batzle, M.[†], Investigating the influence of clay content on ultrasonic velocities and attenuation of the THF hydrate-bearing sediment).

Chapter 4: This chapter compares velocity and attenuation results presented in Chapter 3 with laboratory and well-log data on methane hydrate-bearing sediments obtained from the literature. Chapter 4 will be submitted to *Science* (Pohl, M. and Prasad, M., Detecting Cementation and Porosity Loss from a Loss-Diagram).

Chapter 5: presents a study on continuous complex conductivity measurements in a hydrate saturated Castlegate sandstone during hydrate formation. Our conductivity data document the combined effects of ionic exclusion, water depleting, and exothermic reactions during hydrate formation and dilution, water saturation increase, and endothermic reactions during hydrate dissociation. Chapter 5 will be submitted to *AGU's Journal of Geophysical Research* (Pohl, M., Mapeli, C. and Prasad, M., Effect of methane hydrate formation on complex conductivity measurements in a sandstone).

Chapter 6: presents a conclusion of each chapter of this thesis.

1.3 List of Publications

In preparation for peer-review journal:

1. Pohl, M., Prasad, M., Batzle, M.[†], Investigating the influence of clay content on ultrasonic velocities and attenuation of the THF hydrate-bearing sediment. (Target Journal: *Journal of Geophysical Research*)
2. Pohl, M. and Prasad, M., Detecting Cementation and Porosity Loss from a Loss-Diagram. (Target Journal: *Science*)
3. Pohl, M., Mapeli, C. and Prasad, M., Effect of methane hydrate formation on complex conductivity measurements in a sandstone (Target Journal: *Journal of Geophysical Research*)

Published in peer-review journal:

4. Pohl, M., Prasad, M. and Batzle, M. L. (2017), Ultrasonic attenuation of pure THF hydrates. *Geophysical Prospecting*, doi: 10.1111/1365-2478.12534

Conference proceedings and abstracts:

1. Pohl, M., Mapeli, C., and Prasad, M., Long-Term Effects of Hydrate Formation on Complex Resistivity in a Sandstone, Gordon Research Conference – Natural Gas Hydrate Systems, Galveston, TX, USA, 24th February – 2nd March 2018.
2. Pohl, M., Schindler, M., Livo, K., and Prasad, M., Understanding Seismic and Petrophysical Indications of Pure Hydrates and Hydrate-Bearing Sediments, 9th International Conference on Gas Hydrates 2017, Denver, CO, USA, 25th – 30th June 2017.
3. Pohl, M., Batzle, M., Ultrasonic Attenuation of Pure THF-Hydrates, 3rd International Workshop of Rock Physics, 2015, Perth, Western Australia, Australia, 13th – 17th April 2015.

4. Pohl, M., Rydzy, M., and Batzle, M., Investigating the Influence of Clay Content on Ultrasonic velocities of THF Hydrate-Bearing Sediments, Gordon Research Conference – Natural Gas Hydrate Systems, Galveston, TX, USA, 23rd – 28th March 2014.
5. Pohl, M., Rydzy, M., and Batzle, M., Low frequency and ultrasonic velocity measurements of THF hydrate-bearing Foxhill Sandstone, 2nd International Workshop of Rock Physics, 2013, Southampton, UK, 4th – 9th August 2013.

1.4 References

- Berndt, C., S. Bünz, T. Clayton, J. Mienert, and M. Saunders (2004), Seismic character of bottom simulating reflectors: Examples from the mid-Norwegian margin, *Mar. Pet. Geol.*, 21(6), 723–733, doi:10.1016/j.marpetgeo.2004.02.003.
- Boswell, R. and Collett, T.S., “The Gas Hydrate Resource Pyramid,” *Fire in the Ice, Methane Hydrate R&D Program Newsletter*, Fall 2006.
- Bünz, S., Mienert, J., and Berndt, C., 2003. Geological controls on the Storegga gas-hydrate system of the mid-Norwegian continental margin. *Earth and Planetary Science Letters*, 209(3–4), 291–307.
- Collett, T.S., 2000, Quantitative well-log analysis of in-situ gas hydrates, Ph.D. Thesis, Colorado School of Mines, Golden, Colorado
- Guerin, G., and Goldberg, D., 2002. Sonic waveform attenuation in gas hydrate-bearing sediments from the Mallik 2L-38 research well, MacKenzie Delta, Canada. *J. Geophys. Res.*, 107:2088. doi:10.1029/2001JB000556
- Hyndman, R. D., and Spence, G. D., 1992. A seismic study of methane hydrate marine bottom simulating reflectors. *Journal of Geophysical Research – Solid Earth*, 97, 6683–6698.
- Hyndman, R.D., Foucher, J.P., Yamamoto, M., Fisher, A., and Shipboard Scientific Party of Ocean Drilling Program Leg 131, 1992, Deep sea bottom-simulating-reflectors: Calibration of the base of the hydrate stability field as used for heat flow estimates: *Earth and Planetary Science Letters*, v. 109, p. 289-301.

- Katsuki, D., R. Ohmura, T. Ebinuma, and H. Narita (2006), Formation, growth, and aging of clathrate hydrate crystals in a porous medium, *Philos. Mag.*, 86(12), 1753–1761, doi:10.1080/14786430500509062.
- Khlystov O. M., De Batist M., Shoji H., Hachikubo A., Nishio S., Naudts L. (2013). Gas hydrate of lake baikal: discovery and varieties. *J. Asian Earth Sci.* 62 162–166. 10.1016/j.jseaes.2012.03.009
- Korsakov, O.D., Stupak, S.N. and Byakov, Y.A., (1991). Chernomorskiye gazogidraty; netraditsionnyy vid uglevodorodnogo syr'ya (Black Sea gas-hydrates as a nontraditional kind of hydrocarbon stock). *Geofizicheskiy Zhurnal*, 31(5): 67-75.
- Kunerth, D.C., D.M. Weinberg, J.W. Rector III, C.L. Scott, and J.T. Johnson, 2001, *Journal of Seismic Exploration* 9, 337
- Pearson, C., Murphy, J. and Hermes, R. (1986). Acoustic and resistivity measurements on rock samples containing tetrahydrofuran hydrates: laboratory analogues to natural gas hydrate deposits. *Journal of Geophysical Research* 91: doi: 10.1029/JB080i014p14132. ISSN: 0148-0227.
- Pohl, M., Prasad, M. and Batzle, M. L. (2017), Ultrasonic attenuation of pure THF hydrates. *Geophysical Prospecting*, doi: 10.1111/1365-2478.12534
- Priest J.A, A.I. Best, C.R.I. Clayton (2006), “Attenuation of seismic waves in methane gas hydrate-bearing sand *Geophys. J. Int.*, 164, pp. 149-159, 10.1111/j.1365-246X.2005.02831.X
- Priest, J.A., E.V.L. Rees, and C.R.I. Clayton (2009), “Influence of gas hydrate morphology on the seismic velocities of sands”, *Journal of Geophysical Research*, 114, B1120
- Rydzy, M. B. (2013) “Effect of Hydrate Formation on the Elastic Properties of Unconsolidated Sands”. Ph.D. Thesis, Colorado School of Mines, Golden, CO
- Sloan, E. D. & Koh, C. A. (2007), *Clathrate Hydrates of Natural Gases*. 3rd ed., CRC Press, Taylor & Francis Group, Boca Raton, FL
- Spangenberg, E., J. Kulenkampff, R. Naumann, and J. Erzinger (2005), Pore space hydrate formation in a glass bead sample from methane dissolved in water, *Geophys. Res. Lett.*, 32, L24301, doi:10.1029/2005GL024107.
- Tohidi, B., R. Anderson, and B. Webber (2009), “Capillary controls on gas hydrate growth and dissociation in synthetic and natural porous media: PVT, NMR, Neutron Diffraction and SANS”, Grant Report, EPSRC: EP/D052556/1

- Waite, W. F., Winters, W. J., Mason, D. H. (2004). "Methane Hydrate Formation in Partially Water-Saturated Ottawa Sand." *American Mineralogist*, 89: 1221-1227
- Yang, J., B. Tohidi, and A. Chapoy (2008), Impact of sedimentary mineralogy on the geophysical and geomechanical properties of hydrate-bearing sediments, paper presented at the Sixth International Conference on Gas Hydrates (ICGH 2008), Vancouver, Can., 6–10 Jul.
- Yun, T. S., Francisca, F. M., Santamarina, J. C., Ruppel, C (2005). "Compressional and Shear Wave Velocities in Uncemented Sediment Containing Gas Hydrate." *Geophysical Research Letters*, Vol. 32, L10609, doi:10.1029/2005GL022607

CHAPTER 2

ULTRASONIC ATTENUATION OF PURE THF HYDRATES

A paper published in *Geophysical Prospecting*

Mathias Pohl^{*a}, Manika Prasad^a, Michael L. Batzle^{a†}

2.1 Abstract

Improved estimates of the amount of subsurface gas hydrates are needed for natural resource, geohazard, and climate impact assessments. To evaluate gas hydrate saturation from seismic methods, the properties of pure gas hydrates need to be known. While the properties of sediments, specifically sands, and hydrate-bearing sediments are well studied, the properties of pure hydrates are largely unknown. Hence, we present laboratory ultrasonic P-wave velocity and attenuation measurements on pure tetrahydrofuran (THF) hydrates as they form with reducing temperatures from 25 °C to 1 °C under atmospheric pressure conditions. THF hydrates, with structure II symmetry, are considered as proxies for the structure I methane hydrates because both have similar effects on elastic properties of hydrate-bearing sediments. We find that although velocity increased, the waveform frequency content and amplitude decreased after the hydrate formation reaction was complete, indicating an increase in P-wave attenuation after hydrate formation. When the THF hydrate was cooled below the freezing point of water, velocity and quality factor increased. Nuclear Magnetic Resonance results indicate the presence of liquid water between hydrate grains most likely between hydrate grains most likely causes heightened attenuation in THF hydrates in the

*Primary author and editor.

Corresponding author. Direct correspondence to mpohl@mines.edu.

^aDepartment of Geophysics, Colorado School of Mines, Golden, CO 80401, USA

“pure hydrate” samples above the water freezing point, but none below. The presence of above the freezing point of water. In naturally occurring hydrates, a similarly high attenuation might relate to the presence of water.

2.2 Introduction

Gas hydrates are ice-like crystalline solids that entrap guest molecules (e.g., methane) in water cages (Sloan & Koh, 2007). Natural gas hydrates are detected by an increase in seismic velocities. An increase in the amount of hydrates in the pore space reduces porosity and increases elastic moduli of the solid frame (Dvorkin and Uden, 2004). Although velocity increase in stiffer rocks is generally accompanied by a decrease in attenuation (Klimentos & McCann, 1990, Prasad and Meissner, 1992, Koesoemadinata and McMechan, 2001), a velocity increase with increasing hydrate saturation is accompanied by an increase in attenuation (Wood, 2000; Guerin and Goldberg, 2002; Pratt et al., 2003, Suzuki and Matsuhima, 2013). Prasad and Dvorkin (2004) have reported an increase in velocity and attenuation after formation of ice; after maintaining the ice at freezing temperatures reduces attenuation with time accompanied by a minor increase in velocity. Dvorkin and Uden (2004) postulate that the increased attenuation is caused by elastic heterogeneity after hydrate formation that encourages pore-fluid crossflow between stiffer and more compliant areas in the rock or hydrate. However, there is little experimental documentation of the reasons for the attenuation behavior in pure hydrates.

Previous work focused on elastic properties of water - hydrate systems (Waite et al., 2000, Helgerud et al., 2009). The elastic and anelastic properties of natural hydrate systems (sand - water - hydrate) have also been documented (Lee and Collett, 2001, Yun et al., 2005, Priest et al., 2006, Best et al., 2013). Best et al. (2013) speculate that their observed higher attenuation in hydrate-

bearing sediments might relate to micropores. However, this assumption implies that attenuation is mainly due to the presence of an interface between sand and hydrate grains and further, that pure hydrates themselves do not attenuate seismic waves. Direct measurements are needed to help explain this and other driving factors for attenuation. To explain the observed attenuation in natural hydrate systems (e.g., Guerin and Goldberg, 2002), we need to distinguish between attenuation due to the end members (sand and hydrates) from the attenuation arising from the interactions between the components. While attenuation in sands has been studied (Hamilton, 1972, Prasad and Meissner, 1992, Liu et al., 2001, and Wang and Santamaria, 2007), the intrinsic attenuation in pure hydrates has been largely ignored. Understanding attenuation in hydrate-bearing sediments is important to distinguish between seismic - blanking caused by reverberations as opposed to small amplitudes and loss of higher frequencies due to attenuation.

Our experiments were designed to quantify the attenuation as a function of hydrate saturation and to explore the attenuation mechanisms. We performed ultrasonic pulse-transmission measurements on pure tetrahydrofuran (THF) hydrates. THF was chosen because of its stoichiometric relationship with water. For example, a mixture of 19 wt% THF and 81 wt% water should result in a 100% pure THF hydrate (Makino et al., 2005). Further, since the THF hydrate stability temperature lies above the freezing point of water, any residual, unreacted water in the system should be present in a liquid phase and be detectable by low-field NMR experiments. Our results for the attenuation of THF hydrates should be similar to those of natural methane hydrates and ice due to their similarity in mechanical properties (Sloan and Koh, 2008).

2.3 Experimental Setup & Procedure

We used the ultrasonic pulse-transmission technique and nuclear magnetic resonance (NMR) to study and characterize our samples.

Ultrasonic Measurements:

To perform repeatable and reliable experiments, we designed a sample holder that allowed us to record ultrasonic waves propagating in fluids (Figure 2-1). The sample holder consists of Tygon® tubing to contain the samples. The tubing was sealed on each end with PEEK® end caps that contained fluid lines for fluid injection as well as piezoelectric crystals (nominal frequency = 500 kHz) to transmit and receive acoustic waves. The PEEK end caps were used to have a better impedance match between transducer and sample (Table 2-1). The separation between the PEEK end caps was kept constant at 2 cm by steel wires threaded through the Tygon tubing. Compliant epoxy (EP 1121) is used to encase the sample holder to prevent fluid exchange along the wires. The sample sizes were selected such that we had more than 1.5 wavelengths through the sample. To guarantee repeatability, we performed three experiments on three different samples with same THF water ratios. In the first experiment, we measured acoustic signals as functions of temperature from ~ 25 °C to -10 °C in 1 °C temperature steps. Since this experiment showed that the waveforms and velocities only changed at specific temperatures, the second and third experiments were made at discrete temperatures where maximum change was observed (~ 25 °C; 1 °C; and -10 °C).

We measured six different sized aluminum cylinders to test the accuracy of our ultrasonic velocity measurements. The slope of the length over travel time is the velocity of the measured material. In our experiment, we calculated a velocity for aluminum of 6391 m/s which is within 1.1% of literature values (6320 m/s, Molotovo et al., 1960). In addition to benchmarking, these

experiments with aluminum were used to determine the system delay time that needs to be taken into account when calculating the velocities for the type of transducers that were being used. We also calculated the temperature dependence of our transducers by placing the transducers against one another and recording the changes in arrival times with changes in temperatures.

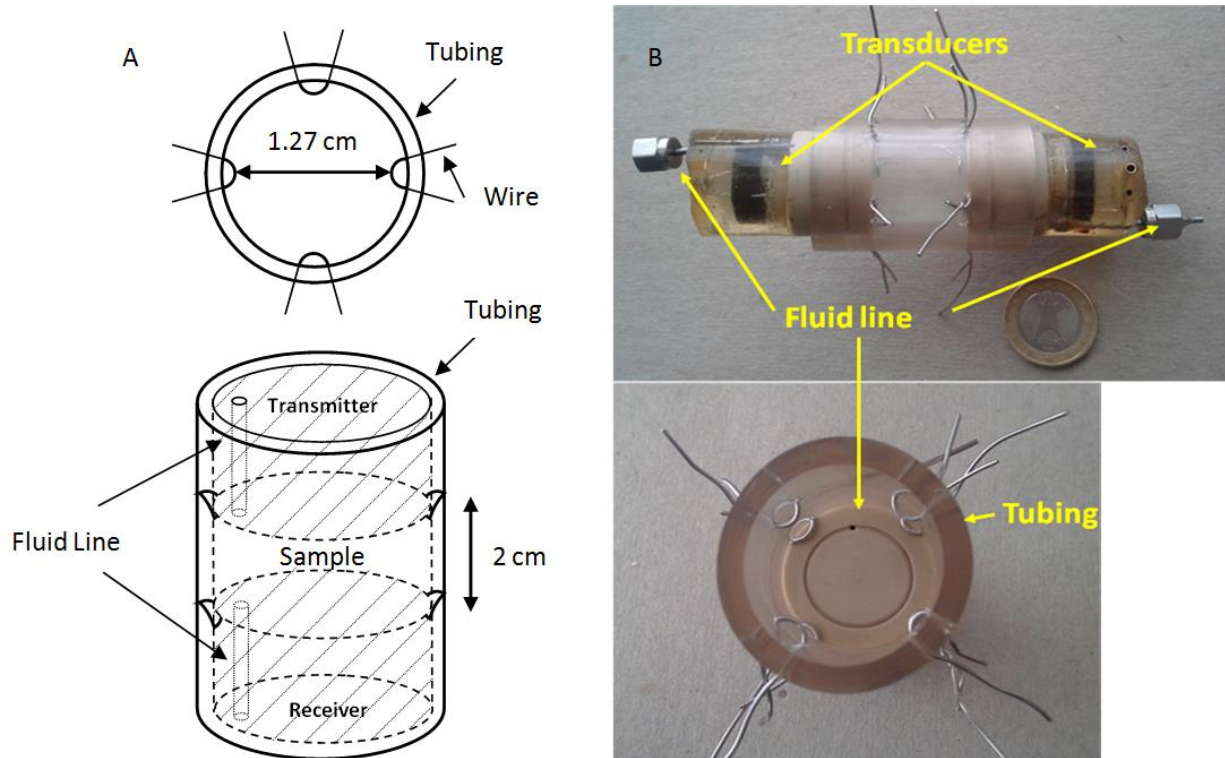


Figure 2-1 A) Schematic of sample B) Photograph showing the transducer and receiver holders. The wires extending from the sample are clipped before measurements and sealed with soft epoxy. Tubing is sealed against transducer and receiver using a metal wire.

Table 2-1 Impedance calculations

Material	Compressional Velocity (m/s)	Density (Kg/m³)	Impedance (Kg/m²s)	Source
Aluminum (~25 °C)	6391	2700	17.25 E6	This study
Liquid (~25 °C)	1550	979	1.52 E6	This study
Hydrate (1 °C)	3150	967	3.05 E6	This study
Frozen (-10 °C)	3560	967	3.44 E6	This study
PEEK (Temperature not specified)	2550	1290	3.29 E6	Hu et al., 2015

We used 81 wt% of de-aired and deionized water to yield 100% THF hydrate formation if the reactants are well mixed. After preparation, the THF-water mixture was de-aired and injected into the sample holder and sealed with the PEEK end caps and compliant epoxy. The fluid lines were closed and the sample was kept at a constant temperature by submerging it into a temperature-controlled water bath. Ultrasonic compressional waves were recorded in the THF-water mixture at atmospheric pressures in the liquid state (room temperature, ~25 °C) and at 100% stable hydrate formation (1 °C). To verify 100% hydrate conversion, an additional measurement was made at -10 °C. In this study we will call THF-water mixture as liquid, 100% THF hydrate as hydrate, and frozen THF hydrate as frozen.

The collected waveforms were analyzed for ultrasonic velocities and frequency content. The travel times were calculated from sample length and travel time of the first arrival of the signals, taking into account system delay time and temperature corrections. The first cycle of the waveforms was also analyzed for its frequency content using a Fast Fourier transform. Ultrasonic attenuation was calculated with the spectral ratio method (Toksöz et al., 1979). Briefly, the amplitude spectrum of the first cycle of a waveform propagating through the sample is divided by a similar wave propagating through a standard sample, aluminum in this study. Both the sample

and the standard had the same geometry. The slope of the frequency spectra ratio is related to the quality factor Q (inverse of attenuation, Q^{-1}) by:

$$Q = \frac{\pi * l}{\gamma * v} \quad (2-1)$$

Where the unitless Q is the quality factor, l the length of the samples [in m], γ the slope of the frequency ratios [in s], and v the measured velocity [in m/s].

NMR Measurements:

NMR measurements are sensitive to hydrogen atoms. We used a low-field (2 MHz) NMR device and a Laplace Transform to calculate T_2 relaxation times from the exponential magnetic signal decay. We used small glass vials (5.7 cm length and 1.5 cm diameter) with a THF-water mixture from the same batch that we used for the third set of acoustic measurements. These sealed glass vials were submerged into the cooling bath together with the sample holder for the ultrasonic measurements. NMR and acoustic measurements were made at the same temperature stages. All measurements were performed at atmospheric pressures. Instead of making NMR measurements under controlled temperature conditions, we continuously measured the NMR response of our sample while the hydrate started to dissociate. Each NMR measurement took about 3.5 min.

2.4 Results

Ultrasonic Properties:

Figure 2-2 shows the waveforms obtained at discrete temperatures corresponding to the initial THF/water mixture (~25 °C), after hydrate formation (1 °C), and subsequent freezing (- 10 °C). Also shown is the waveform obtained for the aluminum standard. Note that p-waves in

the liquid sample have the highest amplitude but have longest travel time. Waveforms in hydrate samples arrive earlier but with lower peak-to-peak amplitude. Further sample cooling to $-10\text{ }^{\circ}\text{C}$ results in earlier wave arrival as well as an increase in the peak-to-peak amplitude. The measured p-wave velocities (VP) at each stage are shown in Table 2-2. VP increases by a factor of 2 for the hydrate specimen compared to liquid. We observed an additional velocity increase of about 400 m/s for the frozen sample compared to the hydrate sample.

Figure 2-3 shows the frequency spectra for the THF mixture at different temperatures along with the aluminum standard calculated from the first cycles of the arriving wave. The frequency spectra for repeat measurements are similar for all samples, showing that the measurements, especially for the hydrate-bearing case, are reproducible. Figure 2-3 shows that signals through the aluminum standard have much higher frequency content than through the samples. The peak frequencies of the signals through the liquid samples are highest of all three samples. With hydrate formation, the frequency content decreases by about half. After freezing, the frequency content of signals propagating through the frozen samples is comparable to that through the liquid sample (Figure 2-3 d).

We calculated attenuation using Equation 2-1. The calculated p-wave attenuation (Q^{-1}) using aluminum as the standard is shown in Figure 2-4. Attenuation values were calculated for the liquid samples ($Q^{-1} < 0.15$). After hydrate formation, Q^{-1} increases by a factor of 3. The attenuation reduces again to almost the same value as for the liquid samples after the sample is frozen at -10°C . Since attenuation in pure liquid THF is unknown, the relatively high attenuation in the liquid sample is unexplained. Nevertheless, there is a relative increase in attenuation after hydrate formation.

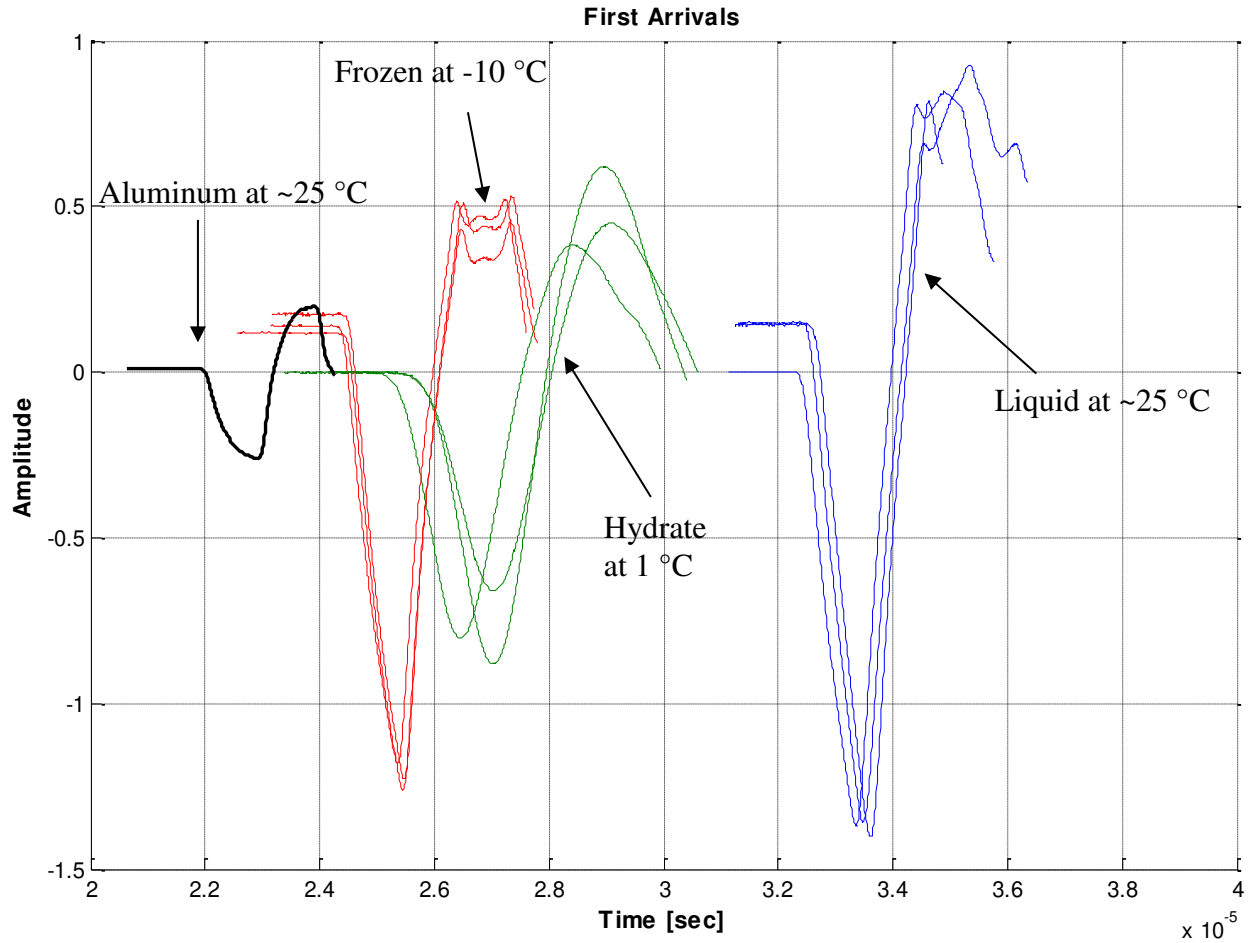


Figure 2-2 Raw waveforms of the first cycles of the P-waves in aluminum standard (black), frozen sample (red), only hydrate-bearing (green), and liquid (blue). The aluminum and liquid samples were measured at room temperature (~ 25 °C), Hydrate samples at 1 °C and frozen samples at -10 °C. All measurements were conducted at atmospheric pressure. Multiple lines at the same conditions mark repeat measurements. Note that the amplitude of the waveform through aluminum is the smallest of all the measured samples due to transducer design. These transducers are impedance matched to measure low impedance materials such as unconsolidated sands. Consequently, the high impedance contrast between the PEEK end caps and the aluminum causes parts of the signal to reflect off the aluminum instead of being transmitted through it.

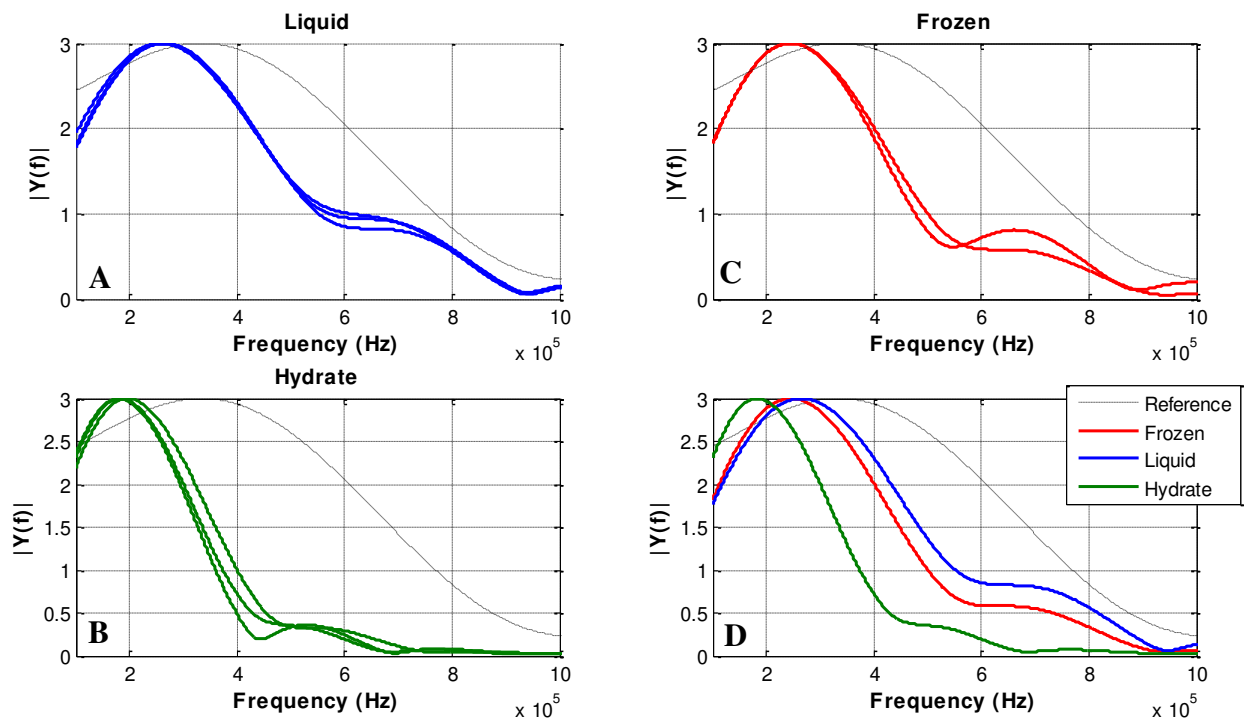


Figure 2-3 Frequency spectra of waveforms shown in Figure 2-2 for different samples to ensure repeatability. A) liquid sample B) hydrate sample C) frozen sample D) Comparison of Liquid, Hydrate, and Frozen frequencies. Time progression of the experiments were day 0 = Liquid data, day 3 = Hydrate data, and day 4 = Frozen data.

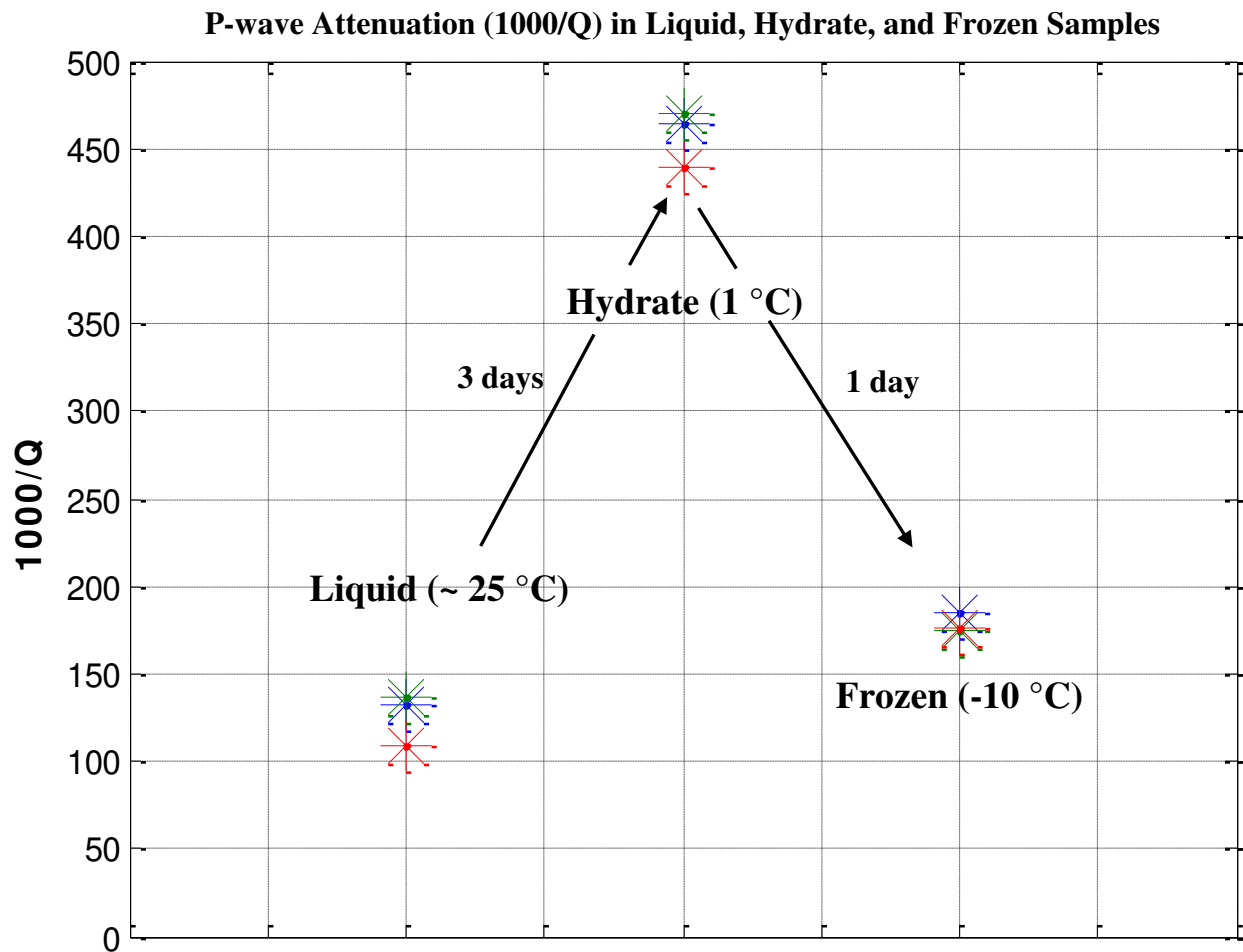


Figure 2-4 Overview of the calculated attenuation Q for the liquid, hydrate and frozen samples. Lines represent the time elapsed between measurements. Blue symbols correspond to the first set of measurements, green symbols to the second set of measurements, and the red symbols to the third set of measurements.

2.5 Discussion

We now examine the implication of the observed increase in velocity accompanied by an increase in attenuation after hydrate formation as well as a further increase in velocity accompanied by a decrease in attenuation after freezing.

The first observed velocity increase (almost by a factor of two) indicates THF hydrate formation. This increase in velocity is accompanied by an increase in attenuation. Johnston et al. (1979) described that attenuation could result from dissipation of energy due to viscous squirt flow of water within the intergranular spaces due to elastic deformation. In our experiments, this type of loss mechanism could mean that there is a fluid present between the THF hydrate grains. Squirt flow has been investigated and identified as a possible driving mechanism for attenuation in other hydrate related research (Guerin and Goldberg, 2005, Priest et al. 2006, Best et al. 2013).

After cooling the sample to below the freezing point of water, a second velocity increase was observed. The residual water in the sample converted into ice that led to an additional stiffening of the sample. Additionally, the attenuation decreased to a value similar to that observed in the liquid sample. The similarity between frequency spectra for liquid and frozen THF hydrate-ice sample suggests that there is little to no intrinsic attenuation within the THF hydrate phase itself. Future experiments should demonstrate specific losses due to the presence of water by comparison with a “dry” hydrate.

Experimental errors for the attenuation calculations were derived by using error propagation for each variable in equation 1 and are presented in Table 2-2. Errors of up to 25% were observed in the liquid samples but were as low as 4.5% for the frozen samples.

Table 2-2 Summary of calculated velocities, peak frequencies, and peak-to-peak amplitudes for all the samples.

Condition Property	Liquid ~ 25 °C	Hydrate 1 °C	Frozen -10 °C	Aluminum ~ 25 °C
Compressional Velocity (m/s)	1550 ± 11 (Avg. of 18 measurements)	3150 ± 95 (Avg. of 20 measurements)	3560 ± 63 (Avg. of 12 measurements)	6391 (Calculated from calibration experiment)
Average Peak Frequency [kHz]	276.3 ± 24.56	187.2 ± 8.67	245.9 ± 0.99	335.2
Average Peak to Peak Amplitude (V)	2.1463 ± 0.094	1.0050 ± 0.099	1.69 ± 0.0016	0.46
Average Slope of the Frequency Ratios γ	5.36 E6 ± 0.618 E-6	9.35 E6 ± 0.342 E-6	3.335 E6 ± 0.134 E-6	
Attenuation (Q⁻¹)	0.124 ± 0.032	0.458 ± 0.022	0.179 ± 0.008	

The transducers used had PEEK end caps and the impedance match is lower between PEEK and the liquid sample causing higher uncertainties in the attenuation calculation whereas the impedance contrast between PEEK-hydrate and PEEK-frozen samples is matched better (Table 2-1), resulting in better quality data.

Residual Fluid Identification

The observation and measurements presented above suggest the presence of free water after complete hydrate formation which might explain a higher attenuation in the sample. To confirm the presence of water content independently, we performed nuclear magnetic resonance (NMR) measurements. The presence of fluids in the supposedly “100%” hydrate sample can be due to possible reasons: First, even though THF has a stoichiometric relationship with water, it is difficult to achieve 100% THF hydrate formation due to the volatility of THF. Possibly, some of the THF evaporates during the mixing process of THF with water, leaving the remaining mixture with excess water after hydrate formation. Since THF hydrate forms above the freezing point of water, the residual water present is in liquid form. Second, the mixture contained excess THF. An inaccurate THF water ratio could have been used resulting in a sample with residual THF after forming hydrates. Third, insufficient time was allowed for full hydrate formation. Fourth, while forming THF-hydrates, some of the THF was separated from the water leading to pockets of water and THF.

Figure 2-5a shows the raw data for NMR T2 relaxation for a sample that was measured starting at around 1 °C, meaning that it is well below the hydrate stability temperature (~ 4°C) but above the freezing point of water. If the conversion from THF and water into THF hydrates had been complete, the T2 signal would decay faster than our instruments capability, and no signal

should be observable. Figure 2-5a shows a T2 signal with a small but not negligible amplitude that relaxes quickly, indicating the presence of free hydrogen, either in the form of water or THF. In this case, fast (or quick) refers to the time it takes for the signal to decay. For example, the first measurement relaxes within 1000 ms compared to the 13th measurement which relaxes after 5000 ms. A fast relaxation time is typical for capillary bound and/or surface bound water (Kleinberg, 1996, Saidian et al., 2015). In analogy, the fast relaxation time in our measurements indicates that the liquid is probably trapped between the hydrate crystals. The inversion of this measurement (Figure 2-5b) does not show a distinct peak, and therefore it is impossible to quantify the type of liquid. The measurements in the NMR were not temperature controlled which caused the hydrate to dissociate. In Figure 2-5a we can observe how the signal changes for the same sample after the hydrates start to dissociate. 62 minutes elapsed between the first and the last measurement. After 42 minutes (13th – 18th measurement) the T2 relaxation time does not change much, indicating the complete dissociation of the hydrates. The ultrasonic signals (Figure 2-5c) show the corresponding first arrivals for the first and 13th measurement of the NMR. It can be observed that the velocity dropped whereas the inversion, as well as the raw data amplitude of the NMR, increased.

NMR measurements were also performed on the frozen sample (~ -10 °C) and shown in Figure 2-6. The results presented in Figure 2-5 and Figure 2-6 clearly show that a mobile fluid phase is present when the sample temperature is around 1 °C, which is not visible when the sample is frozen. Given that the freezing point for THF is -100 °C (Jones et al., 2010), we determine that the residual fluid is water and the elevated attenuation in the hydrate phase is due to residual water left in pockets between hydrate crystals. Tittman et al. (1974) observed similar high attenuation values in moon rocks exposed to volatiles.

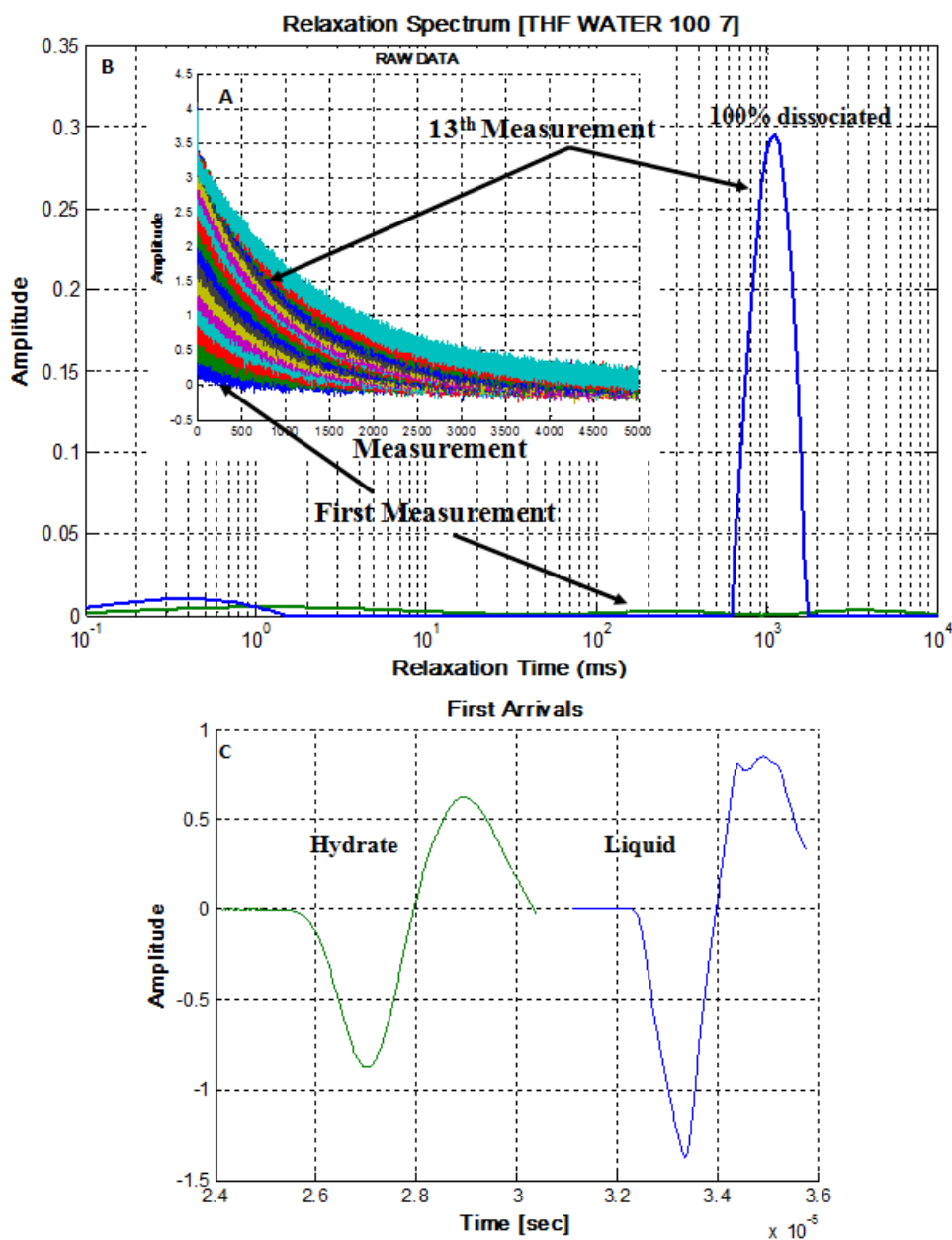


Figure 2-5 A) Raw data for a sample containing “100%” THF hydrate. Continuous measurements show an increase in amplitude and longer relaxation times which are a result of the dissociation of the hydrate and therefore the availability of more free hydrogen. B) Inversion of a sample containing “100%” THF hydrate. Comparison of the First Run at 1 °C with a measurement performed after hydrates were completely dissolved. Inverted signals below an amplitude of 0.01 should not be considered since they may result from inversion artifacts. C) First arrivals for the sample containing only hydrates (green) which corresponds to the first measurement of the NMR and the first arrival of the sample in the liquid stage (blue) which corresponds to the 13th measurement of the NMR.

The attenuation values dropped after removing the volatiles using a vacuum. Our experimental data provide the confirmation for fluid-filled pores within the hydrates as the leading cause for elevated attenuation (Best et al., 2013). These data can now be used to constrain and improve models to estimate subsurface gas hydrate quantities from seismic property changes in hydrate-bearing sediments.

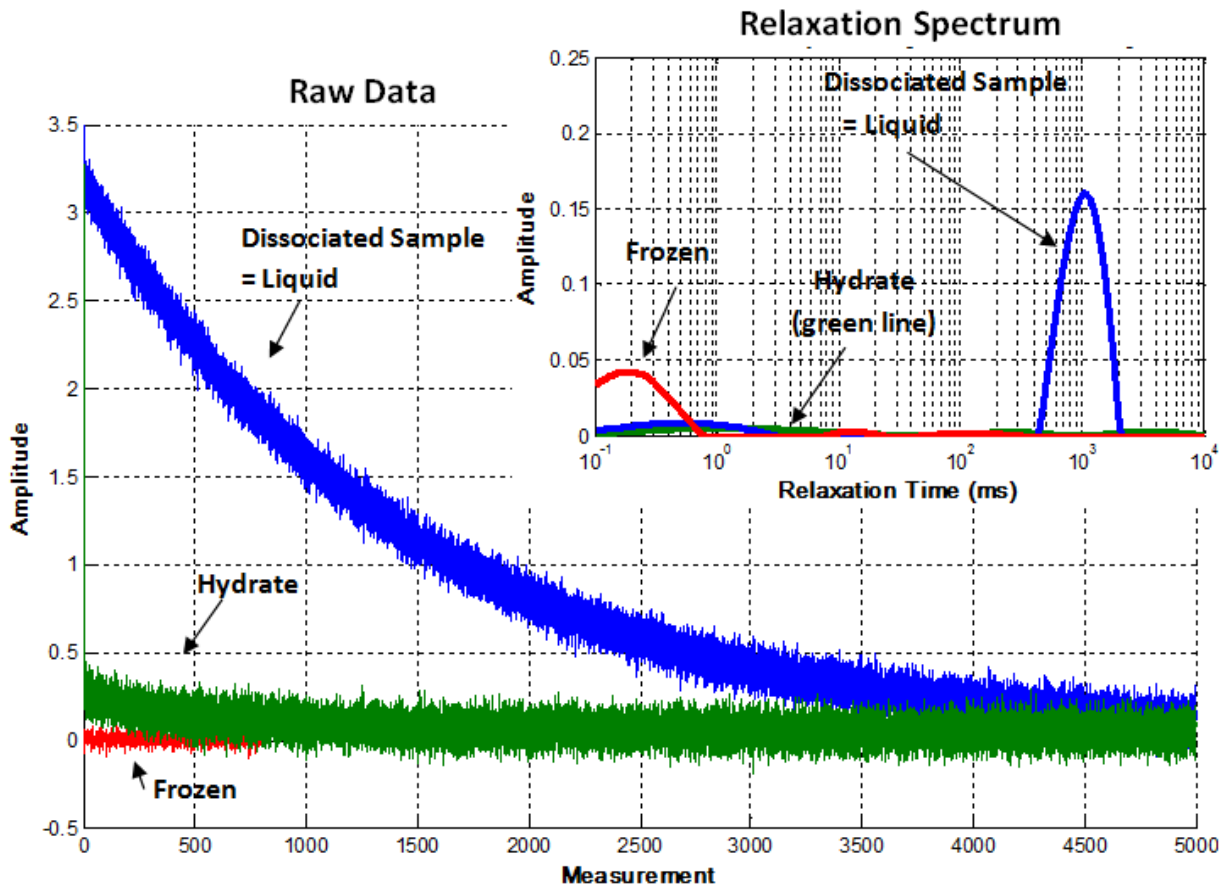


Figure 2-6 Red line shows the relaxation time for a sample containing “100%” THF Hydrate at -10 °C (frozen), green line shows the relaxation time for a sample containing “100%” THF hydrate at 1 °C (hydrate), and blue line shows the relaxation time for a sample containing THF-water mixture (liquid). Note: a subtle difference in relaxation time of Frozen and Hydrate sample.

2.6 Conclusions

We have shown that THF-water mixture, THF hydrate with residual water, and THF hydrate with frozen residual water are distinguishable by their ultrasonic velocity and attenuation as well as NMR signatures. We conclude that pure, solid THF hydrate phase has negligible attenuation, while elevated attenuation is found in the presence of liquid water. A combination of NMR and ultrasonic measurements allows us to characterize gas hydrate formation as well as dissociation processes.

2.7 Acknowledgement

This material is based upon work supported by the U.S. Department of Energy, Office of Science, Office of Fossil Energy, under Award Number DE-FE 0009963. We gratefully acknowledge Kurt Peter Livo and Milad Saidian for providing help in conducting the NMR measurements as well as interpreting the NMR data. The authors would also like to thank William Waite who provided constructive comments.

2.8 References

- Best, A.I., Priest, J. a., Clayton, C.R.I., Rees, E.V.L., (2013), The effect of methane hydrate morphology and water saturation on seismic wave attenuation in sand under shallow sub-seafloor conditions, *Earth and Planetary Science Letters* 368, 78–87.
- Dvorkin, J, R. Uden (2004), “Seismic wave attenuation in a methane hydrate reservoir” *The Leading Edge Interpreter’s Corner*
- Guerin, G., and D. Goldberg, 2005, Modeling of acoustic wave dissipation in gas-hydrate bearing sediments, *Geochemistry, Geophysics, Geosystems*, v. 6, Q07010, doi:10.1029/2005GC000918.
- Guerin, G., and Goldberg, D., (2002). Sonic waveform attenuation in gas hydrate-bearing sediments from the Mallik 2L-38 research well, MacKenzie Delta, Canada. *J. Geophys. Res.*, 107:2088. doi:10.1029/2001JB000556

- Helgerud M.B, W.F. Waite, S.H. Kirby, A. Nur, (2009), Elastic wave speeds and moduli in polycrystalline ice Ih, sI methane hydrate, and sII methane-ethane hydrate, *Journal of Geophysical Research*, 114, p. B02212
- Johnston, D. H., Toksöz, M. N., & Timur, A. (1979). Attenuation of seismic waves in dry and saturated rocks: II. Mechanisms. *Geophysics*, 44(4), 691-711.
- Jones, C. Y., J.S. Zhang, and J.W. Lee (2010), Isotope Effect on Eutectic and Hydrate Melting Temperatures in the Water-THF System, *Journal of Thermodynamics*, Volume 2010 (2010), Article ID 583041
- Kleinberg, R.L., (1996), Utility of NMR T2 distributions, connection with capillary pressure, clay effect, and determination of the surface relaxivity parameter (RHO) 2: 3rd Louvain Catholic University et. al., Recent Advances in MR application to porous media international meeting, Proceedings: Magnetic Resonance Imaging, v. 14/7-8, p. 761-767.
- Hamilton, E. L., (1972), Compressional-wave attenuation in marine sediments: *Geophysics*, 37, 620-646.
- Hu, Y., Wenliang, M., & Zhaoba, W. (2015). A study of Ultrasonic guided wave NDT Technique based on PEEK rod. *International Journal of Hybrid Information Technology*, 8(8), 215-224.
- Klimentos, T. and McCann, C., (1990), Relationships between compressional wave attenuation, porosity, clay content, and permeability of sandstone: *Geophysics*, v. 55, p. 998-1014.
- Koesoemadinat A.P. and McMechan G.A., (2001). Empirical estimation of viscoelastic seismic parameters from petrophysical properties of sandstone, *Geophysics*, 66, 1340–1649.
- Lee, M. W., & Collett, T. S. (2001). Elastic properties of gas hydrate-bearing sediments. *Geophysics*, 66(3), 763-771
- Liu, Z., Rector, J. W., Nihei, K. T., Tomutsa, L., Myer, L. R., & Nakagawa, S. (2001). Extensional wave attenuation and velocity in partially-saturated sand in the sonic frequency range. In *SEG Technical Program Expanded Abstracts 2001* (pp. 1808-1811). Society of Exploration Geophysicists.
- Makino, T., Sugahara, T., and Ohgaki, K. (2005). Stability boundaries of tetrahydrofuran plus water system, *Journal of Chemical and Engineering Data*, 50(6), 2058-2060.
- Molotova and Vassil'ev (1960), *Bull. (Izvest.) Acad. Sei. USSR, Geoph. Ser. (Eng. Ed.)* 8, 731
- Prasad, M. and R. Meissner, (1992), Attenuation mechanisms in sands: Laboratory versus theoretical Biot data, *Geophysics* 57, 710–719
- Prasad, M. and J. Dvorkin (2004), Velocity and attenuation of compressional waves in brines, *SEG Expanded Abstr.*, 23, 1666, doi: 10.1190/1.1845150.

- Pratt, R., K. Bauer, and M. Weber (2003), Crosshole waveform tomography velocity and attenuation images of arctic gas hydrates, paper presented at 73rd Annual Meeting, Soc. Of Explor. Geophys., Dallas, Tex.
- Priest, J. A., Best, A. I., & Clayton, C. R. (2006). Attenuation of seismic waves in methane gas hydrate-bearing sand. *Geophysical Journal International*, 164(1), 149-159.
- Saidian, M. and Prasad, M., (2015), Effect of Mineralogy on Nuclear Magnetic Resonance Surface Relaxivity: A Case Study of Middle Bakken and Three Forks Formations, *Fuel*, Volume 161, Pages 197- 206.
- Sloan, E. D. & Koh, C. A. (2007), *Clathrate Hydrates of Natural Gases*. 3rd ed., CRC Press, Taylor & Francis Group, Boca Raton, FL
- Suzuki, H., and J. Matsuhima, (2013), Quantifying uncertainties in attenuation estimation at methane-hydrate-bearing zones using sonic waveform logs: *Geophysics*, 78, no. 5, D339–D353, doi: 10.1190/geo2012-0495.1
- Toksöz, M.N., Johnston, D.H., and Timur, A., (1979), Attenuation of seismic waves in dry and saturated rocks: 1. Laboratory measurement; *Geophysics*, 44, 681-690.
- Tittmann, B. R., Housley, R. M., Alers, G. A., & Cirlin, E. H. (1974). Internal friction in rocks and its relationship to volatiles on the moon. In *Lunar and Planetary Science Conference Proceedings* (Vol. 5, pp. 2913-2918).
- Waite, W.F., M.B. Helgerud, A. Nur, J.C. Pinkston, L.A. Stern, S.H. Kirby, W.B. Durham, (2000), Laboratory measurements of compressional and shear wave speeds through methane hydrate, *Annals of the New York Academy of Sciences*
- Wang, Y.-H. and J.C. Santamarina, (2007), Attenuation in sand: an exploratory study on the small-strain behavior and the influence of moisture condensation, *Granular Matter*, Volume 9, Issue 6, pp 365-376
- Wood, W.T., Holbrook, W.S. & Hoskins, H., (2000), “In situ measurements of P-wave attenuation in methane hydrate and gas bearing sediments on the Blake Ridge” *Proc. ODP. Results*, Vol 164, pp. 265-272, eds Paull, C., Matsumoto, R., Wallace, P. & others, Ocean Drilling Program, College Station, Texas
- Yun, T. S., Francisca, F. M., Santamarina, J. C., Ruppel, C (2005). “Compressional and Shear Wave Velocities in Uncemented Sediment Containing Gas Hydrate.” *Geophysical Research Letters*, Vol. 32, L10609, doi:10.1029/2005GL022607

CHAPTER 3

INVESTIGATING THE INFLUENCE OF CLAY CONTENT ON ULTRASONIC VELOCITIES AND ATTENUATION OF THF HYDRATE-BEARING SEDIMENT

To be submitted to: *Journal of Geophysical Research* .

Mathias Pohl^{*a}, Manika Prasad^a, Michael L. Batzle^{a†}

3.1 Abstract

Hydrates in nature can occur in sedimentary formations with varying clay content that are composed of different minerals. The practice of using seismic velocities to estimate the amount of gas hydrates in the subsurface can be improved with a better understanding of the effect of hydrate formation on the elastic properties of clay-bearing sediments. To achieve this goal, we measured ultrasonic velocities and attenuations (or the inverse, quality factor Q) in tetrahydrofuran (THF) hydrate-bearing Ottawa sand with varying hydrate saturation and kaolinite content. We find that at hydrate saturations below 60%, ultrasonic velocities are sensitive to both clay content and pressure. A complete consolidation, independent of pressure, is inferred at 80% THF hydrate saturation from the V_p - V_s ratios and quality factors. Clay content does not affect this behavior. A loss of amplitude and frequency of the first time arrival cycle is observed in the P-waveform of samples with high clay content (30 wt%) and low THF hydrate saturation (40%) after elevated pressures. S-waveforms have a higher quality recovery at this stage. The same effect cannot be space. Our results show that hydrates in unconsolidated sand –clay mixtures have a significant

*Primary author and editor.

Corresponding author. Direct correspondence to mpohl@mines.edu.

^aDepartment of Geophysics, Colorado School of Mines, Golden, CO 80401, USA

influence on ultrasonic velocities and attenuation and should be considered when interpreting seismic and well log data.

3.2 Introduction

Gas hydrates are crystalline inclusion compounds which entrap guest molecules (e.g., methane (CH_4)) in a hydrogen-bonded framework (Sloan and Koh, 2007). They occur in permafrost and in marine sediments and are considered potential energy resource. There is a need to estimate the amount of gas hydrates in the subsurface to reliably evaluate gas resources contained in gas hydrates or geohazards and climate change effects posed by gas hydrate dissociation (Kvenvolden, 1999; Collett, 2002; Ruppel, 2007; Priest et al., 2009, Maslin et al., 2010; Boswell and Collett, 2011). Gas hydrate deposits are commonly identified through seismic surveys and well logs, which require calibration through laboratory velocity measurements.

Previous laboratory studies were mostly performed on clean quartz sands (e.g., Waite et al., 2004; Spangenberg et al., 2005; Yun et al., 2005, Priest et al., 2009) or on kaolinite with varying amounts of THF hydrates (Lee et al., 2010). Since natural hydrate-bearing sediments are almost always mixtures of quartz and clay (e.g., Lorenson et al., 2000), seismic measurements on sand-clay mixtures are needed to investigate the interaction between hydrates and sand-clay sediments.

Natural gas hydrates often form from methane dissolved in water – this process of forming methane hydrates is challenging and time-consuming. We used tetrahydrofuran ($\text{C}_4\text{H}_8\text{O}$ or THF) as a hydrate former. THF is completely miscible in water and forms hydrates out of solution, yielding a homogeneous synthesis of THF hydrate in the sediment (Lee et al., 2007). THF hydrates form at ambient pressures and are stable up to 4 °C. Although THF forms structure II hydrates, these hydrates can still be considered a proxy for structure I methane hydrates because: A) the

elastic properties of structure I and structure II hydrate do not vary significantly (Helgerud et al., 2009). The data spread due to differences in the sandpacks is larger than differences between structures I and II (Waite et al., 2011), B) ultrasonic velocities in THF hydrate-bearing sediments are similar to CH₄ hydrate-bearing sediments formed out of solution (Rydzy, 2013), and C) CT-imaging has shown that methane hydrate (Kerkar et al., 2014) and THF hydrate (Schindler et al., 2017) form in the pore space of sediments, and so they are expected to have little effect on velocity.

Natural gas hydrate deposits have been identified by elevated velocities and heightened attenuation properties (Guerin & Goldberg, 2002). An increase in the amount of hydrates in the pore space is accompanied by a reduction in porosity and increases elastic moduli of the solid frame (Dvorkin and Uden, 2004). Although velocity increase in stiffer rocks is generally accompanied by a decrease in attenuation (Klimentos & McCann, 1990, Prasad and Meissner, 1992, Koesoemadinata and McMechan, 2001), a velocity increase with increasing hydrate saturation is accompanied by an increase in attenuation (Wood, 2000; Guerin and Goldberg, 2002; Pratt et al., 2005; Suzuki and Matsuhima, 2013).

Recent experimental studies have shown, that the presence of water films between hydrate and sediments (Kerkar et al., 2014; Chaouachi et al., 2015; Sahoo et al., 2018; Sell et al., 2018) as well as free water between hydrate crystals (Chand and Minshull, 2004, Pohl et al., 2017) can explain the elevated attenuation observed in gas hydrate bearing systems. However, in natural gas hydrate systems, only a few studies have seen elevated attenuation values in the presence of hydrates (Wood et al., 2000, Guerin and Goldberg, 2002, Pratt et al., 2005; Suzuki and Matsuhima, 2013). Using seismic attenuation studies in the KG Basin, Dewangan et al. (2014) and Jyothi et al. (2017) have shown that clay-rich sediments show reduced attenuation values when they are hydrate-bearing. Note that this finding contrasts with Guering & Goldberg (2002) who identified

natural gas hydrate deposits by elevated velocities and heightened attenuation properties. Our study is aimed at addressing the lack of velocity and attenuation studies in clay-rich hydrate-bearing sediments.

We measured ultrasonic velocities and attenuations in THF hydrate-bearing sediment samples composed of Ottawa sand with varying fractions of kaolinite. To our knowledge, this is the first study of velocity and attenuation in hydrate-bearing sand-clay sediments. Our ultrasonic velocity results link the end-member studies on clean sand (Waite et al., 2004; Spangenberg et al., 2005; Yun et al., 2005, Priest et al., 2009) and on clean clay (Lee et al., 2010). Previous measurements from other laboratories (Table 3-1) have shown the effects of hydrate formation in various clean sediments. Our results should help to better understand the effects of gas hydrates on seismic properties of unconsolidated sand-clay sediments and to quantify hydrate occurrences in nature.

Table 3-1 Overview of ultrasonic velocity measurements on various sediments from the literature.

Source	Host	Formation	Porosity	S_{GH}	V_{ph} [km/s]
Pearson et al. (1986)	Berea Sandstone	THF Hydrate	~0.40	1.00	4.7
Collett (2000)	Synthetic Rock	THF Hydrate	~0.26	0.60-1.00	3.26-3.69
Kunerth et al. (2001)	Garnet Sand	THF Hydrate	Unknown	1.00	3.6
Yun et al. (2005)	Ottawa Sand	THF Hydrate	0.39	0.58-1.00	2.00-3.80
Wang et al. (2008)	Unspecified Sand	THF Hydrate	Unknown	1.00?	3.74
Lee et al. (2010)	Various	THF Hydrate	Various	0.00, 0.50, 1.00	1.48-4.20
Rydzy et al. (2013)	Ottawa Sand	THF Hydrate	0.40	0.80	3.1

3.3 Samples Used & Procedure

Sample Preparation

We used Ottawa sand F110 (clean quartz sand with 60-280 μm grain size; Figure 3- a) and aggregates of kaolinite (from Wards Natural Science Establishment), a non-swelling clay (Mohan et al., 1993) chosen to avoid swelling-related effects such as plugging pore fluid line. The size of the clay aggregates was similar to or smaller than the sand grain sizes (Figure 3- b). We thoroughly mixed the Ottawa sand with varying amounts (0, 10, or 30 wt%) of clay until the mixture appeared to be homogenous. The mixing allowed the clay to be dispersed and structurally load bearing. 16.1 g of the sand-clay mixture was placed into an instrumented sample holder and compacted to a cylinder of 2.54 cm diameter and 2.00 cm length. The exact sample length was measured using X-ray CT scans. Porosity was calculated from the weight and volumetric dimensions of each specimen prior to hydrate formation. The THF-water mixture and THF saturations achieved are given in Table 3-2.

Table 3-2 Water – THF mixtures used to achieve 40, 60, and 80% hydrate saturation in the sediments

Water (wt%)	THF (wt%)	Hydrate Saturation (%)
92.36	7.64	40
88.54	11.46	60
84.72	15.28	80

Experimental Setup

The experimental setup, described in detail in Rydzy et al. (2013) and Pohl et al. (2017) is shown in Figure 3-. Briefly, the setup consist of a temperature-controlled pressure vessel filled with hydraulic oil to allow the application of a hydrostatic confining pressure. Two end caps made

of polyether ether ketone (PEEK) serve to hold the 500 kHz piezoelectric transducers as well as fluid lines for fluid injection and pore pressure control. The sample is placed between the end caps with a thermocouple attached to the upper and the lower end of the sample to record temperatures. The transducers are excited by a pulse of 300 V and the propagating signals are recorded and stored using a digital oscilloscope.

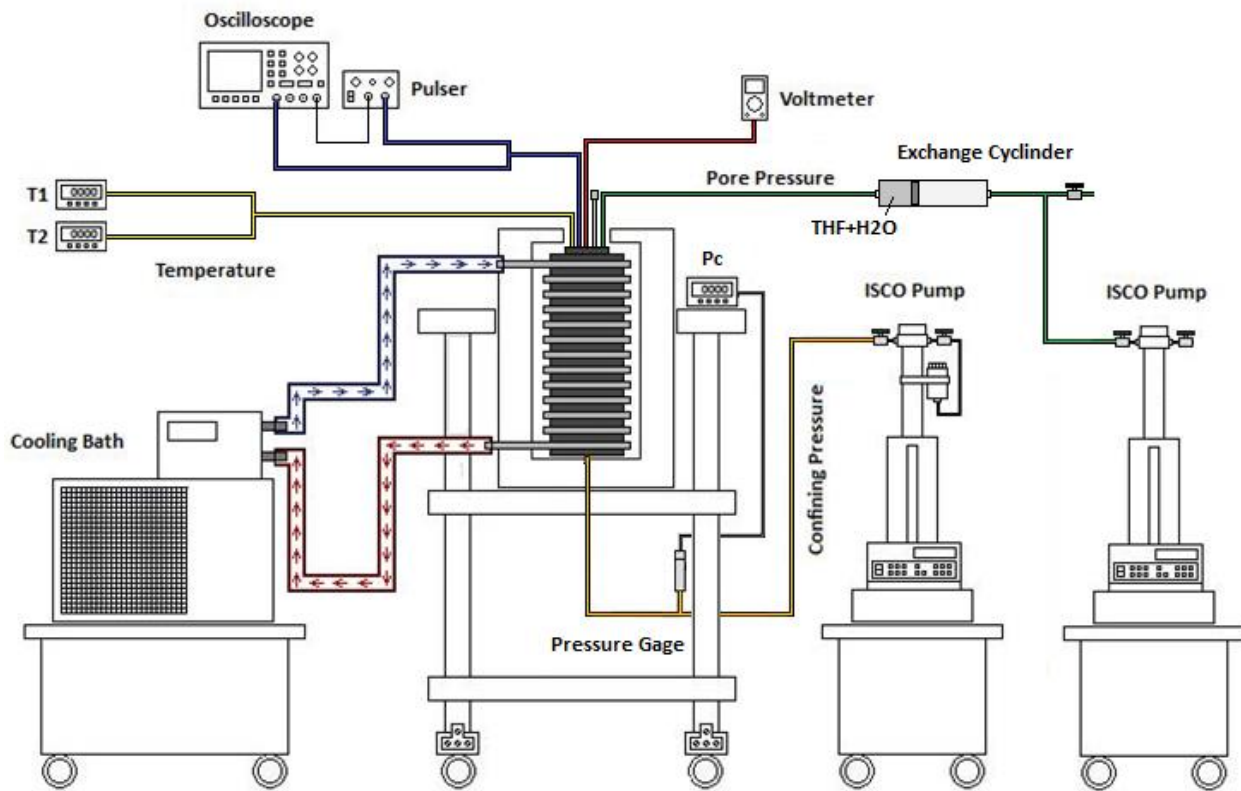


Figure 3-1 Experimental setup for ultrasonic velocity measurements in hydrate-bearing sediments under reservoir conditions (after Ryzdy et al., 2013).

Experimental Procedure

The sample was placed between the end caps surrounded by Tygon® tubing and placed in the pressure vessel. Confining pressure (P_c) was increased to 535 psi at a rate of 9 psi/min. The sample was then vacuumed and injected with a THF-water solution maintained at a pore pressure (P_p) of 100 psi, resulting in a differential pressure (P_d) of 435 psi (~3 MPa). Ultrasonic P- and S-waves, as well as temperature, were recorded at six different experimental stages which are described in the following (see summary in Table 3-3):

Stage I – Baseline measurements without hydrates made at room temperature (~ 24°C), $P_d = 435$ psi, $P_c = 535$ psi, and $P_p = 100$ psi. At this stage, no hydrates are present and the samples are completely THF-water saturated.

Stage II-A – sediment – hydrate measurements at $P_d = 435$ psi made after the temperature was lowered to 0.5°C at a rate of 6.5 °C/h to induce hydrate formation. Pressures were kept constant ($P_c=535$ psi and $P_p=100$).

Stage II-B – sediment - hydrate measurements at $P_d = 2175$ psi. After hydrates were formed in the sediment, the confining pressure was increased to 2275 psi resulting in a differential pressure of 2175 psi. This stage was performed to observe the effects of confining pressure increase on the hydrate bearing sediments.

Stage II-C – sediment - hydrate measurements at $P_d = 435$ psi. Confining pressure was reduced back to the same value as in Stage II-A to observe hysteresis effects due to elevated pressures on hydrate bearing sediments.

Stage III-A – final measurements without hydrates at $P_d = 435$ psi at room temperature (~ 24°C). During this stage the cooling bath was turned off which resulted in a temperature

increase back to room temperature conditions (24 °C) causing the hydrates within the samples to dissociate.

Stage III-B – final measurements without hydrates at $P_d = 2175$ psi at room temperature (24°C). The confining pressure was increased to 2275 psi to compare velocities in hydrate-bearing and hydrate free samples at elevated pressures. Note: This last step was not performed on samples that contain 80% hydrate saturation.

Multiple samples for each combination of THF-water and sand-clay mixtures were measured to establish the degree of repeatability of the experimental data (Table 3-4).

Table 3-3 Overview of the temperature and pressure conditions for different stages during the experiments

Stage	Confining Pressure (psi)	Pore Pressure (psi)	Differential Pressure (psi)	Temperature (°C)	Hydrate-bearing (Yes/No)
I	535	100	435	24	No
II-A	535	100	435	0.5	Yes
II-B	2275	100	2175	0.5	Yes
II-C	535	100	435	0.5	Yes
III-A	535	100	435	24	No
III-B	2275	100	2175	24	No

Table 3-4 Overview of the number of measurements made on samples for the various cases discussed here.

	80% Hydrate Saturation	60% Hydrate Saturation	40% Hydrate Saturation
Pure Quartz Sand Samples	6	3	3
90 wt% Quartz + 10 wt% Clay	4	2	2
70 wt% Quartz + 30 wt% Clay	5	2	2

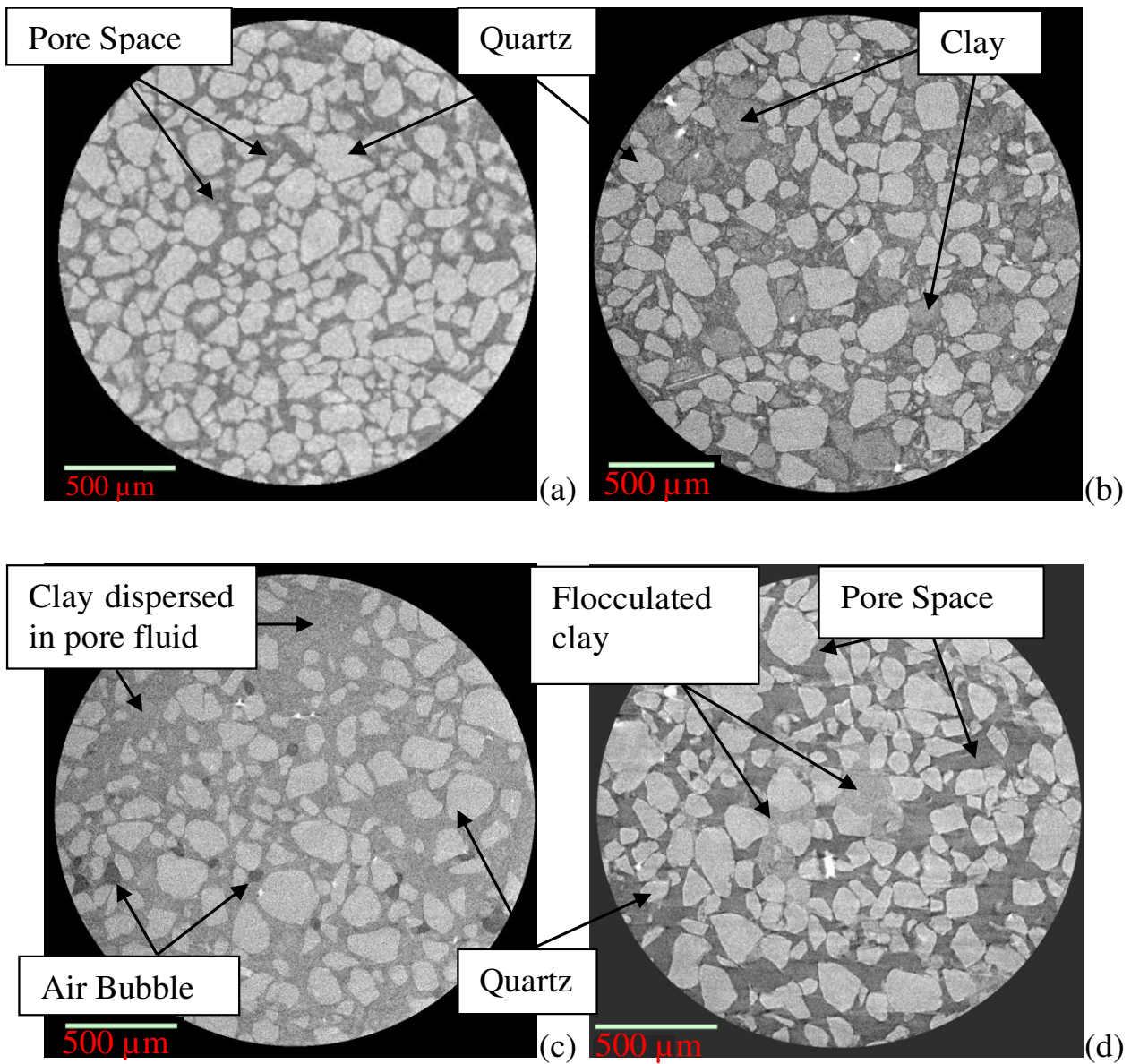


Figure 3-2 Micro X-Ray CT images of (a) dry Ottawa sand, (b) dry Ottawa sand mixed with 30 wt% clay, (c) fluid saturated Ottawa sand with 30 wt% clay, and (d) dried Ottawa sand mixed with 30 wt% clay

Ultrasonic Velocities

Ultrasonic velocities were calculated using the sample length and the first arrival time estimated from each waveform. The final measured velocity was corrected for temperature and the time required for the signal to pass through the PEEK end caps (dead time correction). P- and S-wave velocities were determined with an error of about 3.5%. The main source for this error was the uncertainty in picking the correct arrival time. Data points, shown in this work, are the averaged values from repeated measurements with the same sample composition and hydrate saturation. Arrow bars represent the standard deviation of the repeated measurements.

Ultrasonic Attenuation

The first cycle of the ultrasonic waveform was analyzed for its frequency content using a Fast Fourier Transform (FFT). We used the spectral ratio method to calculate ultrasonic attenuation (Toksöz et al., 1979). The frequency spectrum of the first cycle of a waveform propagating through a standard sample is divided by the spectrum of the first cycle of a wave propagating through the saturated sediment sample. Figure 3-1 shows the analysis for a typical shear wave signal. Attenuation is calculated from the slope of the spectral ratio. We used a constant frequency window of 400 kHz in all our calculations, although the variation in attenuation did not vary by more than 4% for larger frequency windows. The assumption made was that the attenuation is a linear function of frequency in this window.

Aluminum was used as a standard material in this study because its attenuation is considered negligible. The sample and the standard were both measured with the same transducers and had the same geometry. The slope of the frequency spectrum ratio (Figure 3-1 d) is related to the quality factor Q (inverse of attenuation, Q^{-1}) by:

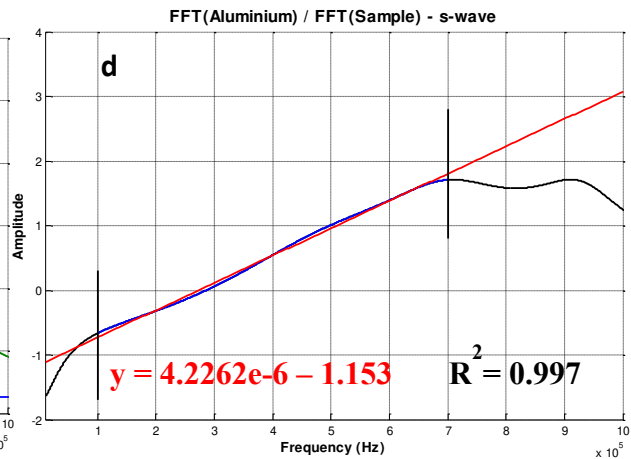
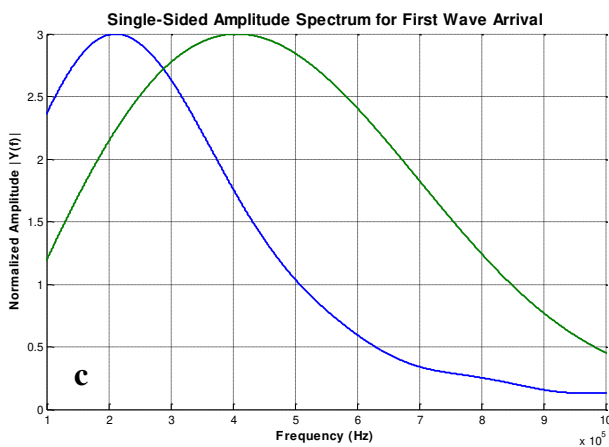
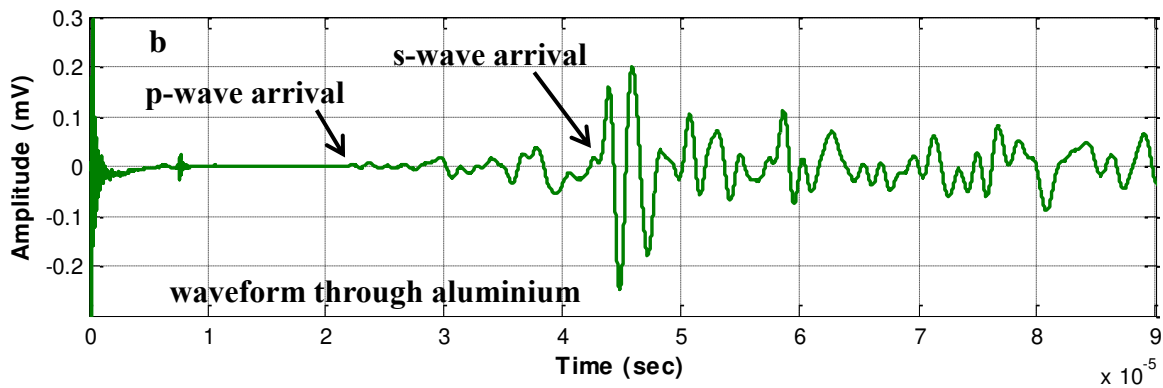
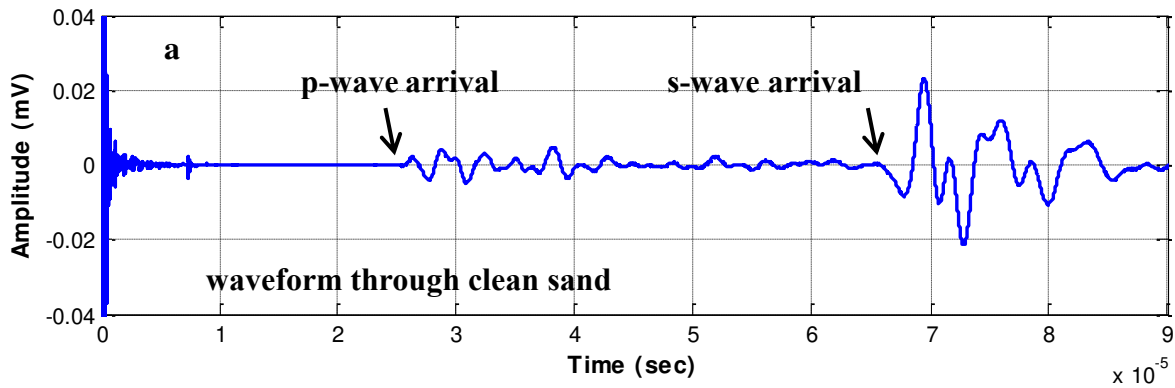


Figure 3-1 a) Example of a collected S-waveform through a clean quartz sand sample saturated with liquid THF-water b) Example of a collected S-waveform through aluminium standard c) Normalized frequency content of the same S-wave (a) in blue and aluminium standard (b) in green, d) ratio between frequency content of aluminium and sample, the slope between the two black bars is γ .

$$Q = \frac{\pi * l}{\gamma * v} \quad (3-1)$$

Where the unitless Q is the quality factor, l is the length of the samples [in m], γ is the slope of the frequency ratios [in s], and v is the measured velocity [in m/s]. For compressional velocities (V_p) and shear wave velocities (V_s) the quality factors will be expressed as Q_p and Q_s , respectively.

3.4 Results

In the following section, we investigate the influence of hydrate formation on the ultrasonic velocities and attenuation in clean sands as well as sand-clay mixtures. A summary of the data are given in Appendix A.

3.4.1 Ultrasonic Velocity Measurements

Clean Sand

Figure 3-2 shows V_p and V_s values for the clean sand packs with varying hydrate saturations along with measurements without hydrates. V_p and V_s in Stage I do not vary significantly ($V_p = 2121 \text{ m/s} \pm 22 \text{ m/s}$; $V_s = 605 \text{ m/s} \pm 15 \text{ m/s}$). With the formation of hydrates in Stage II-A, V_p and V_s increase proportional to the resulting hydrate saturation. The highest increase in velocity occurs when the samples are 80% hydrate saturated. At this stage, V_s in the 80% hydrate saturated samples increases threefold from ~ 605 to $\sim 1700 \text{ m/s}$, while V_p increases by 50% from 2121 to 3220 m/s. At all hydrate saturation, velocities increase with pressure (Stage II-B) and show some hysteresis with velocities in Stage II-C not returning to the same level as in Stage II-A. After hydrate dissociation, where the samples were brought back to room

temperature (Stage III-A), the ultrasonic velocities returned to the same or slightly higher values as in Stage I; $V_p = 2189 \text{ m/s} \pm 40 \text{ m/s}$ and $V_s = 641 \text{ m/s} \pm 20 \text{ m/s}$. The decrease in velocities from Stage II-C to Stage III-A are proportional to THF hydrate saturation and mimic the changes from Stage I to Stage II-A; the greater the saturation the greater the decrease in velocity. Finally, the pressure sensitivity test for all sands (Stage III-B) shows uniform increase with pressure; V_p increased by 208 m/s to $2397 \pm 30 \text{ m/s}$ and V_s increased by 262 m/s to $903 \text{ m/s} \pm 9 \text{ m/s}$.

V_p - V_s ratios for the clean sand samples with varying hydrate saturation and under different confining pressures are presented in Figure 3-3. The V_p - V_s ratio for the THF-water saturated clean sand samples is around 3.5. After hydrate formation (Stage II-A), the V_p - V_s ratios for the sands containing 80% THF hydrate saturation fall below 2 and remain there as long as hydrates are present in the sample (up to Stage II-C). Below 80% hydrate saturation, the V_p - V_s ratio of sands decreases from 3.5 to about 3 after hydrates are formed (Stage II-A). These sands are pressure sensitive and decrease further to $V_p/V_s \approx 2.4$ at a differential pressure of 2175 psi (Stage II-B). The V_p - V_s ratio shows slight hysteresis with pressure: after pressurization at (Stage II-C), V_p - V_s ratio is 2.8 as compared to V_p - V_s ratio = 3 before pressurization (Stage II-A). The V_p - V_s ratio in the clean sand samples after hydrate dissociation (Stage III-A) are also slightly lower than the V_p - V_s ratios in Stage I before hydrate formation. Increasing the differential pressure to 2175 psi (Stage III-B) results in a decrease of V_p - V_s ratios to about 2.7, comparable to the pressurized 40 and 60% THF hydrate-bearing samples at Stage II-C.

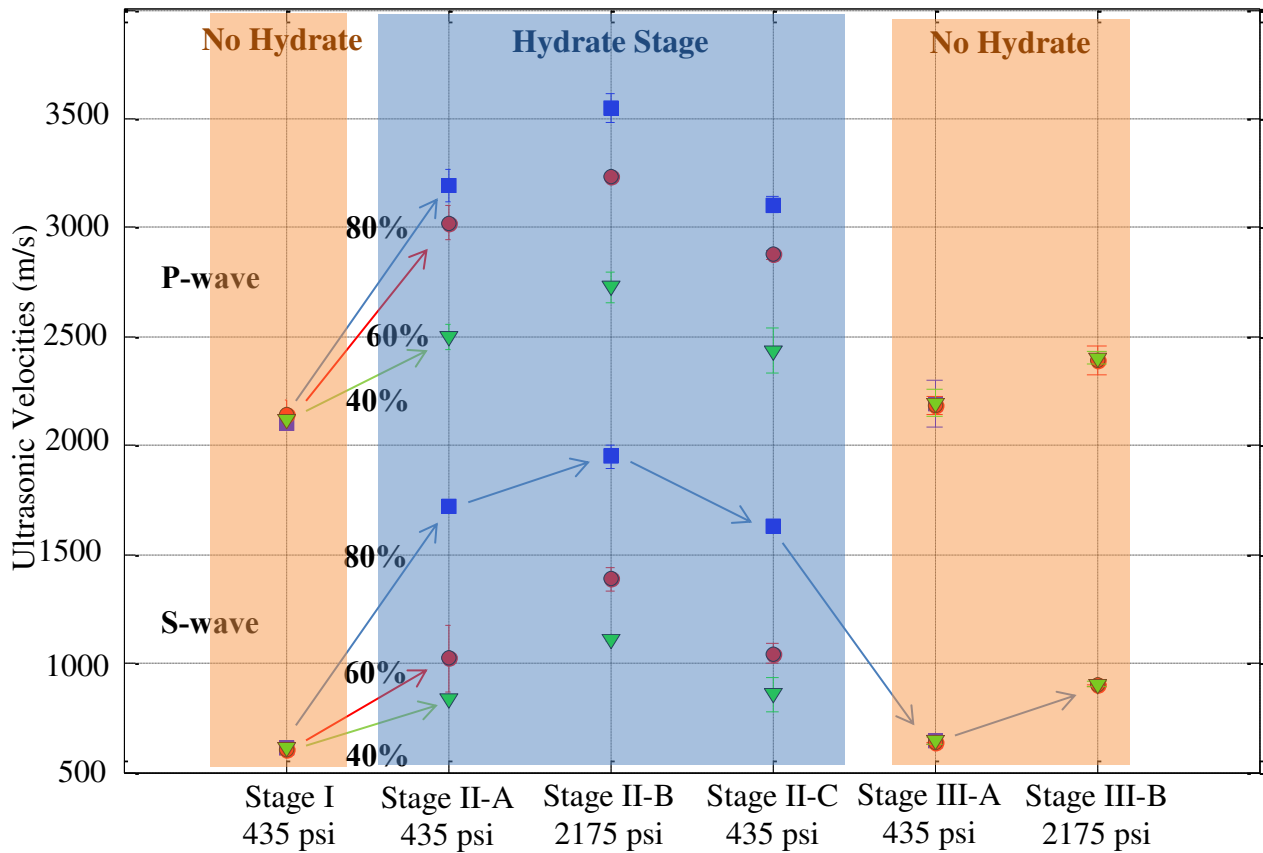


Figure 3-2 P- and S-wave velocities before and after hydrate formation for different hydrate saturation (0, 40, 60, and 80%) and at different differential pressures (435 and 2175 psi) in pure sand samples. Each sample was first measured at 435 psi differential pressure and at room temperatures (Stage I). Stage II was measured with hydrates in the sediment, while Stages I and III were measured in the host sediment before and after hydrate formation, respectively.

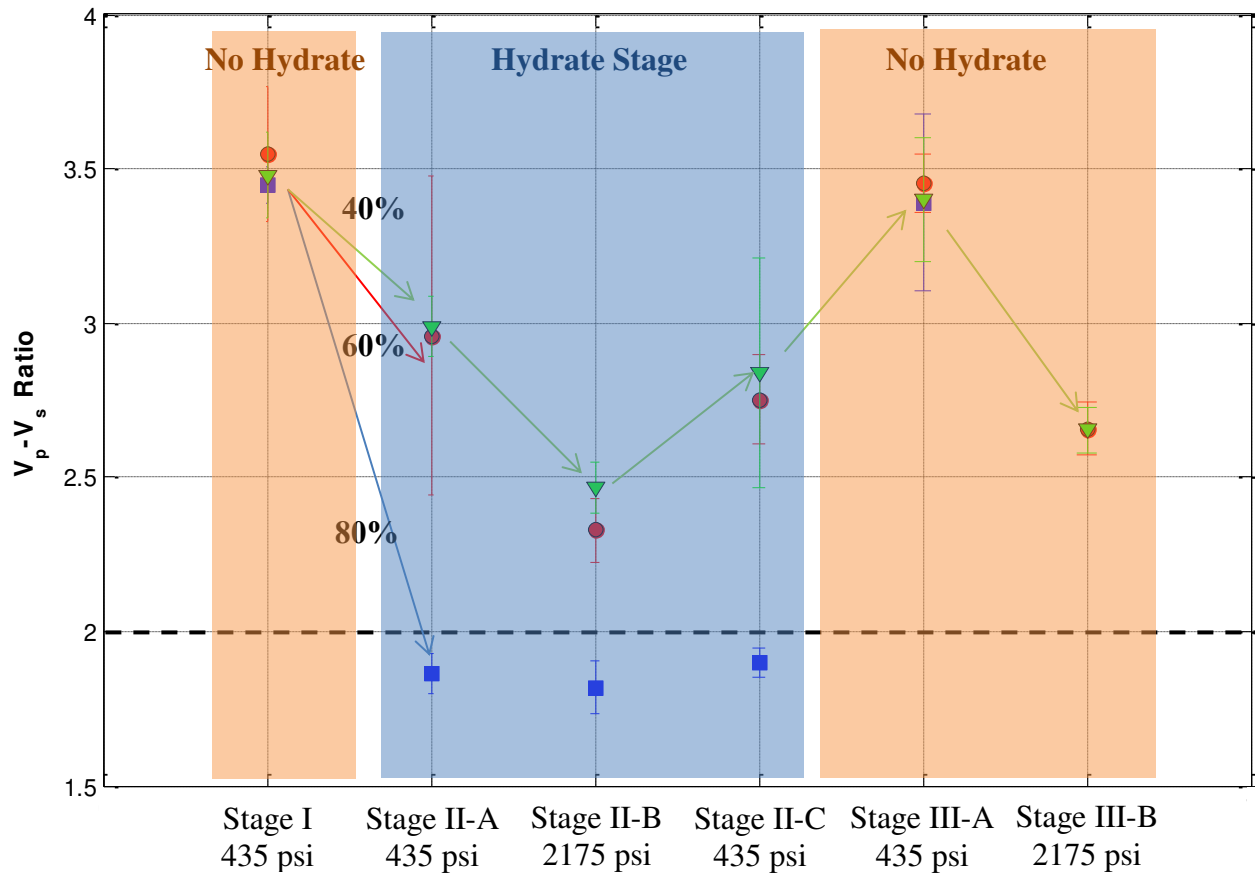


Figure 3-3 V_p - V_s ratio changes before and after hydrate formation for different hydrate saturation (0%, 40% (green triangles), 60% (red circles), and 80% (blue squares)) and at different confining pressures (435 psi and 2175 psi). Samples are considered consolidated if they fall below the dotted line (V_p - V_s ratio < 2). Note that the stages mentioned here are the same as in Figure 3-2.

Sand-Clay mixtures

In the following we are going to look how clay effects the calculated ultrasonic velocities with varying hydrate saturations. We are only going to focus at Stages I, II-A, II-B as no significant observations occurred during the last three stages. For completeness, the data for Stages II-C, III-A, and III-C can be found in Appendix A.

V_p and V_s for three sand-clay mixtures with 0, 10, and 30 wt% and with a THF-water mixture ratio to yield 80% THF hydrate saturation (Figure 3-4), 60% THF hydrate saturation (Figure 3-5), and 40% THF hydrate saturation (Figure 3-6) are plotted as a function of porosity for different temperature and pressure conditions. Without hydrates, V_p and V_s decrease with addition of 10 wt% clay but with higher amount of clay (30 wt%), V_p and V_s increase independent of THF-water mixture ratios.

All velocities increase when hydrates are formed, the largest increase is observed after the formation of 80% hydrate - ~52% increase in V_p and ~ 180% increase in V_s - regardless of clay content. Clean sands show the largest change in velocities with pressure. The pressure dependence reduces with increasing clay content. Adding clay has limited influence on the V_p-V_s ratio of hydrate free samples (Figure 3-7 a, b, and c). The V_p-V_s ratio for 80% hydrate in clean sands and sand-clay mixtures is below 2 and is again independent of clay content.

For hydrate saturations below 80%, calculated P- and S-wave velocities are dependent on clay content. A reduced increase in P-wave velocities can be seen with the addition of clay. A further increase in clay content does not result in an additional reduction in velocity. The S-wave velocity shows first an increase in velocities with the addition of clay (10 wt%) and a decrease with higher clay amounts (30 wt%). V_p-V_s ratios for lower hydrate saturations (40, 60%) show a decrease when clay is added when compared to clean sand.

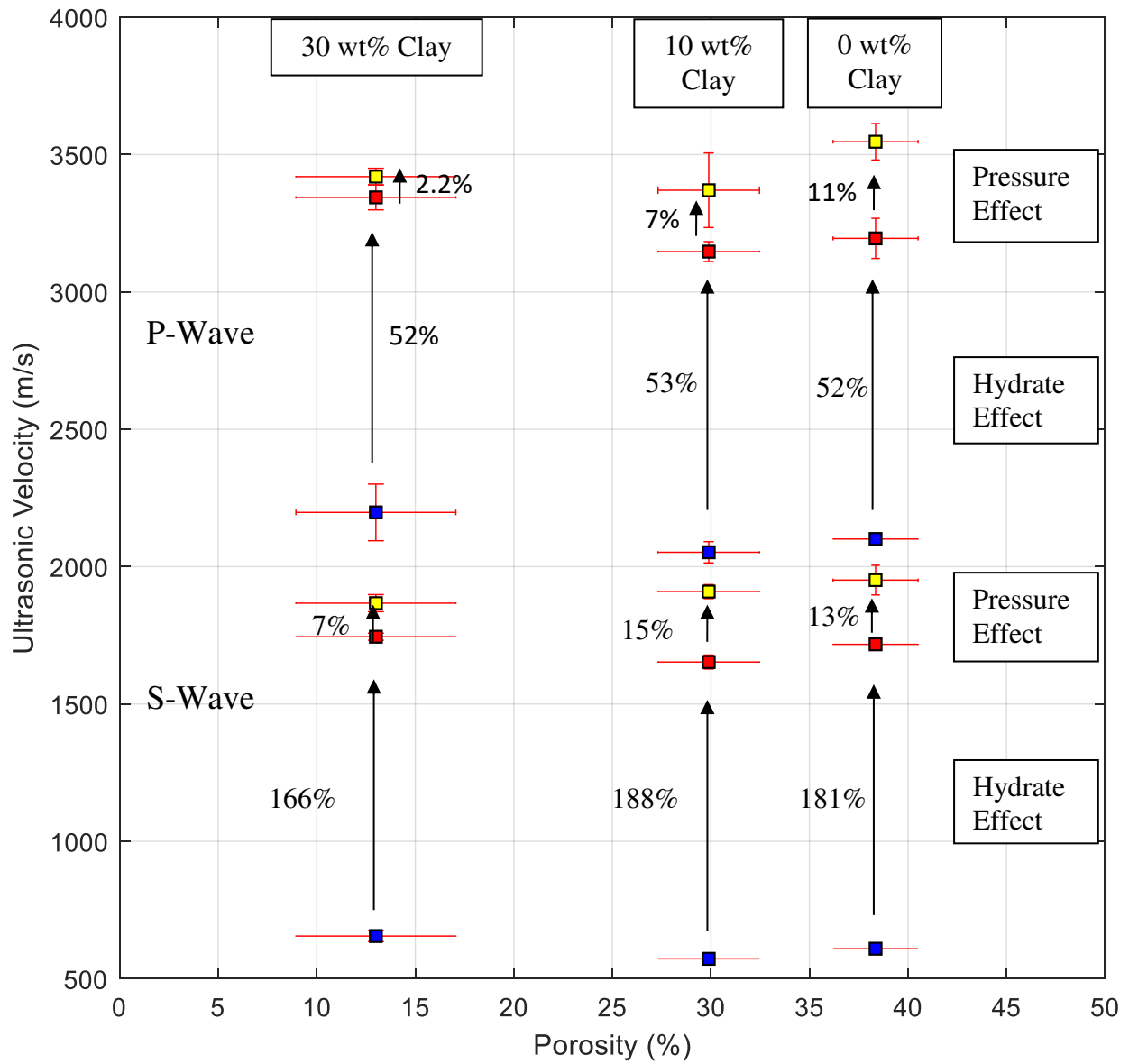


Figure 3-4 Compressional (squares) and shear (circles) wave velocities as a function of porosity for samples with 0, 10, and 30 wt% clay before and after THF hydrate formation for 80% THF hydrate saturation. Percentages given are a proportional change in velocity.

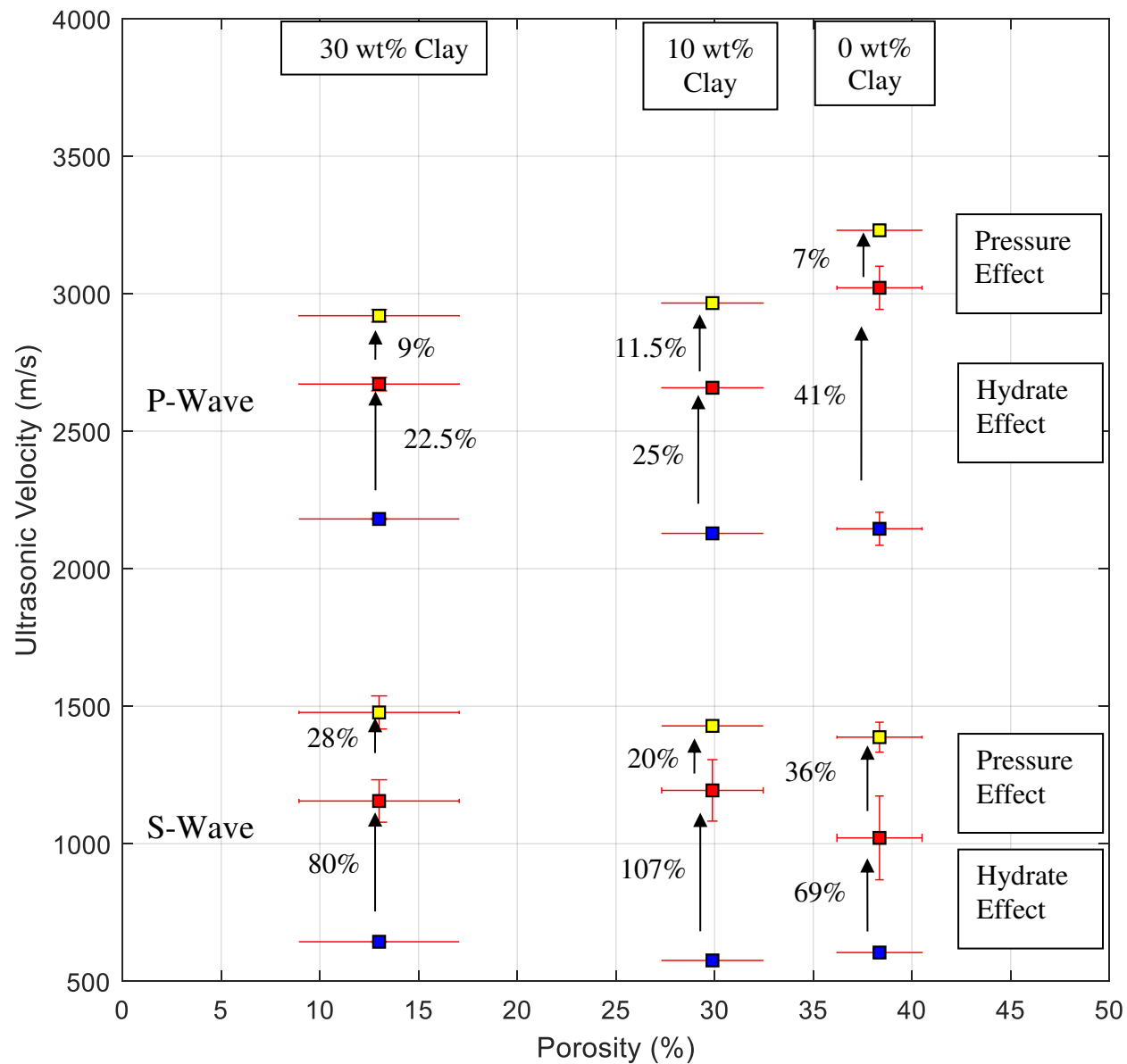


Figure 3-5 Compressional (squares) and shear (circles) wave velocities as a function of porosity for samples with 0, 10, and 30 wt% clay before and after THF hydrate formation for 60% THF hydrate saturation. Percentages given are a proportional change in velocity.

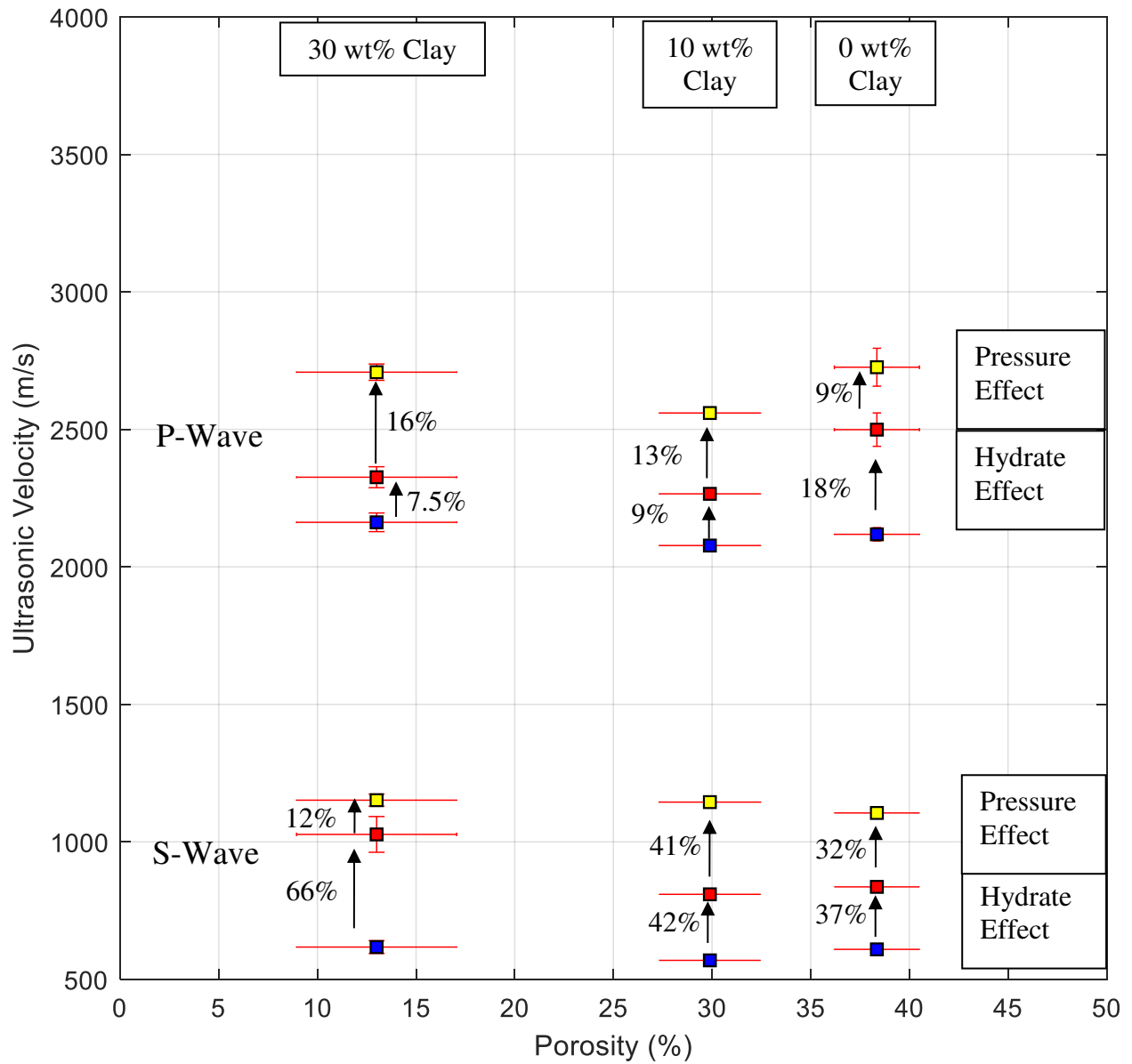


Figure 3-6 Compressional (squares) and shear (circles) wave velocities as a function of porosity for samples with 0, 10, and 30 wt% clay before and after THF hydrate formation for 40% THF hydrate saturation. Percentages given are a proportional change in velocity.

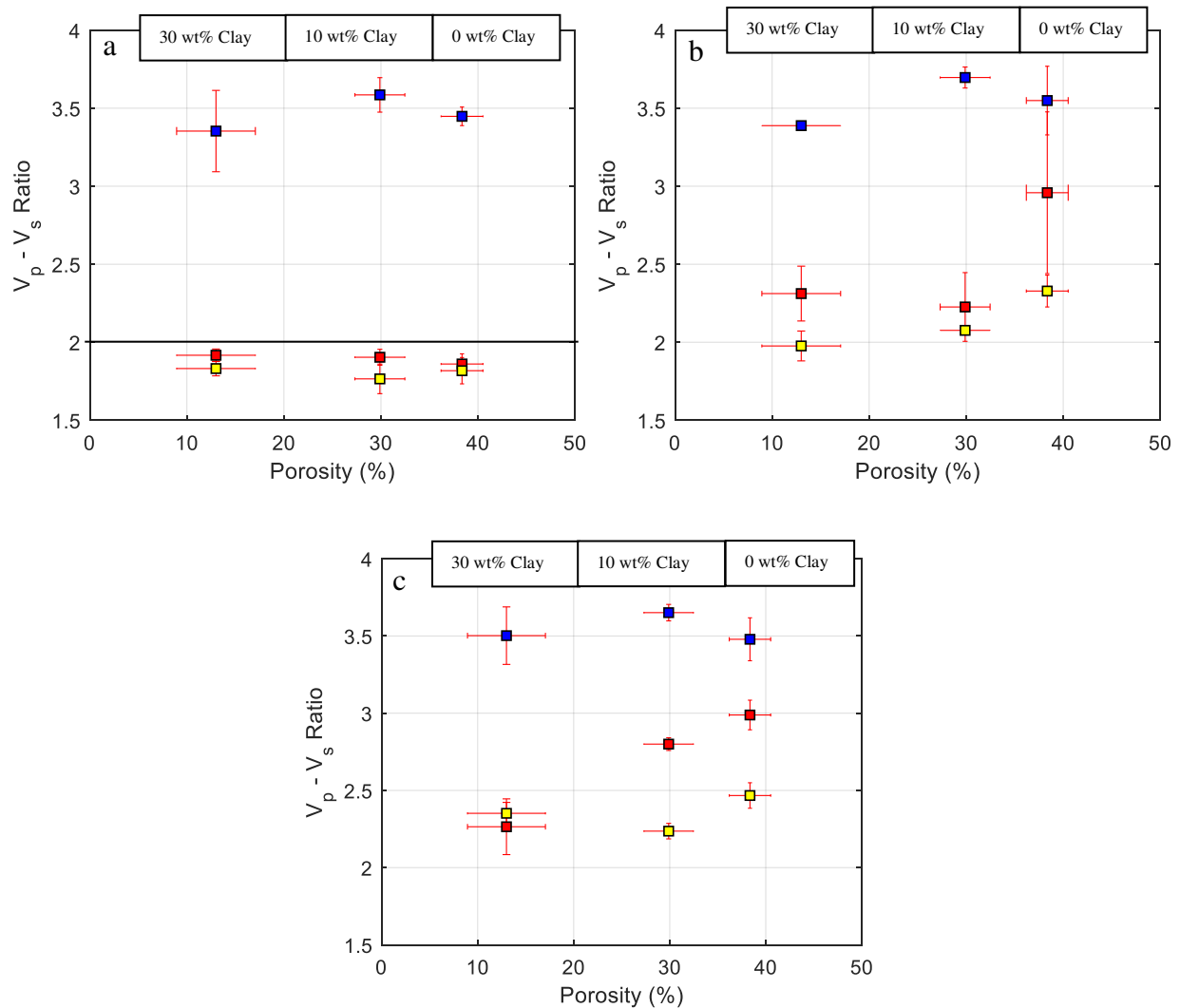


Figure 3-7 $V_p - V_s$ ratios for samples containing 30, 10 and 0 wt% of clay for samples containing:
 (a) 80% THF hydrate
 (b) 60% THF hydrate, and
 (c) 40% THF hydrate.

The solid line in (a) marks $V_p - V_s$ ratio of 2 and corresponds to the consolidation line. Blue squares are THF-water mixture saturated samples (Stage I), Red squares are THF hydrate saturated samples (Stage II-A), and Yellow squares are THF hydrate saturated samples at 2175 psi confining pressure (Stage II-B).

3.4.2 Ultrasonic Attenuation Measurements

Clean Sand

The P- and S-wave quality factors, Q_p and Q_s respectively (Figure 3-8) show a small decrease in Q_p (blue symbols) and a larger decrease in Q_s (red symbols) after hydrate formation in all the samples from Stage I to Stage II-A. After hydrate formation occurred, the quality factors for the samples that contain 80% hydrate saturation (Figure 3-8 a) do not show a change with pressures.

For samples with 60% hydrate saturation (Figure 3-8 b), we observe a small increase in Q_s during Stage II-B where the confining pressure is increased to 2275 psi and a small decrease back to Stage II-A values after the pressure was lowered back to the initial confining pressure of 535 psi (Stage II-C). Q_p however, did not change during this pressure cycle.

Samples with 40% hydrate saturation (Figure 3-8 c) show the largest changes due to pressure while hydrates are present. We observed that Q_s doubled due to the confining pressure increase (~ 7 at 535 psi to ~15 at 2275 psi). After hydrate dissociation (Stage III-A), Q_s and Q_p values were higher compared to the beginning of the experiment for samples that contained lower hydrate saturation (40 and 60%). The changes in Q_s are most drastic for samples with lower hydrate saturation (40%). After increase of confining pressure to 2275 psi in Stage III-B, we observed a large increase in Q_s for the now non-hydrate-bearing samples whereas Q_p did not change significantly.

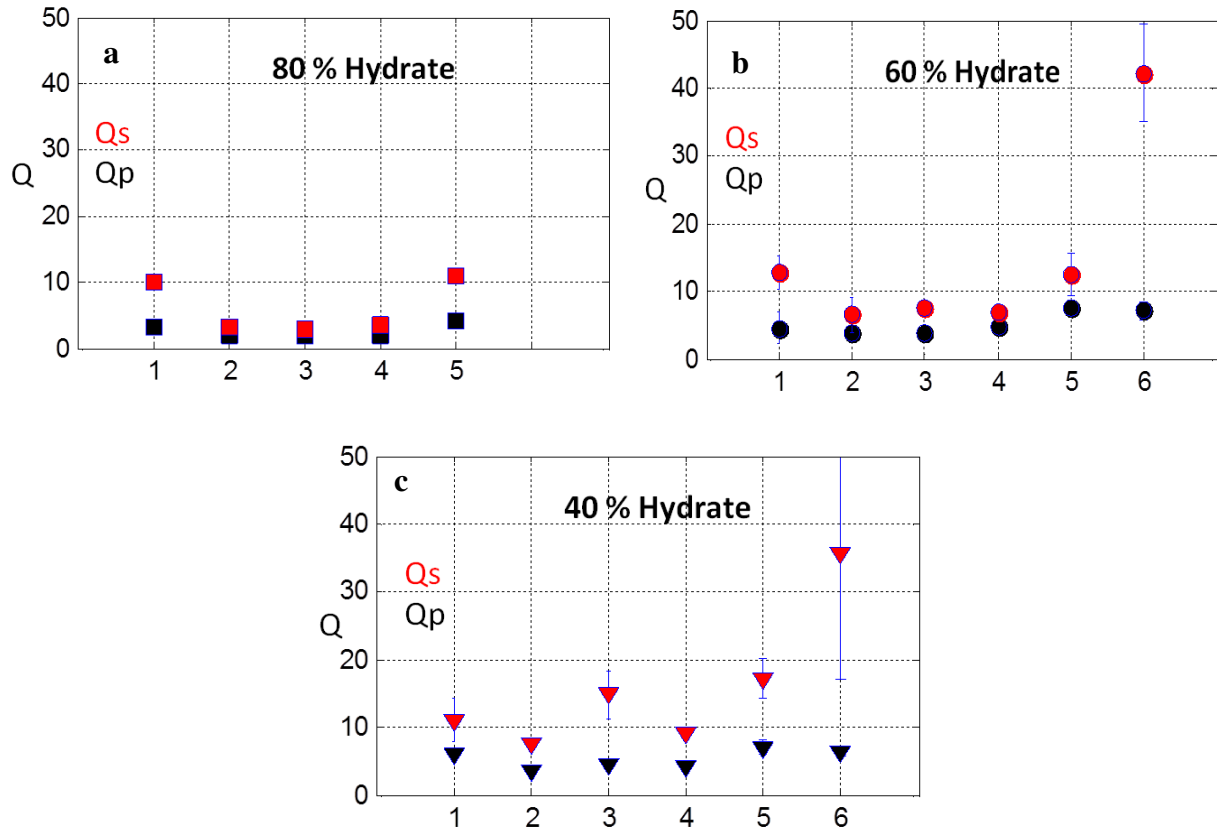


Figure 3-8 Qp and Qs values for clean sand samples containing 80 (a), 60 (b), and 40% (c) hydrate saturation. For all three plots, the numbers on the x-axis correspond to the stages:

- 1 = Stage I – sample at $P_d=435$ psi, THF-water saturated, at 24°C ,
- 2 = Stage II-A – sample at $P_d=435$ psi, hydrate bearing, at 0.5°C ,
- 3 = Stage II-B – sample at $P_d=2175$ psi, hydrate bearing, at 0.5°C ,
- 4 = Stage II-C – sample at $P_d=435$ psi, hydrate bearing, at 0.5°C ,
- 5 = Stage III-A – sample at $P_d=435$ psi, THF-water saturated, at 24°C ,
- 6 = Stage III-B – sample at $P_d=2175$ psi, THF-water saturated, at 24°C

Sand-Clay Mixture

Q_p and Q_s results before hydrate formation (yellow squares) and after hydrate dissociation (yellow triangle) for clean sand and sand-clay mixtures containing THF-water mixture that results in 80% THF hydrate saturation are presented in Figure 3-9. With increasing clay content Q_p and Q_s are decreasing before THF hydrate formation occurred (yellow squares). Stages II-A, II-B, II-C (the hydrate-bearing stages) are represented by the blue symbols for various clay contents (0, 10, and 30 wt%) and confining pressure stages (535 and 2275 psi). Comparing the Q values from the beginning of the experiment (Stage I; yellow squares) with the values at the end of the experiment (Stage III-A; yellow triangles), Q_p increased to values around 4, Q_s also increased but still shows a stronger dependence with regard to the clay content. The quality factors for the samples containing 80% THF hydrate are independent of clay content (Figure 3-9). A similar analysis for samples containing lower amounts of hydrate saturation (60 and 40%) was inconclusive in sand-clay mixtures. However, a visual analysis of the raw waveforms is provided in Appendix B.

3.5 Discussion

3.5.1 Ultrasonic Velocities

Our ultrasonic velocity measurements with varying hydrate saturation in clean Ottawa Sand F110 agree with results from Yun et al. (2005) showing repeatability and consistency of results, independent of methodology.

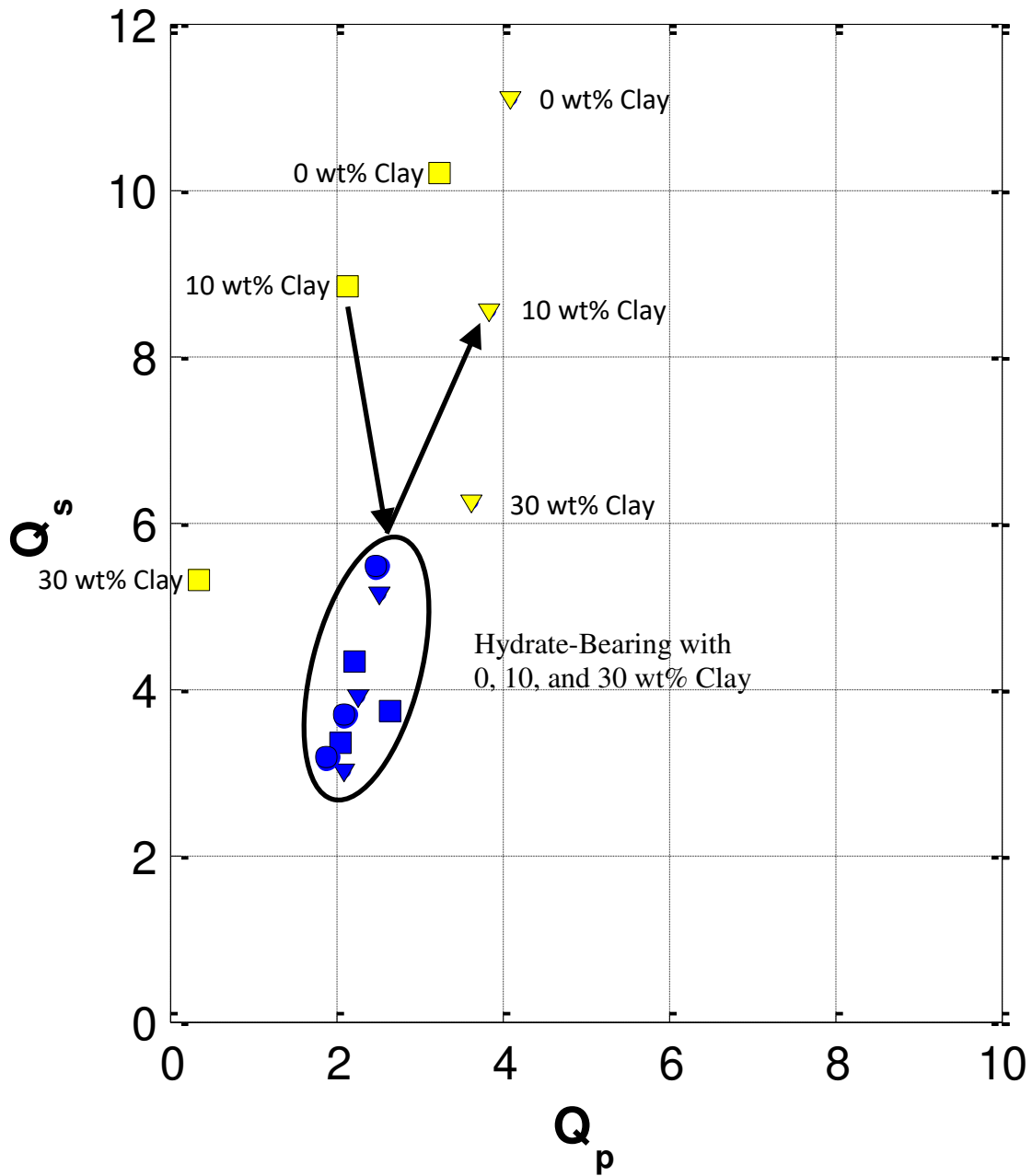


Figure 3-9 Seismic losses (Q_s and Q_p) in sands containing various amounts of clay (0, 10, and 30 wt%) before hydrate formation (yellow squares) and after hydrate dissociation (yellow triangles). Note the significant difference between the sands without hydrates (yellow symbols) and with 80% hydrate saturation (blue symbols).

After hydrate formation (Stage II-A) in clean sand samples, there is a significant increase in P-wave velocity for the samples containing 80% THF hydrate (Figure 3-2). This increase in P-wave velocity could be explained with the hydrates forming a framework and in effect consolidating the sample. The hydrate framework becomes the main load-bearer as it encases the quartz grains. This is supported by the V_p - V_s ratios (Figure 3-3). Ratios < 2 are characteristic for well-consolidated or gas-saturated unconsolidated rocks, V_p - V_s ratios > 2 are typical for water-saturated (in our case THF-water mixture) unconsolidated sediments (Gardner and Harris, 1968). An increase in confining pressure causes a decrease in V_p - V_s ratios for the lower hydrate-bearing sediments but not enough to consolidate these clean sand samples. The 80% THF hydrate-bearing samples, containing clay, have V_p - V_s ratios below 2 (Figure 3-7 a); therefore they are also considered consolidated indicating that the consolidating effect of these samples is not dependent on clay content.

The lower THF hydrate-bearing samples are sensitive to clay content shown by a significant decrease in V_p - V_s ratios (Figure 3-7 b and c). Adding confining pressure to the hydrate effect further decreases the V_p - V_s ratio, except for the V_p - V_s ratio of 40% THF hydrate-bearing sample containing 30 wt% clay. In the case of 60% THF hydrate-bearing sample containing clay, the values are bordering the consolidation line. Considering the P- and S-waves (Figure 3-5 and Figure 3-6) it becomes clear that by adding clay there is a compressional weakening and/or shear strengthening effect occurring compared to clean sands. A possible explanation could be that when THF hydrates start to form, they potentially create a hydrate structure that has clay particles within. The shear strengthening observed in the S-waves indicates that, with the addition of clay, the grain matrix is more rigid when hydrates form. The compressional weakening observed in the P-waves,

on the other hand, indicates that the clay particles within the structure formed by the hydrates cause softening of the matrix.

CT-imaging can provide a better understanding on the effects of clay on the matrix by revealing how the clay is distributed in the THF-water saturated samples. In the fluid-saturated stage, the clay pellets completely disaggregate and are dispensed in the pore fluid (Figure 3-c). For low clay content (10 wt%), the clay particles are part of the pore fluid, causing a softening of the quartz grain matrix which is observed as a decreased P- and S-wave velocity. With larger clay amounts (30 wt%), the clay starts to support the grain matrix which results in an increase in P- and S-wave velocities. The simultaneous decrease in porosity and increase in velocity observed is due to the clays filling up the pore space as was also observed by Marion et al. (1992).

The decrease in velocity after a decrease in confining pressure on the hydrate-bearing clean sand samples (Stage II-C) lead to an overall decrease in P- and S-wave velocities to below the observed values in Stage II-A (Figure 3-2). This is most likely caused by a loss of structural integrity of the hydrate framework after it got damaged during the relaxation that happened after the high-pressure phase (Stage II-B to II-C). Consolidated rock samples that are brought up to elevated pressures and subsequently unloaded to low pressures show an increase in velocity. This effect is called hysteresis. The hydrate framework in high hydrate saturation clean sand samples, however, is compliant and therefore deforms permanently during the high-pressure phase. During unloading, the grain matrix relaxes, but the hydrate matrix stays in its deformed stage therefore potentially breaking internal and external connections. This would cause the observed decrease in ultrasonic velocities. However, the two exceptions are the S-wave velocities for 40 and 60% THF hydrate saturation where the resulting velocities are marginally higher. During the compression, the hydrate framework is not the dominant load-bearer and can, therefore, compress without

deforming. The grain matrix, however, experiences slight hysteresis due to compaction. Therefore, the S-wave velocities for 40 and 60% THF hydrate saturation show a slight increase.

After hydrate dissociation and elevated confining pressures (Stage III-B), there is an increase in P- and S-wave velocities observed in the clean sand samples (Figure 3-2). This increase is in the same order as that of the 40% THF hydrate-bearing clean sand sample at low confining pressures (Stages II-A and II-C). V_p - V_s ratios at Stage III-B are comparable to lower hydrate-bearing samples (40 and 60%) at Stages II-A and II-C. It is very important to take this into consideration when looking at field data if it is unknown whether the area of interest is under high pressure or contains hydrates, as one cannot distinguish the difference by looking at the P- and S-wave velocities. In the following section, we investigate if attenuation could provide more information regarding hydrate saturation.

3.5.2 Ultrasonic Attenuation

In general, clean sandstones at atmospheric pressure and temperature have Q_p values of around 20, depending on the type of sandstone, for example, dry Berea Sandstone (Toksöz et al., 1979). With increasing confining pressure (to 5000 psi) Q_p increases to ~ 100 for dry Berea Sandstone (Toksöz et al., 1979). For unconsolidated wet sands however, Q_p decreases with increasing confining pressure whereas Q_s increases with increasing confining pressure (Dvorkin et al., 2014). In this work, we observe that Q_s increases (~ 10 to ~ 40) with increasing confining pressure, on the other hand, Q_p does not decrease significantly with increasing confining pressure (Figure 3-8). Increasing the confining pressure leads to an increase in contact radius of the grains and a denser packing which leads to an increase in shear strength resulting in higher Q_s (Prasad and Meissner, 1992). The uncertainties in the quality factor values are such that the Q_p and Q_s

values can be used for relative comparison rather than comparison to absolute values found in literature, and are therefore indicative of processes.

After hydrate formation, the pressure sensitivity of Q_s depends on hydrate saturation; a lower hydrate saturation results in a greater change of Q_s after 2275 psi confining pressure is applied (Figure 3-8). Recent studies have shown that methane hydrate formation (Kerkar et al., 2014), as well as THF hydrate formation (Schindler et al., 2017), takes place in the pore space, away from the grains. This leads to a different hydrate-sediment interaction than if the hydrate had formed along the grain surfaces. Increasing the pressure in the absence of hydrates results in compaction and increase of contact surface of the grains resulting in shear stiffening as discussed before. After hydrate formation, the sample structure is partially supported by the hydrate framework, reducing the effects of elevated confining pressures on compaction. At 40% THF hydrate saturation, connectivity within the hydrate framework decreases compared to samples with 80% THF hydrate saturation, and is therefore more sensitive to elevated pressures (Figure 3-8 a and c). At 80% THF hydrate saturation, the hydrate framework can withstand a confining pressure increase. Therefore Q_p and Q_s are unaffected. This is in agreement with the observations made on the sample with 80% THF hydrate saturation where the V_p - V_s ratios reveal a consolidated sample indicating that the hydrate framework dominates the sample structure. This is further evidenced by plotting Q_s versus Q_p (Figure 3-9) for varying clay content. After forming 80% THF hydrate in sand-clay mixtures the Q_p and Q_s are no longer sensitive to the presence of clay or confining pressure. This is in agreement with the previous statement, that clay content has only minimal effects on the V_p - V_s ratios with 80% THF hydrate saturation.

Another aspect to note is that a plot of Q_s versus Q_p shows a significant change in Q_s and Q_p with increasing clay content (Figure 3-9). The change in Q_s is caused by the softening effect

of the clay on the grain matrix. The significant change in Q_p could be caused by air bubbles remaining in the sample after vacuuming. Over the course of the experiment, this remnant air might have dissolved into the pore fluid, which resulted in higher Q values. Another explanation could be that the dispersed clay within the pore fluid (Figure 3-2c) has undergone some changes that are below the detectable resolution of the μ CT-Scanner used. Although dispersed, small (soft) aggregates of clay particles might still be present in the pore fluid and could undergo compaction due to the volumetric expansion of THF hydrates of $\sim 7\%$ (Lee et al., 2007). This volumetric expansion could cause a collapsing of the soft clay aggregates to a denser particle or pushing the clay particles against the quartz grains resulting in a stronger quartz – clay grain contact. Scattering in the data pertaining to lower THF hydrate-bearing (40 and 60%) sand-clay mixture samples prevent any trends from being observed in a Q_s versus Q_p plot and are therefore not shown here (see Appendix B).

3.6 Conclusions

Our results for hydrate-bearing clean Ottawa Sand F110 are comparable with literature data. We find that:

- Hydrate formation in any sediment (clean sand, sand-clay) causes an increase in P- and S-wave velocities.
- The pressure dependence of velocities decreases with increasing hydrate saturation and clay content.
- At high hydrate saturation (80%), V_p - V_s ratio mimics cemented sandstones, independent of clay content.
- Hydrate formation in clean sand causes a decrease in Q_p and Q_s

- Q_s is strongly pressure dependent; this pressure dependence is inversely proportional to hydrate saturation. Changes in Q_p are small and less conclusive.

Our results of the effects of clay content and pressure on hydrate-bearing sediments show that a lack of knowledge about the pressure conditions could lead to errors in estimates of hydrate saturation when interpreting field data.

3.7 Acknowledgement

This material is based upon work supported by the U.S. Department of Energy, Office of Science, Office of Fossil Energy, under Award Number DE-FE 0009963. Thanks to Mandy Schindler for acquiring the CT-images.

3.8 References

- Boswell, R., & Collett, T. (2011), Current perspectives on gas hydrate resources. *Energy Environ. Sci.*, 4, 1206–1215.
- Chand, S., and T. A. Minshull (2004), The effect of hydrate content on seismic attenuation: A case study for Mallik 2L-38 well data, Mackenzie delta, Canada, *Geophys. Res. Lett.*, 31, L14609, doi:10.1029/2004GL020292.
- Chaouachi, M., Falenty, A., Sell, K., Enzmann, F., Kersten, M., Haberthür, D., & Kuhs, W. F. (2015). Microstructural evolution of gas hydrates in sedimentary matrices observed with synchrotron X-ray computed tomographic microscopy. *Geochemistry, Geophysics, Geosystems*, 16(6), 1711–1722. <https://doi.org/10.1002/2015GC005811>
- Collett, T.S., 2000, Quantitative well-log analysis of in-situ gas hydrates, Ph.D. Thesis, Colorado School of Mines, Golden, Colorado
- Collett, T. (2002), Energy resource potential of natural gas hydrate, *Am. Assoc. Pet. Geol. Bull.*, 86, 1971–1992
- Dewangan P., Mandal R., Jaiswal P., Ramprasad T., Sriram G., (2014) Estimation of seismic attenuation of gas hydrate bearing sediments from multi-channel seismic data: A case study

- from Krishna–Godavari offshore basin. *Marine and Petroleum Geology* 58, 356-367. <https://library.seg.org/doi/abs/10.1190/1.1440520?journalCode=gpya7>
- Dvorkin, J., Gutierrez, M., & Grana, D. (2014). *Seismic Reflections of Rock Properties*. Cambridge: Cambridge University Press. doi:10.1017/CBO9780511843655
- Dvorkin, J. R. Uden (2004), “Seismic wave attenuation in a methane hydrate reservoir” *The Leading Edge Interpreter’s Corner*
- Gardner, G.H.F., and Harris, M.H., 1968, Velocity and attenuation of elastic waves in sands: Society of Professional Well Log Analysts, Transactions, 9th Annual Log Symposium, p. M1–M19
- Guerin, G., and Goldberg, D., (2002). Sonic waveform attenuation in gas hydrate-bearing sediments from the Mallik 2L-38 research well, MacKenzie Delta, Canada. *J. Geophys. Res.*, 107:2088. doi:10.1029/2001JB000556
- Helgerud, M.B., W.F. Waite, S.H. Kirby, and A. Nur, 2009, “Elastic wave speeds and moduli in polycrystalline ice Ih, sI methane hydrate and sII methane-ethane hydrate”, *Journal of Geophysical Research* 114, B02212
- Jyothi, V., Sain, K., Pandey, V. (2017), Seismic attenuation for characterization of gas hydrate reservoir in Krishna-Godavari basin, eastern Indian margin. *Journal of the Geological Society of India*. 90. 261-266. 10.1007/s12594-017-0713-9.
- Kerker, P. B., K. Horvat, K. W. Jones, and D. Mahajan (2014), Imaging methane hydrates growth dynamics in porous media using synchrotron X-ray computed microtomography, *Geochem. Geophys. Geosyst.*, 15, 4759–4768, doi:10.1002/2014GC005373.
- Klimentos, T. and McCann, C., (1990), Relationships between compressional wave attenuation, porosity, clay content, and permeability of sandstone: *Geophysics*, v. 55, p. 998-1014.
- Koesoemadinat A.P. and McMechan G.A., (2001). Empirical estimation of viscoelastic seismic parameters from petrophysical properties of sandstone, *Geophysics*, 66, 1340–1649.
- Kunert, D.C., D.M. Weinberg, J.W. Rector III, C.L. Scott, and J.T. Johnson, 2001, *Journal of Seismic Exploration* 9, 337
- Kvenvolden, K. A. (1999), Potential effects of gas hydrate on human welfare, *Proc. Natl. Acad. Sci. U.S.A.*, 96(7), 3420–3426.
- Lee, J. Y., Yun, T. S., Santamarina, J. C., Ruppel, C. (2007). “Observations Related to Tetrahydrofuran and Methane Hydrates for Laboratory Studies of Hydrate-Bearing

Sediments” Geochemistry Geophysics Geosystems An Electronic Journal of the Earth Sciences, 8 (6)

- Lee, J. Y., F. M. Francisca, J. C. Santamarina, and C. Ruppel (2010), “Parametric study of the physical properties of hydrate-bearing sand, silt, and clay sediments: 2. Small-strain mechanical properties”, *Journal of Geophysical Research*, Vol. 115, B11105, doi:10.1029/2009JB006670
- Marion, D., A. Nur, H. Yin, and D. Han, 1992, Compressional velocity and porosity in sand-clay mixtures: *Geophysics*, 57, no. 4, 554–563, <http://dx.doi.org/10.1190/1.1443269>.
- Maslin, M., Owen, M., Betts, R., Day, S., Jones, T.D., & Ridgwell, A. (2010), Gas hydrates: Past and future geohazard? *Proc. R. Soc. A*, 368(1919), 2369–2393.
- Mohan, K. K., R. N. Vaidya, M. G. Reed, and H. S. Fogler, “Water Sensitivity of Sandstones Containing Swelling and Non-Swelling Clays,” *Colloids Surf A; Physicochem. Eng. Aspects*, 73, 237 (1993).
- Pearson, C., Murphy, J. and Hermes, R. (1986). Acoustic and resistivity measurements on rock samples containing tetrahydrofuran hydrates: laboratory analogues to natural gas hydrate deposits. *Journal of Geophysical Research* 91: doi: 10.1029/JB080i014p14132. issn: 0148-0227.
- Prasad, M. and R. Meissner, (1992), Attenuation mechanisms in sands: Laboratory versus theoretical Biot data, *Geophysics* 57, 710–719
- R.G. Pratt, F. Hou, K. Bauer, M. Weber, (2005), Waveform tomography images of velocity and inelastic attenuation from the Mallik 2002 crosshole seismic surveys *Bull. Geol. Surv. Can.*, pp. 1-14
- Priest, J.A., E.V.L. Rees, and C.R.I. Clayton (2009), “Influence of gas hydrate morphology on the seismic velocities of sands”, *Journal of Geophysical Research*, 114, B1120
- Ruppel, C. (2007), Tapping methane hydrates for unconventional natural gas, *Elements*, 3(3), 193–199
- Rydz, M. B. (2013) “Effect of Hydrate Formation on the Elastic Properties of Unconsolidated Sands”. Ph.D. Thesis, Colorado School of Mines, Golden, CO
- Sahoo, S. K., Madhusudhan, B. N., Marín-Moreno, H., North, L. J., Ahmed, S., Falcon-Suarez, I. H., Minshull, T. A., & Best, A. I. (2018). Laboratory insights into the effect of sediment-hosted methane hydrate morphology on elastic wave velocity from time-lapse 4D synchrotron X-ray computed tomography. *Geochemistry, Geophysics, Geosystems*, 19. <https://doi.org/10.1029/2018GC007710>

- Sell, K., Quintal, B., Kersten, M., & Saenger, E. H. (2018). Squirt flow due to interfacial water films in hydrate bearing sediments. *Solid Earth*, 9(3), 699–711. <https://doi.org/10.5194/se-9-699-2018>
- Schindler, M., Batzle, M. L. and Prasad, M. (2017), Micro X-Ray computed tomography imaging and ultrasonic velocity measurements in tetrahydrofuran-hydrate-bearing sediments. *Geophysical Prospecting*, 65: 1025–1036. doi:10.1111/1365-2478.12449
- Sloan, E. D. & Koh, C. A. (2007), *Clathrate Hydrates of Natural Gases*. 3rd ed., CRC Press, Taylor & Francis Group, Boca Raton, FL
- Spangenberg, E., J. Kuhlenkampff, R. Naumann, and J. Erzinger (2005), “Pore-space hydrate formation in a glass bead sample from methane dissolved in water”, *Journal of Geophysical Research*, 32, L24301
- Suzuki, H., and J. Matsuhima, (2013), Quantifying uncertainties in attenuation estimation at methane-hydrate-bearing zones using sonic waveform logs: *Geophysics*, 78, no. 5, D339–D353, doi: 10.1190/geo2012-0495.1
- Toksöz, M.N., Johnston, D.H., and Timur, A., (1979), Attenuation of seismic waves in dry and saturated rocks: 1. Laboratory measurement; *Geophysics*, 44, 681-690.
- Waite, W. F., Winters, W. J., Mason, D. H. (2004). “Methane Hydrate Formation in Partially Water-Saturated Ottawa Sand.” *American Mineralogist*, 89: 1221-1227
- Waite, W.F., Santamarina, J.C., Rydzy, M., Chong, S.H., Grozic, J.L.H., Hester, K.C., Howard, J., Kneafsey, T.J., Lee, J.Y., Nakagawa, S., Priest, J., Rees, E., Koh, C.A., Sloan, E.D., Sultaniya, A., July 17-22, 2011. Inter-laboratory comparison of wave velocity measurements in a sand under hydrate-bearing and other Set conditions. Manuscript 195. In: Seventh International Conference on Gas Hydrates. Edinburgh, Scotland.
- Wang, D., L.D. Li, H.L. Zhang, S.S. Fan, and H.B. Zhao, 2008, Laboratory measurement of longitudinal wave velocity of artificial gas hydrate under different temperatures and pressures, *Science in China Series G: Physics, Mechanics, and Astronomy* 51(12), 1,905-1,913
- Wood, W.T., Holbrook, W.S. & Hoskins, H., (2000), “In situ measurements of P-wave attenuation in methane hydrate and gas bearing sediments on the Blake Ridge” *Proc. ODP. Results*, Vol 164, pp. 265-272, eds Paull, C., Matsumoto, R., Wallace, P. & others, Ocean Drilling Program, College Station, Texas
- Yun, T. S., Francisca, F. M., Santamarina, J. C., Ruppel, C (2005). “Compressional and Shear Wave Velocities in Uncemented Sediment Containing Gas Hydrate.” *Geophysical Research Letters*, Vol. 32, L10609, doi:10.1029/2005GL022607

3.9 Appendix A

Table A-1 Summary of compressional wave velocities with varying clay content and 80% THF hydrate saturation

Clay Content (wt%)	Vp (m/s) Stage I	Vp (m/s) Stage II-A	Vp (m/s) Stage II-B	Vp (m/s) Stage II-C	Vp (m/s) Stage III-A	Vp (m/s) Stage III-C
0	2101 ± 17	3194 ± 73	3546 ± 66	3103 ± 37	2190 ± 109	NA
10	2052 ± 38	3146 ± 36	3370 ± 135	3079 ± 17	2112 ± 49	NA
30	2197 ± 103	3344 ± 45	3419 ± 30	3363 ± 39	2253 ± 113	NA

Table A-2 Summary of shear wave velocities with varying clay content and 80% THF hydrate saturation

Clay Content (wt%)	Vs (m/s) Stage I	Vs (m/s) Stage II-A	Vs (m/s) Stage II-B	Vs (m/s) Stage II-C	Vs (m/s) Stage III-A	Vs (m/s) Stage III-C
0	609 ± 6	1717 ± 21	1951 ± 54	1633 ± 21	646 ± 22	NA
10	572 ± 6	1652 ± 25	1909 ± 25	1667 ± 43	644 ± 13	NA
30	655 ± 23	1744 ± 13	1867 ± 31	1816 ± 15	687 ± 11	NA

Table A-3 Summary for Vp-Vs ratio with varying clay content and 80% THF hydrate saturation

Clay Content (wt%)	Vp/Vs Stage I	Vp/Vs Stage II-A	Vp/Vs Stage II-B	Vp/Vs Stage II-C	Vp/Vs Stage III-A	Vp/Vs Stage III-B
0	3.448 ± 0.062	1.861 ± 0.065	1.818 ± 0.084	1.900 ± 0.047	3.390 ± 0.284	NA
10	3.585 ± 0.110	1.904 ± 0.049	1.765 ± 0.094	1.847 ± 0.058	3.279 ± 0.142	NA
30	3.353 ± 0.259	1.917 ± 0.040	1.832 ± 0.046	1.852 ± 0.037	3.279 ± 0.217	NA

Table A-4 Summary of compressional wave velocities with varying clay content and 60% THF hydrate saturation

Clay Content (wt%)	Vp (m/s) Stage I	Vp (m/s) Stage II-A	Vp (m/s) Stage II-B	Vp (m/s) Stage II-C	Vp (m/s) Stage III-A	Vp (m/s) Stage III-C
0	2145 ± 60	3022 ± 79	3231 ± 14	2875 ± 23	2185 ± 39	2392 ± 64
10	2129 ± 6	2658 ± 14	2966 ± 16	2692 ± 51	2163 ± 6	2392 ± 11
30	2181 ± 3	2672 ± 25	2920 ± 23	2828 ± 37	2342 ± 4	2697 ± 21

Table A-5 Summary of shear wave velocities with varying clay content and 60% THF hydrate saturation

Clay Content (wt%)	Vs (m/s) Stage I	Vs (m/s) Stage II-A	Vs (m/s) Stage II-B	Vs (m/s) Stage II-C	Vs (m/s) Stage III-A	Vs (m/s) Stage III-C
0	604 ± 20	1021 ± 152	1388 ± 55	1045 ± 48	633 ± 6	900 ± 5
10	576 ± 9	1194 ± 112	1429 ± 3	1132 ± 20	577 ± 8	993 ± 46
30	644 ± 2	1156 ± 78	1478 ± 60	1280 ± 21	750 ± 122	1055 ± 25

Table A-6 Summary for Vp-Vs ratio with varying clay content and 60% THF hydrate saturation

Clay Content (wt%)	Vp/Vs Stage I	Vp/Vs Stage II-A	Vp/Vs Stage II-B	Vp/Vs Stage II-C	Vp/Vs Stage III-A	Vp/Vs Stage III-B
0	3.549 ± 0.220	2.958 ± 0.065	2.328 ± 0.102	2.753 ± 0.147	3.452 ± 0.093	2.656 ± 0.085
10	3.697 ± 0.068	2.226 ± 0.220	2.076 ± 0.07	2.379 ± 0.085	3.749 ± 0.06	2.408 ± 0.123
30	3.388 ± 0.013	2.312 ± 0.176	1.976 ± 0.095	2.21 ± 0.064	3.120 ± 0.515	2.555 ± 0.080

Table A-7 Summary of compressional wave velocities with varying clay content and 40% THF hydrate saturation

Clay Content (wt%)	Vp (m/s) Stage I	Vp (m/s) Stage II-A	Vp (m/s) Stage II-B	Vp (m/s) Stage II-C	Vp (m/s) Stage III-A	Vp (m/s) Stage III-C
0	2118 ± 24	2499 ± 61	2726 ± 69	2432 ± 104	2193 ± 62	2401 ± 30
10	2077 ± 15	2265 ± 12	2560 ± 15	2301 ± 4	2104 ± 17	2332 ± 50
30	2162 ± 34	2326 ± 38	2708 ± 30	2396 ± 127	2252 ± 20	2584 ± 30

Table A-8 Summary of shear wave velocities with varying clay content and 40% hydrate THF saturation

Clay Content (wt%)	Vs (m/s) Stage I	Vs (m/s) Stage II-A	Vs (m/s) Stage II-B	Vs (m/s) Stage II-C	Vs (m/s) Stage III-A	Vs (m/s) Stage III-C
0	609 ± 17	836 ± 6	1105 ± 9	857 ± 75	645 ± 20	905 ± 14
10	569 ± 4	809 ± 8	1144 ± 19	807 ± 10	530 ± 4	935 ± 14
30	617 ± 23	1027 ± 65	1151 ± 22	1055 ± 25	731 ± 30	1072 ± 38

Table A-9 Summary for Vp-Vs ratios with varying clay content and 40% THF hydrate saturation

Clay Content (wt%)	Vp/Vs Stage I	Vp/Vs Stage II-A	Vp/Vs Stage II-B	Vp/Vs Stage II-C	Vp/Vs Stage III-A	Vp/Vs Stage III-B
0	3.478 ± 0.139	2.988 ± 0.095	2.467 ± 0.083	2.839 ± 0.371	3.398 ± 0.200	2.544 ± 0.074
10	3.651 ± 0.053	2.799 ± 0.041	2.236 ± 0.050	2.851 ± 0.0425	3.971 ± 0.063	2.495 ± 0.091
30	3.502 ± 0.186	2.265 ± 0.181	2.352 ± 0.071	2.270 ± 0.174	3.077 ± 0.157	2.410 ± 0.114

Table A-10 Quality factor Qp for 80% THF hydrate saturation with varying clay content.

Clay Content (wt%)	Qp Stage I	Qp Stage II-A	Qp Stage II-B	Qp Stage II-C	Qp Stage III-A	Qp Stage III-B
0	3.246 ± 0.234	2.0365 ± 0.078	2.086 ± 0.244	2.070 ± 0.152	4.096 ± 0.141	NA
10	2.132 ± 0.680	2.656 ± 0.750	2.275 ± 0.073	1.862 ± 0.117	3.821 ± 0.830	NA
30	0.330 ± 0.041	2.226 ± 0.658	2.494 ± 0.112	2.471 ± 0.462	3.608 ± 0.878	NA

Table A-11 Quality factor Qs for 80% THF hydrate saturation with varying clay content.

Clay Content (wt%)	Qs Stage I	Qp Stage II-A	Qs Stage II-B	Qs Stage II-C	Qs Stage III-A	Qs Stage III-B
0	10.171 ± 0.590	3.335 ± 0.450	2.983 ± 0.570	3.693 ± 0.056	11.086 ± 0.937	NA
10	8.835 ± 2.061	3.735 ± 0.657	3.910 ± 0.395	3.160 ± 0.261	8.530 ± 1.806	NA
30	5.282 ± 2.636	4.308 ± 1.865	5.144 ± 0.730	5.478 ± 0.025	6.254 ± 0.588	NA

Table A-12 Quality factor Qp for 60% THF hydrate saturation with varying clay content.

Clay Content (wt%)	Qp Stage I	Qp Stage II-A	Qp Stage II-B	Qp Stage II-C	Qp Stage III-A	Qp Stage III-B
0	4.555 ± 2.380	3.979 ± 0.749	3.715 ± 0.518	4.632 ± 0.106	7.460 ± 0.623	7.137 ± 1.307
10	3.722 ± 0.088	2.956 ± 0.265	5.521 ± 2.043	2.981 ± 0.170	3.419 ± 0.097	3.937 ± 0.558
30	2.340 ± 0.198	1.951 ± 0.005	1.949 ± 0.030	3.069 ± 1.267	2.518 ± 0.301	2.898 ± 0.372

Table A-13 Quality factor Qs for 60% hydrate saturation with varying clay content.

Clay Content (wt%)	Qs Stage I	Qp Stage II-A	Qs Stage II-B	Qs Stage II-C	Qs Stage III-A	Qs Stage III-B
0	12.760 ±2.400	6.530 ± 2.585	7.528 ±0.565	6.816 ± 0.869	12.479 ± 3.203	42.195 ± 7.3
10	7.246 ± 0.179	7.066 ± 2.498	4.977 ± 0.181	3.650 ± 0.453	7.187 ± 1.903	4.214 ± 1.902
30	7.230 ± 0.534	6.185 ± 2.393	7.095 ± 5.103	7.406 ± 5.025	6.577 ± 0.253	5.578 ± 0.510

Table A-14 Quality factor Qp for 40% THF hydrate saturation with varying clay content.

Clay Content (wt%)	Qp Stage I	Qp Stage II-A	Qp Stage II-B	Qp Stage II-C	Qp Stage III-A	Qp Stage III-B
0	5.912 ± 0.794	3.569 ± 0.741	4.385 ± 0.780	4.269 ± 0.215	7.022 ± 1.111	6.344 ± 0.650
10	3.352 ± 0.901	3.874 ± 1.646	3.051 ±0.550	3.114 ±0.231	3.019 ± 0.451	3.405 ± 1.087
30	3.619 ± 0.077	3.013 ± 0.153	2.465 ± 0.004	2.995 ± 0.826	4.523 ± 0.221	3.439 ± 0.679

Table A-15 Quality factor Qs for 40% THF hydrate saturation with varying clay content.

Clay Content (wt%)	Qs Stage I	Qp Stage II-A	Qs Stage II-B	Qs Stage II-C	Qs Stage III-A	Qs Stage III-B
0	10.967 ± 3.238	7.461 ±0.893	14.883 ± 3.527	9.089 ± 0.779	17.237 ± 2.943	35.771 ± 2.943
10	11.195 ± 0.971	7.063 ± 1.381	8.057 ± 3.082	6.432 ± 0.578	12.540 ± 3.337	8.488 ± 3.664
30	9.098 ± 1.848	9.382 ± 4.287	8.692 ± 5.985	7.753 ± 0.457	11.214 ± 3.624	12.589 ± 1.249

3.10 Appendix B

A closer look at the raw waveforms, for samples of varying clay content and containing 40 and 60% THF hydrate saturation, enhances the insight into the behavior of these samples under various temperature and pressure conditions. The raw waveforms of the 40% hydrate in a 30 wt% clay mixed with 70 wt% samples show that the P-waveform is significantly affected by relaxation after high confining pressure condition during the hydrate-bearing phase (Figure B-1; Stage II-B to II-C). During the experiments, the volume of the pore pressure pump was recorded. Hydrate formation was accompanied by a volumetric expansion observed in a change of volume (~ 0.02 ml) of the pore pressure pump. The increase in confining pressure from 535 psi to 2275 psi caused another increase in the pore pressure pump volume of ~ 0.3 ml. Lowering the confining pressure back to 535 psi was accompanied by a slight change of volume (< 0.05 ml) of the pore pressure pump, permanently reducing the volume of the pore space by ~ 0.25 ml resulting in a reduction in amplitude and broadening of the first wave arrival cycle of the P-waveform.

Hydrate formation (Stage II-A) causes a slight decrease in amplitude and faster arrival time for the P- and S-waveforms (Figure B-1 a to c and b to d). An increase in confining pressure (Stage II-B) results in an earlier arrival time as well as a slight recovery of the amplitudes for the P-waveform (Figure B-1 c to e) and a significant increase in amplitude for the S-waveform (Figure B-1 d to f). Interestingly, once the confining pressure was reduced back to 535 psi (Stage II-C), the P-waveforms drastically changed to a lower amplitude as well as a broader first arrival cycle (Figure B-1 c to g). In the case of the S-waveform, there is a higher amplitude signature after the reduced confining pressure conditions (Figure B-1 d to h). After hydrate dissociation (Stage III-A), the P- and S-waveforms revert to the initial amplitude observed in Stage I though with a slightly

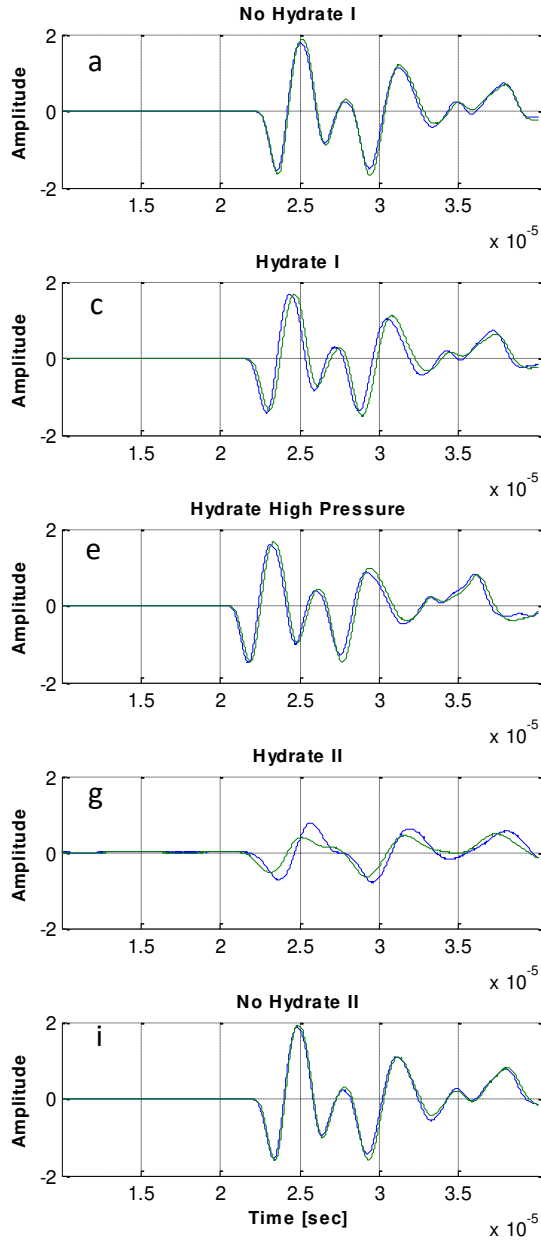
faster arrival time. The observations described above were consistent for both samples measured demonstrating repeatability.

Although V_p and V_s velocities are slightly higher after elevated confining pressures, the compaction process does not have the same effect on the P-waveform. This indicates that the observed amplitude loss in the P-wave is caused by the effects of pore space reduction. The S-waveform is not sensitive to changes in the pore space, but it is sensitive to compaction. Therefore this process results in a higher quality recovery, less attenuated, S-wave (Figure B-1 h). Relaxation after a high confining pressure phase (Sage II-B to II-C) in 40% THF hydrate-bearing clean sand samples show no loss in amplitude nor change in first wave arrival cycle in the P-waveform (Figure B-2 c to e). This emphasizes the effect of clay-hydrate interaction at lower hydrate saturations (40%) on the attenuation in these samples.

The results, discussed in this section, show the dependence of attenuation of low hydrate-bearing sediments on pressure conditions. When interpreting field data, it is important to keep this in mind, as not knowing the pressure conditions of your area of interest could lead to an over- or underestimation of hydrate saturation in the sediment. In addition, these results emphasize the strong effects of clay content on attenuation. Sediments found in nature never consist of 100% pure quartz grains but always contain contaminants, potentially in the form of clay. Therefore, it is important to know the clay content in order to make accurate predictions on hydrate saturation in sediments.

Samples containing 30 wt% clay and 70 wt% Ottawa Sand F110

Raw Data - Compressional Wave



Raw Data - Shear Wave

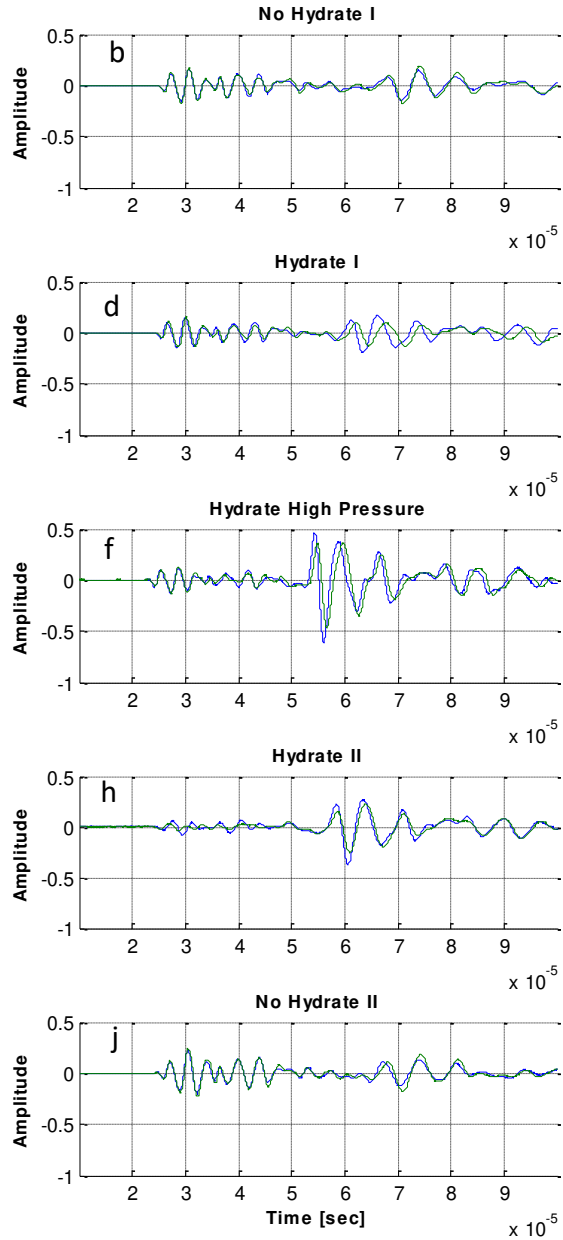


Figure B-1 Collected and overlaid waveforms for two separate samples with 70 wt% Ottawa Sand and 30 wt% clay. a & b – fluid saturated samples at 535 psi, c & d – samples containing 40% hydrate at 535 psi, e & f – samples containing 40% hydrate at elevated pressure (2275 psi), g & h – samples containing 40% hydrate after reducing pressures back to 535 psi, i & j – samples after hydrate dissociation at 535 psi

Samples containing clean Ottawa Sand F110

Samples containing 30 wt% clay and 70 wt% Ottawa Sand F110

Raw Data - Compressional Wave

Raw Data - Compressional Wave

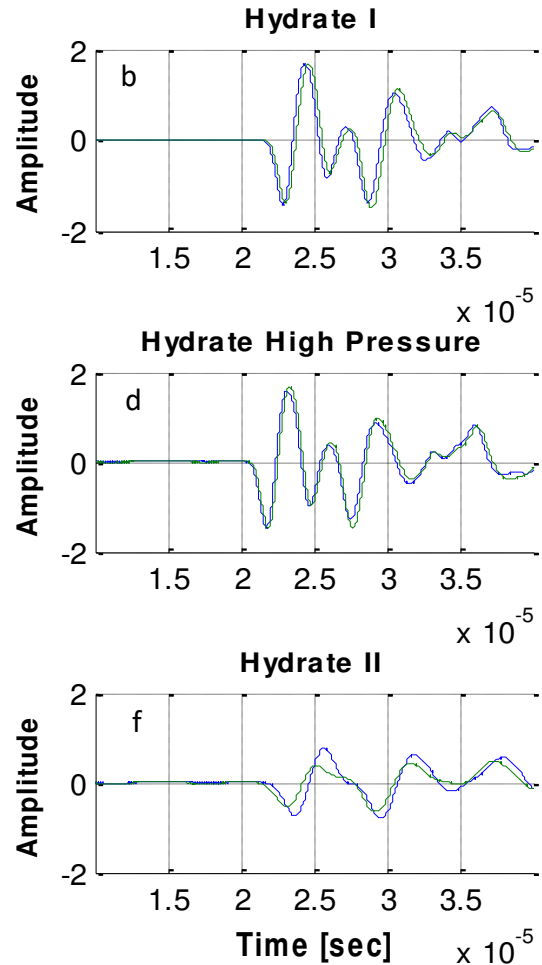
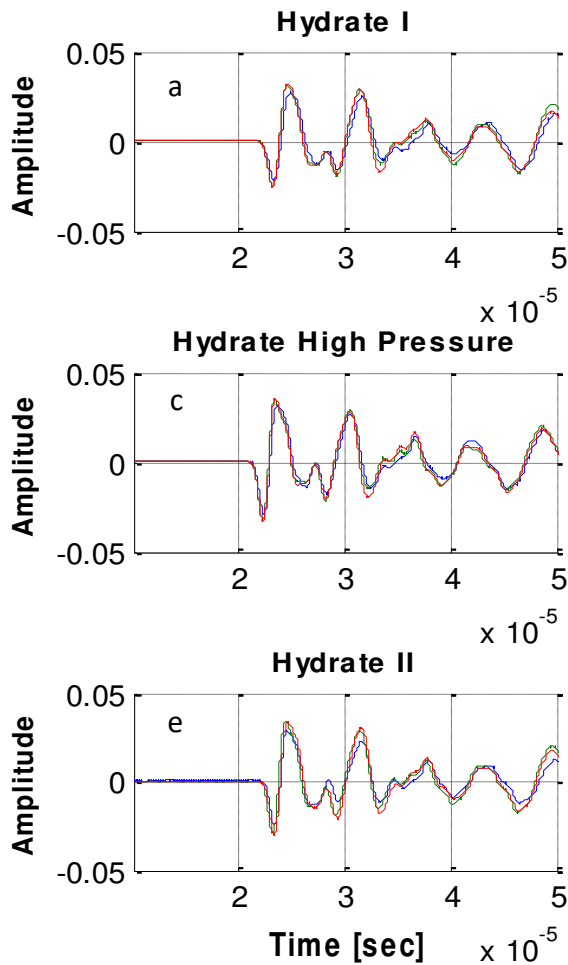


Figure B-2 Comparison for ultrasonic raw p-waveforms for clean sand (a,c,e) and sand with 30 wt% clay (b,d,f) containing 40% THF hydrate saturation. a, c, and e contain three raw waveforms each (blue, green, red). b, d, and f contain two waveforms each (blue and green). Clean sand samples with 40% THF hydrate saturation do not show a visible change in their waveforms after elevated pressures (comparing a and e), whereas samples with 30 wt% clay show a visible decrease in amplitude after elevated confining pressures (comparing b and f)

CHAPTER 4

DETECTING CEMENTATION AND POROSITY LOSS FROM A LOSS-DIAGRAM

To be submitted to: *Science*

Mathias Pohl^{*a}, Manika Prasad^a

4.1 Abstract

A comparison with laboratory data obtained using methane as a hydrate former verifies that acoustic properties of THF hydrate-bearing sediments are comparable to the methane hydrate-bearing sediments found in nature, demonstrating that THF is an appropriate proxy for methane hydrates. Loss mechanisms for low hydrate saturation (0 and 40%) are independent of pressure, whereas higher hydrate saturations (60%) are affected by an increase in pressure.

4.2 Introduction

In Chapter 3, I showed how compressional and shear wave velocities and attenuations (Q^{-1} or its inverse Q) change with formation of hydrates in the pore space. I now compare these changes in a joint diagram to investigate their predictive properties. Winkler and Nur (1992) have shown that a plot of Q_p/Q_s versus V_p/V_s can be used to distinguish between dry, partially saturated, and fully saturated sandstones where Q_p/Q_s is more sensitive to presence of gas than the V_p-V_s ratio. Prasad and Meissner (1992) extended on the work done by Winkler and Nur (1982) using unconsolidated sand in the dry and saturated stage. Since the hydrate-bearing sedi-

*Primary author and editor.

Corresponding author. Direct correspondence to mpohl@mines.edu.

^aDepartment of Geophysics, Colorado School of Mines, Golden, CO 80401, USA

ments used in this study span from unconsolidated to hydrate-cemented with varying saturations, this so-called loss diagram might allow us to differentiate hydrate saturations. In the following, I present the methodology of creating a loss-diagram and present the data from Chapter 3 together with literature data on sandstones and loose sands.

4.3 Methodology

Loss-Diagram

Winkler and Nur, 1982 and Prasad and Meissner (1992) used the compressional and shear wave velocity equations as well as the quality factor ratio for compressional and shear components in an isotropic:

$$\left(\frac{V_p}{V_s}\right)^2 = \frac{K + \frac{4}{3}\mu}{\mu} \quad (4-1)$$

$$\frac{Q_p}{Q_s} = \frac{K + \frac{4}{3}\mu}{\mu} \cdot \frac{\mu_i}{K_i + \frac{4}{3}\mu_i}, \text{ with } Q_s = \frac{\mu}{\mu_i} \text{ and } Q_p = \frac{K + \frac{4}{3}\mu}{K_i + \frac{4}{3}\mu_i} \quad (4-2)$$

Combined, these two equations become:

$$\frac{Q_p}{Q_s} = \frac{\mu_i}{K_i + \frac{4}{3}\mu_i} \cdot \left(\frac{V_p}{V_s}\right)^2 \quad (4-3)$$

where $\mu_i / (K_i + \frac{4}{3}\mu_i)$ is the ratio between shear (μ_i) and the bulk (K_i) losses. Note: higher order terms are ignored in the complex number computation. A plot of equation (4-3) is called the loss-diagram and helps determining whether shear or bulk losses dominate in acoustic wave propagation through the sample. It has been shown that bulk losses dominate in unconsolidated and fully water-saturated sediments whereas the $K_i - \mu_i$ ratio decreases for dry unconsolidated

sediments (Prasad and Meissner, 1992). In this work, we investigate how loss mechanisms change after hydrate formation. Knowing these changes helps to make better predictions regarding hydrate saturations. We use the loss-diagram to determine the effects of hydrate saturation and pressure in the various sand samples.

4.4 Results

A comparison of data obtained from Chapter 3 with previous studies is shown in a loss-diagram (Figure 4-1, close up Figure 4-2). Data from Prasad and Meissner (1992) representing unconsolidated, dry and clean sands (yellow triangles) show low Q_p-Q_s and low $(V_p/V_s)^2$, and in the saturated stage (yellow circles), the data lie between $K_i = 15\mu_i$ and $K_i = 20\mu_i$.

The mechanical properties depend on the hydrate formation process (dissolved or free gas). The losses for grain cementing hydrates (black squares; Priest et al., 2006) for low hydrate saturation (<3%) plot in the same area as Prasad and Meissner (1992) data for the fully water saturated samples, whereas the losses for higher (3-35%) saturated samples plot in the same area as Prasad and Meissner (1992) data for the dry samples. Priest et al. (2009) studied at methane hydrates formed out of solution which resulted in methane hydrate formation in the pore space. In the loss-diagram, these data (red squares) plots in the same area as the fully water saturated sand samples from Prasad and Meissner (1992) for low (<20%) methane hydrate saturation. Samples with higher (39%) methane hydrate saturation plot in a lower $K_i-\mu_i$ ratio zone together with field data (Guerin & Goldberg, 2002; green triangles). The initially high Q_p-Q_s ratio (~ 2.3) decreases with increasing hydrate saturation. The $(V_p/V_s)^2$ remains low (<7) with increasing hydrate saturation.

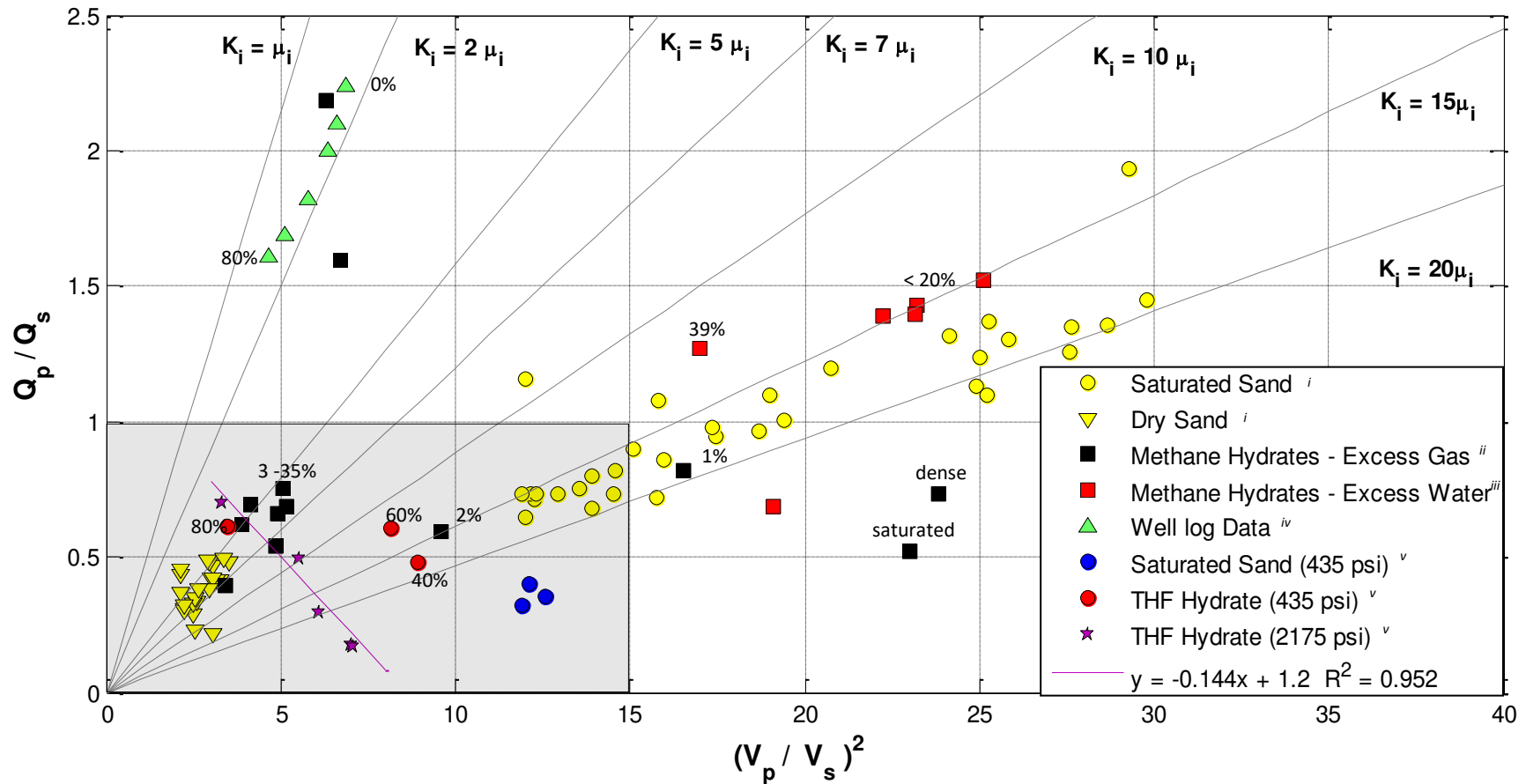


Figure 4-1 Comparisons of loss mechanisms in sands with varying hydrate concentrations. Modeled ratios of shear (μ_i) to bulk (K_i) losses are shown by solid gray lines, while symbols depict data. The saturated sands show high bulk losses ($K_i=15-20 \mu_i$). Hydrate presence changes and increases shear losses proportionally to hydrate saturation. Percentages indicate hydrate saturation. Sources: i: Prasad and Meissner (1992), ii: Priest et al., 2006, iii: Priest et al., 2009, iv: Guerin and Goldberg (2002), v: this study. The gray shaded box indicates the zoomed in part shown in Figure 4-2.

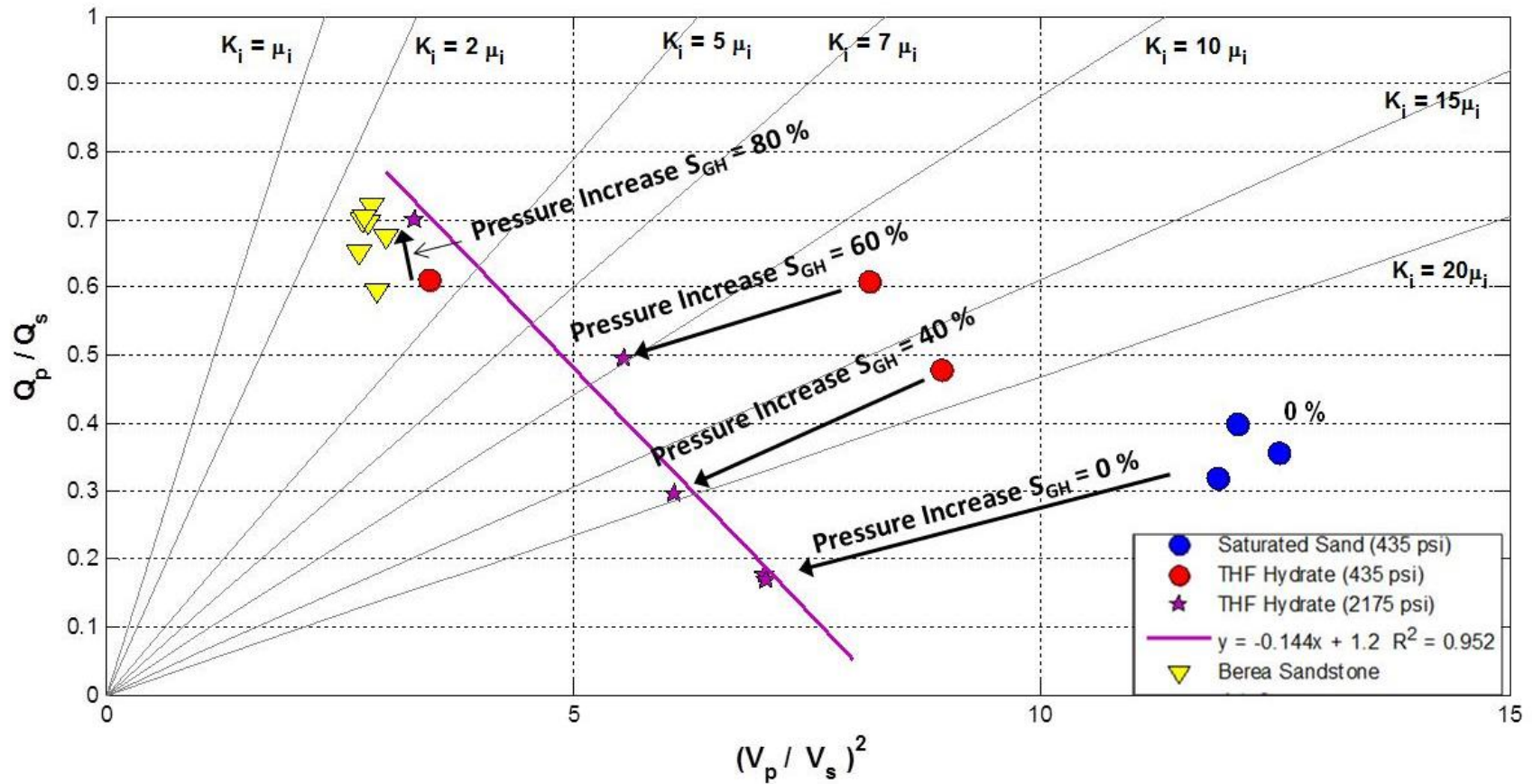


Figure 4-2 Loss Diagram with THF-water mixture samples (grey box from Figure 4-1): Before THF hydrate formation (blue circles), THF hydrate-bearing sands at 535 psi (red circles) and 2275 psi (purple stars) confining pressure. The purple line is a linear regression for the purple stars. Grey lines show the relationship between K_i and μ_i . Yellow triangles are fully water saturated Berea Sandstone data (Mapeli, 2018).

Ultrasonic velocity and attenuation data obtained from the clean sand samples from Chapter 3 are plotted on the same loss-diagram (Figure 4-1, close up Figure 4-2). Before hydrate formation, all samples have high $(V_p/V_s)^2$ of ~ 12 and a Qp-Qs ratio between 0.3-0.4. With increasing hydrate saturation, the $(V_p/V_s)^2$ starts to decrease, and Qp-Qs ratios increase, resulting in lower $K_i\text{-}\mu_i$ ratio zones. An increase in pressure (from 535 to 2275 psi) causes a decrease in squared Vp-Vs and Qp-Qs ratios for all but the 80% THF hydrate saturated sample, this sample shows an increase in Qp-Qs ratio and a minimal decrease in squared Vp-Vs ratio. At elevated pressures, the samples (hydrate and non-hydrate-bearing) follow a linear trend (purple line). Fully water saturated, non-hydrate-bearing, Berea sandstone data (Mapeli, 2018; yellow triangles) plot in the same $K_i\text{-}\mu_i$ ratio zone and follow the same behavior with elevated pressures as the 80% THF hydrate-bearing clean sand samples.

4.5 Discussion

We combined data of clean sand from this work with data from previous studies in a loss-diagram (Figure 4-1). With increasing pressure, unconsolidated, fully water saturated sands (yellow circles, Prasad and Meissner (1992)), show a decrease in Vp-Vs and Qp-Qs ratios while remaining within the same loss zone (between $K_i = 15 \mu_i$ and $K_i = 20\mu_i$). This implies that the ratio between the loss mechanisms (K_i and μ_i) does not change with increasing pressure.

The elastic properties of the sediment depend on where the hydrate formation occurs (pore space or along the grains). Low amounts of methane hydrates formed on the grain surfaces (black squares, Priest et al., 2006) have low $(V_p/V_s)^2$ and Qp-Qs ratios, most probably due to the cementing effect of the hydrate stiffening the sediment. When methane hydrates form in the pore space, a larger hydrate saturation is required to cause similar stiffening effects. We see this in a

decrease in the $(V_p/V_s)^2$ and Q_p-Q_s ratios with increasing hydrate saturation ($> 20\%$; red squares, Priest et al., 2009). Additionally, once hydrate saturation in the sample reaches load-bearing levels, the loss ratio ($K_i - \mu_i$) begins to shift to lower ratios.

The velocity and quality factor results of the clean sand samples with varying hydrate saturation plot within the shaded area in Figure 4-1. A close up exclusively containing clean sand data obtained in this study is shown in Figure 4-2. With increasing THF hydrate saturation, the $K_i - \mu_i$ ratio decreases, implying that hydrates add to the rigidity of the samples. This behavior is also observed for methane hydrates formed in the pore space (Priest et al., 2009), indicating that THF hydrates are an appropriate substitution for methane hydrates in their effect on mechanical properties of hydrate-bearing samples. Effects of confining pressure on the seismic properties depend on THF hydrate content. Lower THF hydrate samples (0 and 40%) follow the same behavior as unconsolidated and fully water-saturated sand samples (Prasad and Meissner, 1992). At 60% THF hydrate saturation, the behavior with increasing confining pressure starts to deviate from the lower THF hydrate saturated samples by decreasing the $K_i - \mu_i$ ratio.

The V_p-V_s ratio for the 60% THF hydrate-bearing clean sand samples is lower than the ratio for 40% THF hydrate-bearing clean sand samples, indicating more consolidation at higher hydrate saturations. The Q_p-Q_s ratio for the 60% THF hydrate-bearing clean sand samples decreased less than the ratio does for the 40% THF hydrate-bearing clean sand samples. This is due to a greater increase of Q_s in the lower saturated sample. The effect of increasing confining pressure on the 80% THF hydrate saturated clean sand samples varies greatly from the lower THF hydrate saturated samples; the Q_p-Q_s ratio increases, mimicking the behavior under pressure of consolidated sandstone (Toksöz et al., 1979). This is also seen in an analysis of the behavior of the consolidated and fully water saturated Berea sandstone (Figure 4-2, yellow triangles; Mapeli,

2018). This indicates that continuously increasing the THF hydrate content (to ~ 80%) of a clean sand sample will result in consolidating behavior similar to that of consolidated and fully saturated sandstones.

The THF hydrate saturated clean sand sample behavior under pressure might be used to analyze the bottom simulating reflector (BSR). The BSR is a reflector that marks the bottom of hydrate stability zone and is characterized by a phase inversion relative to the seafloor reflection event and it crosscuts the local seismic stratigraphy (Berndt et al., 2004). It also follows a constant pressure profile (Figure 4-2, purple line). Using our findings, one might be able to make better predictions about hydrate saturation based on Q_p - Q_s changes as well as V_p - V_s along the BSR.

Well log data are plotted in a low K_i - μ_i ratio zone with high Q_p - Q_s ratios that decrease with increasing hydrate saturation (Figure 4-1, green triangles; Guerin and Goldberg, 2002). Comparing this well log data to lab data from Winkler and Nur (1982) the Q_p - Q_s and squared V_p - V_s ratios are similar to partially saturated sandstones. This could indicate that during well-logging, free gas was present within the hydrate stability zone, either due to hydrate dissociating during the drilling process itself or in situ gas. Therefore, the loss mechanism in hydrate-bearing sediments could be misinterpreted due to alterations (i.e., dissociation of hydrates caused by depressurization during the drilling process).

4.6 Conclusion

We have shown how a loss-diagram can be used to separate hydrates in the pore space from hydrates as a cement within sediments. We find that:

- THF-hydrates can be used as proxy for methane hydrates – Methane hydrate-bearing sediments show the same change in K_i - μ_i ratio as THF hydrate-bearing sediments.

- Seismic loss mechanisms for fluid-saturated unconsolidated clean sands are independent of pressure changes but sensitive to hydrate saturation.
- At low (0 and 40%) hydrate saturations, the bulk to shear loss is much larger and it does not change with pressure. At higher hydrate saturation (60 and 80%) the bulk to shear loss is lower and reduces further with elevated pressures.
- We derive an empirical equation, $Q_p/Q_s = -0.144(V_p/V_s)^2 + 1.2$, to predict hydrate saturation along a Bottom Simulating Reflector (BSR) which is considered to be at equal pressure.

Our analysis can be used to assess hydrate saturation and presence of gas. For example, we show how well log data from hydrate-bearing sediments in the Mallik 2L-38 research well are not comparable with dry or fully saturated sands or sandstone data, but rather with partially saturated sandstone.

4.7 Acknowledgement

This material is based upon work supported by the U.S. Department of Energy, Office of Science, Office of Fossil Energy, under Award Number DE-FE 0009963.

4.8 References

- Guerin, G., and Goldberg, D., (2002). Sonic waveform attenuation in gas hydrate-bearing sediments from the Mallik 2L-38 research well, MacKenzie Delta, Canada. *J. Geophys. Res.*, 107:2088. doi:10.1029/2001JB000556
- Mapeli, C (2018), The Effect of Pressure on Simultaneous Elastic and Electrical Measurements, MS Thesis, Colorado School of Mines, Golden, Colorado
- Prasad, M. and R. Meissner, (1992), Attenuation mechanisms in sands: Laboratory versus theoretical Biot data, *Geophysics* 57, 710–719

Priest, J. A.; Best A. I.; Clayton, C. R. I., (2006), Attenuation of seismic waves in methane gas hydrate-bearing sand *Geophys. J. Int.*, 164 (1)149– 159

Priest, J.A., E.V.L. Rees, and C.R.I. Clayton (2009), “Influence of gas hydrate morphology on the seismic velocities of sands”, *Journal of Geophysical Research*, 114, B1120

Winkler, K. W., and Nur, 1982, Seismic attenuation: Effects of pore fluids and frictional sliding: *Geophysics*, 47, no. 1, 1-15.

CHAPTER 5

EFFECT OF METHANE HYDRATE FORMATION ON COMPLEX CONDUCTIVITY MEASUREMENTS IN SANDSTONE

To be submitted to: *Journal of Geophysical Research*

Mathias Pohl^{*a}, Cesar Mapeli^a, Manika Prasad^a

5.1 Abstract

Gas Hydrates are considered either as an energy resource, as receptors for CO₂ storage, or as aggravating climate change processes. Gas production by dissociating gas hydrate has the potential to damage or even collapse otherwise stable sedimentary layers. Therefore, we need to develop indicators of processes during hydrate production. In this research, we investigate changes in the electrical properties of sediments as potential indicators of the formation or dissociation of hydrates. We present continuous complex conductivity measurements during hydrate formation and dissociation in a sandstone. We find that hydrate formation increases conductivity due to exothermic reactions. Finally, cooling below the freezing point of water results in a sudden decay in conductivity. This sudden drop in conductivity indicates ice formation from unreacted free water present between the thin layer of hydrate and sediment grains. Hydrate dissociation leads to a drop in conductivity due to endothermic reactions. These detectable conductivity changes accompanying hydrate formation and dissociation allow us to understand the fundamental processes associated with hydrate dissociation and formation.

*Primary author and editor.

Corresponding author. Direct correspondence to mpohl@mines.edu.

^aDepartment of Geophysics, Colorado School of Mines, Golden, CO 80401, USA

5.2 Introduction

Natural gas hydrates are crystalline structures consisting of water molecules that encage guest molecules with small molecular diameters, most commonly methane and occasionally larger molecules such as ethane, propane, and carbon dioxide (Sloan & Koh, 2007). Low temperatures, elevated pressures, adequate amounts of free water as well as gas (either in free- or in dissolved-phase) are required for hydrates to occur in nature. These conditions exist in marine environments, along continental slopes, or in permafrost regions (Kvenvolden & Lorenson, 2001).

Hydrate-bearing sediments can be considered as a potential hydrocarbon resource, contributor to climate change, or as a storage opportunity for CO₂ (e.g., Kvenvolden, 1999; Collett, 2002; Ruppel, 2007; Priest et al., 2009; Maslin et al., 2010; Boswell & Collett, 2011; Seol & Lee, 2013). Thus, there is a need for reliable detection and quantification of gas hydrates in the subsurface.

In the presence of gas hydrates, the mechanical properties of sediments change. The effects of hydrates on the mechanical stiffness of sediments depends on the hydrate saturation and hydrate location – along the grains or in pore space. Hydrates forming along the grains cause a stiffening of the sediment at low hydrate saturation (~5% S_{gh}), whereas hydrates forming in the pore space only affect the grain matrix after they reach a critical hydrate saturation of about 30-40% (Rydzy, 2014). Gas hydrate deposits are generally identified through seismic surveys and well-logging. In seismic surveys, the bottom simulating reflector (BSR) can indicate the presence but not the amount of hydrate that is stored in the zone (Hyndman & Spence, 1992; Bünz et al., 2003). Additional geophysical techniques are needed to help quantify the amount of hydrate stored in the subsurface.

In addition to seismic properties, gas hydrates also influence the electrical properties of sediments. Pure methane hydrates are considered to be insulators (Edwards, 1997, Du Frane et al, 2011 & 2015). The formation of gas hydrates replaces the conductive pore fluid, thereby restricting the flow of electric current which results in an increase in bulk resistivity of the sediment (Yuan & Edwards, 2000). The formation of hydrate withdraws fresh water from the formation and excludes ions. Thus, hydrate formation causes a competing effect between water saturation decrease and salinity increase. Additionally, hydrate formation causes a drop in permeability and reduces potential conductivity pathways. Kerkar et al. (2014) found that methane gas dissolved in water forms gas hydrates in the pore-space and away from the grains. Electrical measurements detect the combined effects of free water surrounding the hydrate, as well as unreacted water within the hydrate structure in hydrate-bearing systems, without being able to distinguish between the two.

Controlled source electromagnetic (CSEM) surveys in conjunction with seismic surveys can provide a more detailed picture of the near surface that potentially hosts gas hydrates. Higher velocities and lower conductivities in the presence of hydrates might be due to free gas, which causes the velocity to drop and the conductivity to remain low; this combined method can be used to distinguish between areas containing hydrates versus areas with free gas. Field CSEM studies have demonstrated the sensitivity of this method in assessing general gas hydrate concentration, saturation, and distribution patterns (Schwalenberg et al., 2005, 2017; Evans, 2007; Weitemeyer et al., 2006, 2011).

Methane hydrates form in an exothermic reaction (Linga et al., 2007) which uses pore fluids and gas present in the sediment. This depletion in pore fluid causes a pressure decrease and the exclusion of salt (in the form of ions) (Ussler & Paull, 1995). Laboratory studies have shown

that the bulk conductivity decreases with increasing hydrate saturation (Spangenberg & Kulenkampff, 2006; Ren et al., 2010; Li et al., 2012; Du Frane et al., 2015). Mixing sand grains with methane hydrates results in an increased conductivity compared to pure methane hydrates (Du Frane et al., 2015). Previous studies lack the time-limited, dynamic process of hydrate formation and dissociation. A thorough understanding of the geophysical indicators during the dynamic processes of hydrate formation and dissociation could lead to better detection using remote sensing or other techniques. And, this understanding would help avoid complications such as sediment collapse during hydrate dissociation, or unwanted CO₂ hydrate formation near an injection well.

We present here continuous measurements of complex conductivity during methane hydrate formation and dissociation in a sandstone. After hydrate formation, we freeze the sample to convert any un-reacted water in the sample to ice. Lastly, we increase the temperature above hydrate stability and record the changes in conductivity due to hydrate dissociation. By measuring real and imaginary conductivity values, we investigate the effects of hydrates on electrical properties. While the real part of complex conductivity allows us to quantify gas hydrate saturation, the imaginary or quadrature component gives information about pore structure (Slater and Lesmes, 2002, Revil et al., 2014, Niu et al., 2016).

Our results document the water depletion process which takes place during hydrate formation as well as the pore fluid dilution process during dissociation. Such time-sensitive changes during hydrate formation and dissociation can be used to monitor the formation and dissociation front in natural hydrate deposits when subject to rapid changes (e.g. gas production).

5.3 Background – Low-Frequency Complex Conductivity Principles

The electrical resistivity (ρ) and its inverse, electrical conductivity (σ), describe electrical charge transport (Guéguen & Palciauskas, 1994). Resistivity and conductivity are both intrinsic properties, independent of sample geometry. The resistance (R) or conductance (C) data acquired in the laboratory are related to conductivity or resistivity by:

$$R = \rho G \quad (5-1)$$

$$C = \frac{\sigma}{G} \quad (5-2)$$

where G is the geometric factor and is dependant on the experimental design. We used a finite element code (Niu et al., 2016) in COMSOL-Multiphysics to calculate the geometric factor for our setup.

Conductivity measurements are normally used to determine the water saturation of clean sandstones using the empirical Archie's law (Archie, 1942):

$$S_w^n = F \frac{R_w}{R_t} = F \frac{\sigma}{\sigma_w} \quad (5-3)$$

$$F = \frac{a}{\phi^m} \quad (5-4)$$

where S_w is the water saturation, n is the saturation exponent, F is the formation factor, R_w is the real resistivity of formation water, R_t is the real resistivity of the formation, σ is the real bulk conductivity, σ_w is the real conductivity of water, a is the tortuosity factor, ϕ is the porosity and, m is the cementation factor. The so-called Archie's parameters are frequently assigned constant values, where $a=1$; $m=n=2$.

Since the conduction in sediments is ionic, rather than electronic as in metal, the effective conductivity of a porous media is a result of a combination of the conductivity difference between

the solid particles, in this case silica ($\sigma \sim 10^{-12}$ S/m), and a high conductivity brine solution ($\sigma \sim 0.1$ S/m). Due to the contrast between these two conductivities, the electrical current applied flows mainly through the fluid connected pore space. However, current flow is not the only phenomena observed; polarization also contributes to the electrical resistivity (Vinegar and Waxman, 1984, Slater and Lesmes, 2002). The phenomena of an electrical double layer (or Helmholtz layer) (Schwarz, 1962, Schurr, 1964, Revil, 2012) around silica grains has been used to explain the polarization effects observed in rocks. The electrical double layer consists of a so-called Stern layer which is comprised of positively charged ions which adhere to the negatively charged grain surfaces (Revil, 2012).

We performed conductivity measurements at the low-frequency range (1.5 Hz to 12 kHz), also known as the Induced Polarization (IP) method, Complex Resistivity (CR) method, or Complex Conductivity (CC) method, using four electrodes. IP is sensitive to the ability of the porous material to store electrical charges as well as conduct electrical charge. Mathematically, this behavior can be represented by the combination of real and imaginary conductivity (Vinegar and Waxman, 1984, Slater and Lesmes, 2002, Revil and Skold, 2011):

$$\sigma^* = \sigma' + i\sigma'' \quad (5-5)$$

$$|\sigma^*| = \sqrt{\sigma'^2 + \sigma''^2} \quad (5-6)$$

$$\tan \varphi = \frac{\sigma''}{\sigma'} \quad (5-7)$$

where σ' is the real part of conductivity (also known as in-phase conductivity), σ'' is the imaginary part (out-of-phase or quadrature conductivity), φ is the phase angle, and $i = \sqrt{-1}$.

The measured in-phase conductivity is the combined effect from the electrical current influenced by pore bulk water conductivity and surface conductivity (Revil et al., 2013a,

Revil et al., 2013b). The out-of-phase conductivity is exclusively affected by surface polarization, and can therefore provide information relating to pore structure. Both conductivities (in-phase and quadrature) help us characterize changes within the sample during hydrate formation and dissociation. In this paper, conductivity and quadrature conductivity refer to the real, in-phase and complex part of the conductivity measurement, respectively.

5.4 Experimental Setup and Procedure

We conducted continuous electrical measurements before, during, and after hydrate formation in a Castlegate sandstone sample. Castlegate sandstone is a clean sandstone composed of 70% quartz, 30% feldspar, and lithic fragments with a 25% porosity (Pradhan et. al., 2014). The sandstone was used as received and therefore contained small amounts (100 ppm) of precipitated sodium, determined from Inductively Coupled Plasma Mass Spectrometry (ICP-MS) measurements.

Sample Preparation:

The sample was cut into a cylindrical form of one-inch diameter and two-inch length. Silver epoxy was applied to the top and bottom of the sample to serve as a current source. Two small holes were drilled into the side of the sample (3.5 mm deep and 1.5 mm diameter). Electrodes (3mm x 2 mm) are glued using silver epoxy into those holes to measure the electrical potential caused by the current electrodes. These potential electrodes are non-polarizable and made of silver silver-chloride (Ag-AgCl; Figure 5-1 a). The dry weight of the instrumented sample was measured after vacuum drying for four days at 80°C.

The oven-dried sample was placed into a desiccator and maintained at about 100% humidity. The moisture content in the sample was monitored by measuring the relative weight gain

of the sample. To guarantee maximum saturation, the sample was kept for three months in the desiccator. Note: the greatest weight increase occurred during the first two weeks (1.55 g), for the remainder of the three months the weight increased marginally to a final weight increase of 1.586 g. The humidity exposure resulted in a water saturation (S_w) of about 24.6% as estimated by the relative weight gain. Using the measured salt content from ICP-MS and the achieved water saturation, we calculated the salinity to be 63,000 ppm corresponding to a water conductivity (σ_w) of 7.58 S/m at 20°C. The water salinity was confirmed using the resistivity chart for a NaCl-water solution (from Schlumberger) which indicates a salinity between 60,000 and 70,000 ppm at the beginning of the experiment ($S_w=25\%$ and $T=20^\circ\text{C}$).

Measurement Procedure:

The partially water-saturated sample was placed into a pressure vessel that allowed us to measure electrical conductivity and temperature under pressure as follows. The sample was first pressurized with methane gas to 1500 psi (10.34 MPa) using an ISCO-pump (Model 1000 HL). Once the pressure inside the vessel stabilized, the pressure vessel was submerged in a cooling bath to control the temperature (Figure 5-1 b). Continuous complex conductivity data were collected during the temperature cycles at intervals of every two minutes at frequencies between 1.5 Hz to 12 kHz for 11 days. Three cycles of cooling – freezing – thawing – warming were collected in the following discrete steps to assess repeatability:

1. Initialize experiment by stabilizing the temperature in the vessel to 20°C.
2. Form hydrates by reducing the temperature in the vessel to 4.5°C..... I Cooling Stage
3. Freeze remaining water by reducing the temperature in the vessel..... II Freezing Stage to -8.5°C

- 4 Thaw ice by increasing the temperature in the vessel to 4.5°C..... III Thawing Stage
- 5 Dissociate hydrates by increasing the temperature IV Warming Stage

We established the completion of the reaction at each step from conductivity measurements. Conductivity values changed during each reaction. The reaction was considered as completed once the conductivity values remained constant for at least 5 hours.

In the following, we describe and discuss the results of the continuous complex conductivity measurements during the Cooling, Freezing, Thawing, and Warming Stages in the context of hydrate formation processes and infer locations of the hydrates in the sediment matrix.

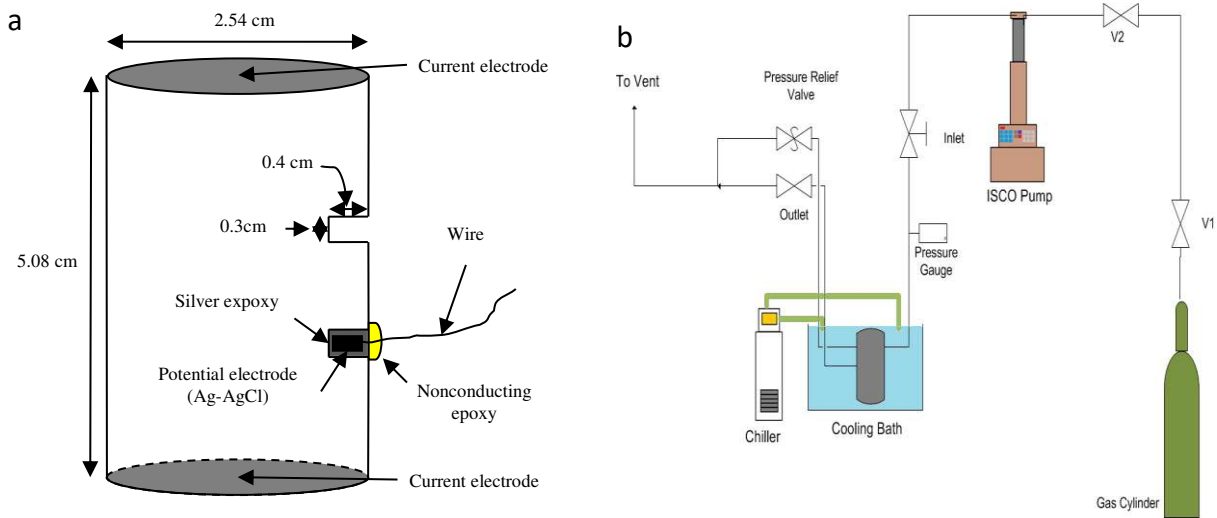


Figure 5-1 (a) Schematic of the sandstone sample with current electrodes on the top and the bottom and potential electrodes in the middle of the sample. (b) Schematic of the experimental setup (courtesy of Ahmad Majid).

5.5 Results

Since the measured conductivity for three cycles of hydrate-ice formation (Figure 5-2a) shows repeatability over a frequency range from 1.5–12 kHz, we only use cycle I data at 94 Hz to

discuss the changes in conductivity and temperature during each event (Figure 5-3). The arrows in Figure 5-2 a and 5-3 b point to distinct and repeated events during the experiment.

The Cooling Stage (Arrow I) marks the onset of hydrate formation with an exponential drop in conductivity. The Freezing Stage (Arrow II) marks the onset of ice formation accompanied by a sharp drop in conductivity. As ice is thawed (Thawing Stage: Arrow III), conductivity increases back to Cooling Stage levels for sediment plus hydrate. And finally, during hydrate dissociation (Warming Stage: Arrow IV), the real part of conductivity reaches initial values. Although the real and the imaginary parts of the conductivity track each other, they differ during hydrate dissociation (Warming Stage: Arrow IV). The real conductivity shows an increase, whereas the onset of hydrate dissociation leads to a prominent peak that drops back to the initial values before the start of the cycle. In the following section, we will use the experimental data collected at 94 Hz as a representative frequency.

Cooling Stage

Figure 5-3 c shows the conductivity values during the Cooling Stage from 20°C to 4.5°C. Real conductivity decreases with decreasing temperature. A linear fit shows conductivity decreasing at a rate of 0.1737 S/m/°C for the first 45 min (marked by an arrow in Figure 5-3c). During the same period of time, the quadrature conductivity remained constant at a value of 0.001337 S/m. After 45 min, an increase in both conductivity and quadrature conductivity can be observed which lasted for about 9 min, followed by a steeper decrease in conductivity values until the temperature reached a constant value of 4.5°C. Note that the pressure inside the vessel dropped from 1500 psi to about 1376 psi during the cooling process. Figure 5-4 a shows the temperature and pressure schematics for the comparative conductivity values at two different frequencies

during Stage I (Figure 5-4 b). The observed peak in complex conductivity values is frequency dependent with larger values at higher frequencies.

Freezing Stage

To convert any unreacted water still present in the sample the temperature was reduced to approximately -8.5°C (Note that the freezing point of water at 1450 psi is -0.75°C), accompanied by a pressure decrease from 1376 to 1276 psi. Figure 5-3 d shows the changes in conductivity during the freezing process. Electrical conductivity decreases as temperature decreases. At the 26 h mark (marked by an arrow in Figure 5-3 d), a sharp decrease can be noted in both conductivity and quadrature conductivity values. Note that the complex conductivity values during the freezing process do not show frequency dependence.

Thawing Stage

Although conductivity values remain constant after the 40 h mark (Figure 5-3 b), the quadrature conductivity values continue to increase (Figure 5-3 b). When the temperature was increased back to 4.5°C to melt the ice, the conductivity values increased correspondingly to values comparable to the end of the Cooling Stage. Note that quadrature conductivity was higher at the end of Stage III compared to the end of Stage I. Also, the pressure values increased back to 1376 psi as before the Freezing Stage.

Warming Stage

Figure 5-3 f shows that conductivity changes during hydrate dissociation. Both conductivity and quadrature conductivity increase with increasing temperature. The quadrature conductivity reaches a high point at around 71.36, h whereas the conductivity reaches its high point at the 72.24 h mark to a maximum high point (marked by an arrow in Figure 5-3 f). Both

conductivities decrease after they reached a high point. However, the conductivity starts to increase again at the 74 h mark. At the same time, the quadrature conductivity increases for about 2 h and then starts to decrease again. The observed bump during the Warming Stage is more prominent at higher frequencies in the conductivity values, whereas frequency does not have a significant effect on the amplitude in the quadrature conductivity (Figure 5-4). However, as it can be seen in Figure 5-6 b, at the 71.5 h mark the quadrature conductivity exhibits elevated values at 190 Hz.

5.6 Discussion

Cooling Stage

In general, electrical conductivity in sediments decreases with decreasing temperature (Sanyal, 1972, Ucok et al., 1980), as was also observed at the beginning of the cooling procedure in our experiment (Figure 5-3 c). The rate of change of the conductivity with temperature was calculated at $0.1737 \text{ S/m/}^\circ\text{C}$ (eqs 5-3 and 5-4).

The initial increase in conductivity accompanying the onset of hydrate formation is counter-intuitive because hydrates are considered insulators (Edwards, 1997) (Figure 5-3 c). We consider four phenomena that might explain the increase in conductivity:

- (a) Decrease in water saturation as water is used for the formation of hydrates
- (b) Increase in salinity as some of the water forms hydrates
- (c) Diffusion of ions to equilibrate the salinity imbalance due to hydrate formation occurring from the outside of the sample towards the inside.
- (d) Temperature increase due to the exothermic hydrate formation.

In the following, we model each of these phenomena to assess their contributions on the observed conductivity.

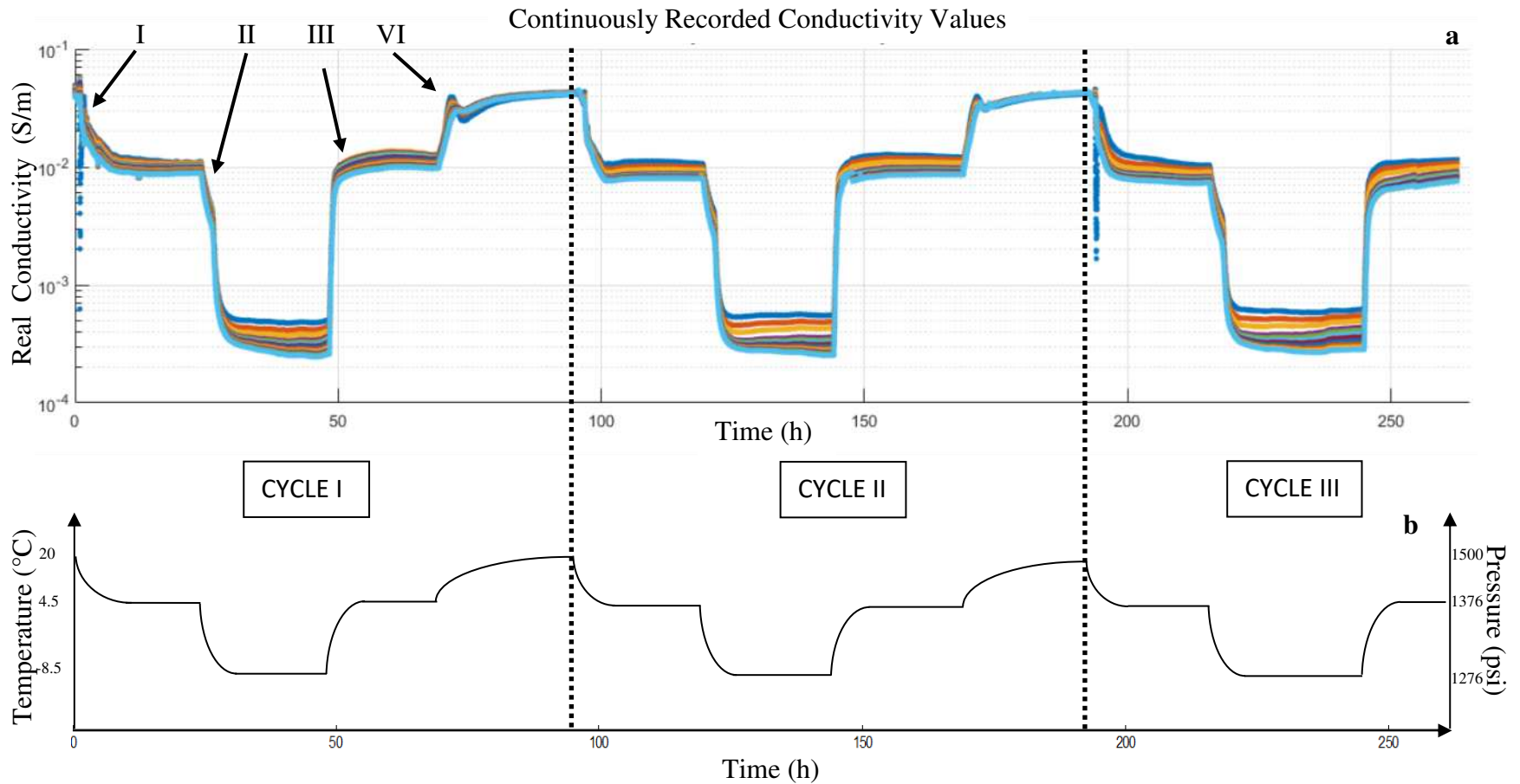


Figure 5-2 (a) Overview of the measured electrical conductivities for the entire duration of the test. Letters are used in the following figures and displayed here to mark when changes occurred. I marks the event of hydrate formation, II marks the freezing of the hydrate-bearing sample, III marks the thawing of the ice in the ice-hydrate-bearing sample, and IV marks the hydrate dissociation event. Different colors denote different frequencies. The data displayed ranges from 1.5 Hz–12000 Hz. (b) Schematic of temperature and pressure changes during the duration of the experiment.

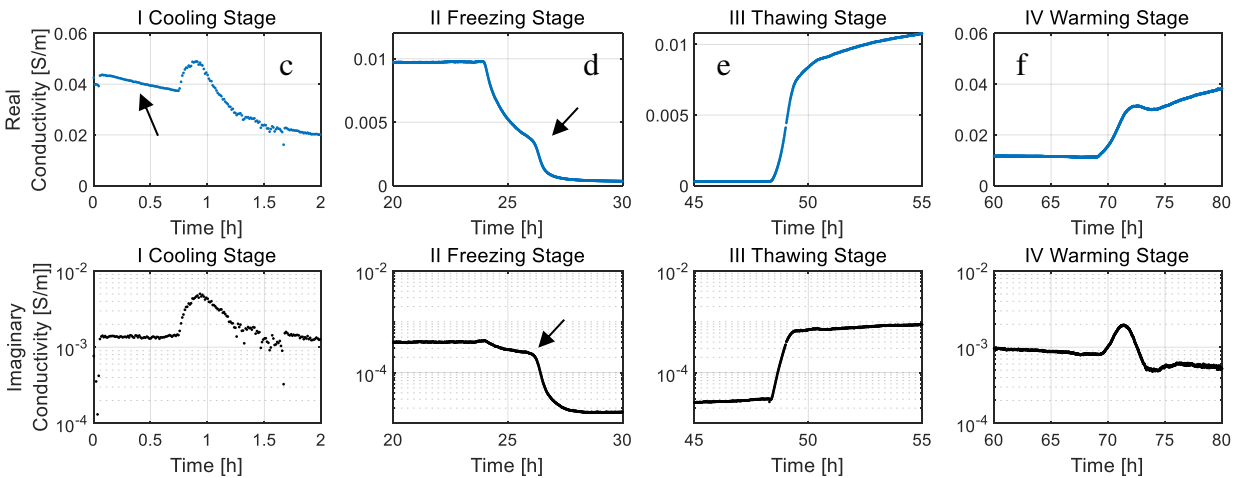
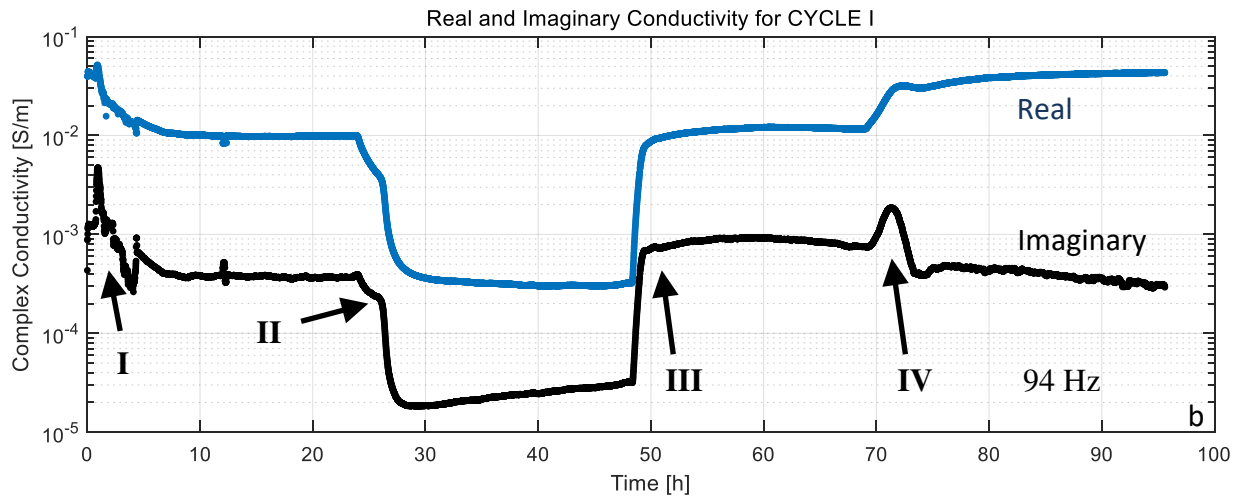
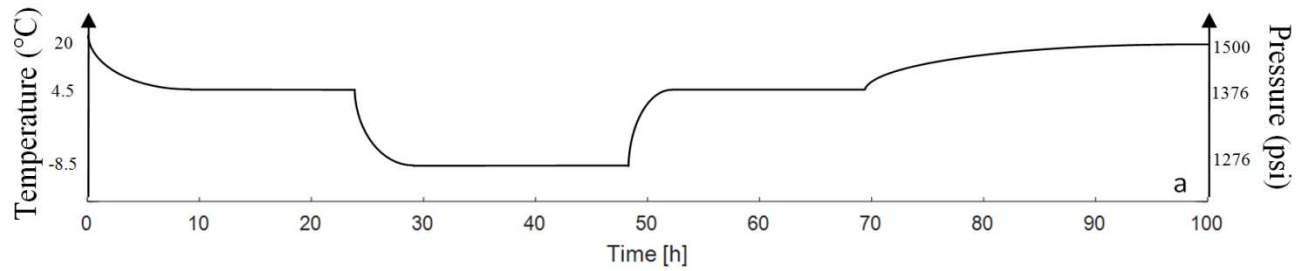


Figure 5-3 (a) Schematic of temperature and pressure changes during Cycle I. (b) Real (blue) and Imaginary (black) part of the conductivity measurements for the first complete measurement cycle, displayed for a single frequency (94 Hz). The arrows mark distinct stages: Arrow I – Cooling Stage with the onset of hydrate formation, Arrow II – Freezing Stage with ice formation, Arrow III – Thawing Stage, Arrow IV – Warming Stage with the onset of hydrate dissociation. Zoomed in plots for I Cooling Stage (c), II Freezing Stage (d), III Thawing Stage (e), and IV Warming Stage for Real (blue) and Imaginary (black) conductivity at 94Hz.

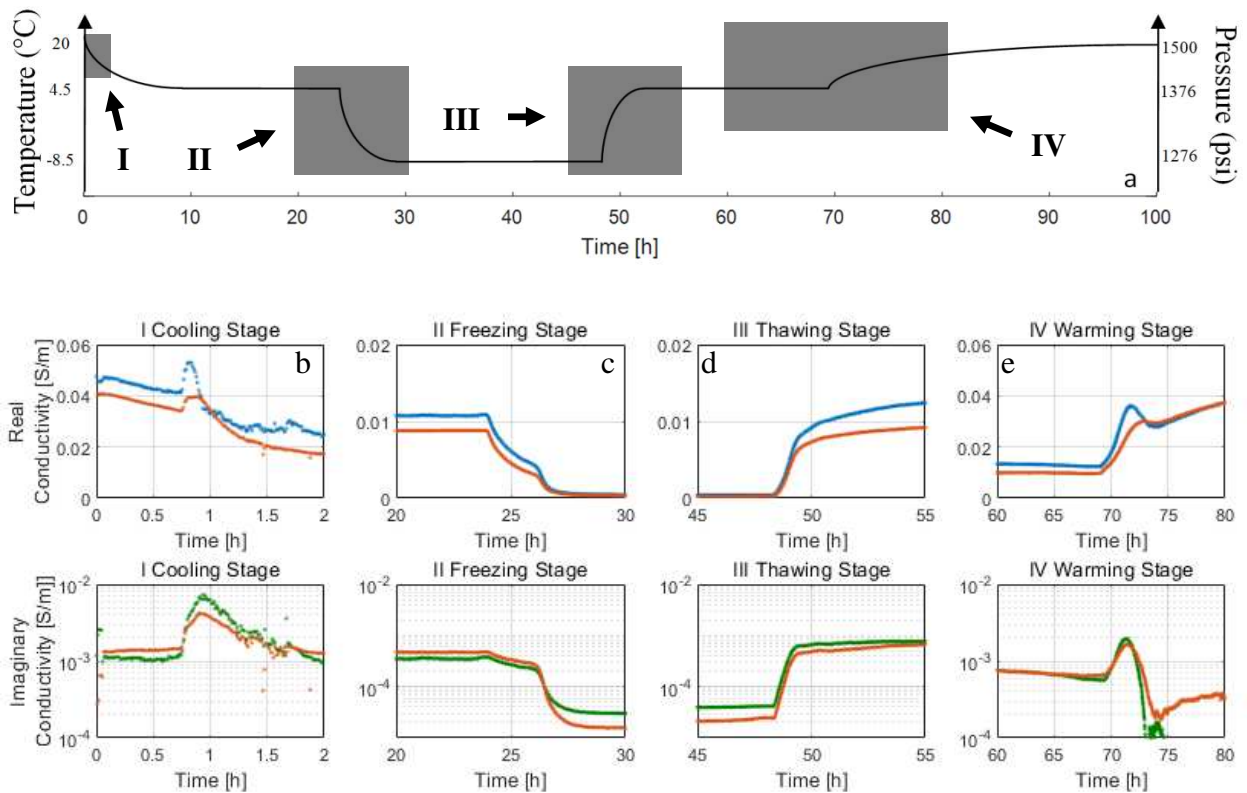


Figure 5-4 (a) Schematic of temperature and pressure changes during Cycle I. Grey boxes and arrows point at the four stages that are displayed in b, c, d, and e. A comparison between higher (6000 Hz for real conductivity (blue), 375 Hz for imaginary conductivity (green)), and lower (1.5 Hz for both real and imaginary conductivity (brown)) frequencies is displayed for (b) I Cooling Stage, (c) II Freezing Stage, (d) III Thawing Stage, and (e) IV Warming Stage.

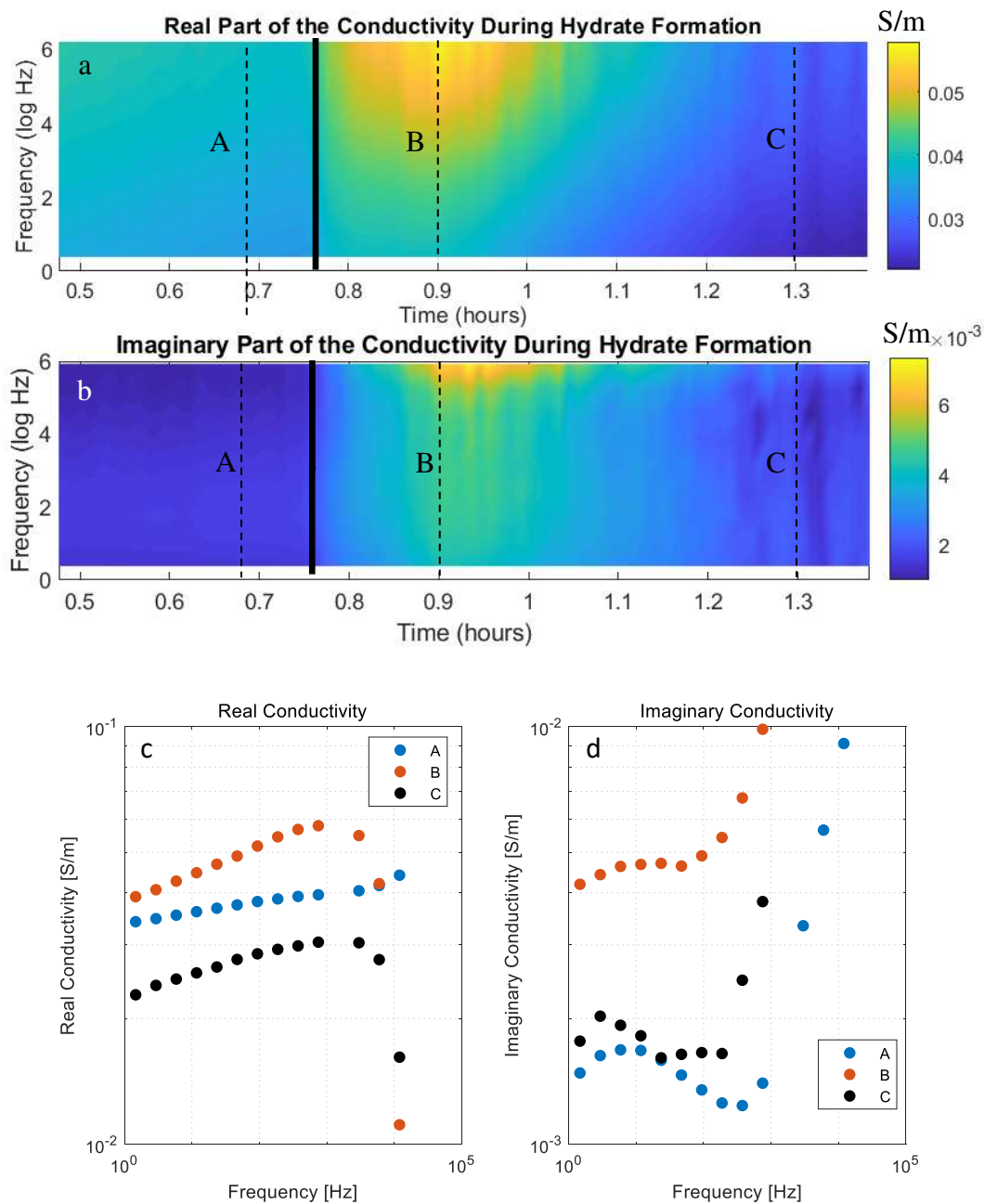


Figure 5-5 (a) Real part of the conductivity over time and frequency for the initial hydrate formation. The amplitude in the electrical conductivity is frequency dependent during hydrate formation, and the formation process can be detected for up to 30 min for higher frequencies. Lower frequencies stop seeing hydrate formation after 15 min. (b) Imaginary part of the conductivity over time and the frequency for the initial hydrate formation. Conductivity values drop quickly once hydrate formation starts. The solid black line marks the onset of hydrate formation. Dotted lines and letters correspond to data plotted in (c) and (d). (c) and (d) show conductivity and quadrature conductivity values, respectively, over a range of frequencies before, during, and after hydrate formation.

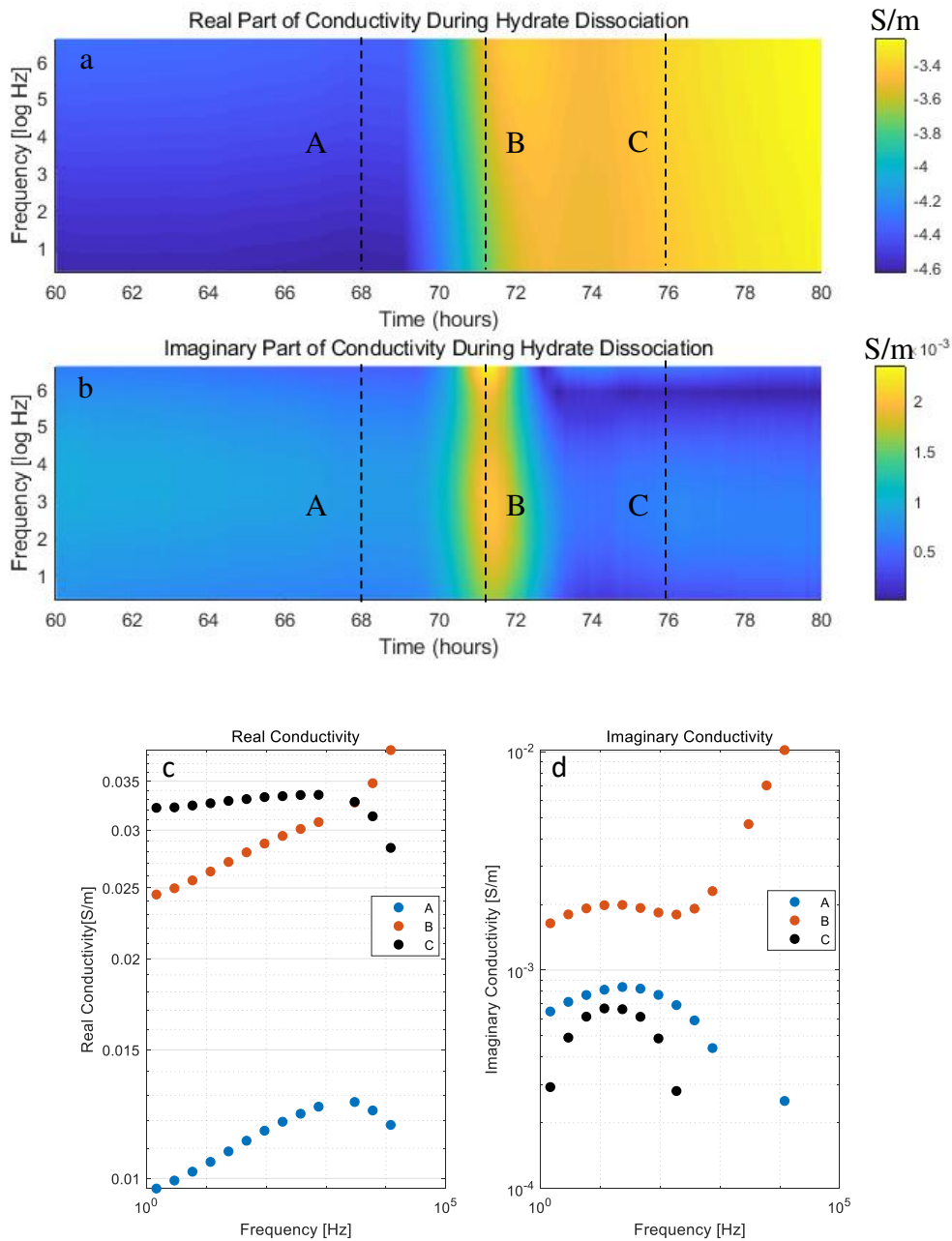


Figure 5-6 Real part (a) and Imaginary part (b) of the conductivity over time and frequency for the IV Warming Stage (hydrate dissociation). The amplitude in electrical conductivity is frequency dependent during hydrate dissociation, and the dissociation process can be detected for up to 170 min. (c) and (d) show conductivity and quadrature conductivity values, respectively, over a range of frequencies before, during, and after hydrate dissociation (A, B, and C correspond to A, B, and C in (a) and (b)). A peak in the imaginary conductivity (d) at 23 Hz can be observed during hydrate dissociation (B)

Hydrate formation is accompanied by an increase in salinity and a decrease in water saturation (Ussler & Paull, 1995). The process of hydrate formation extracts fresh water from the available pore water for inclusion in the hydrate lattice, thereby decreasing the water saturation and the resulting conductivity. The exclusion of ions causes an increase in the salinity of the residual fluid resulting in an increase in conductivity. Using equations 5-3 & 5-4 and assuming 50% reduction in water saturation due to hydrate formation, we anticipate the following:

- Water saturation reduces from 25 to 12.5%
- Salinity increases from 63,000 to 126,000 ppm
- Corresponding to an increase in salinity, water conductivity increases from 6.25 to 12.5 S/m (Schlumberger, 2009)
- Corresponding to a decrease in water saturation, conductivity decreases by a factor of 4

The combined effect of decreased water saturation and increased salinity would overall decrease the conductivity by a factor of 2. Because we observe an increase in conductivity, these competing events alone cannot explain the observed increase in conductivity during the hydrate formation process.

As the cooling of the sample is not uniform, regions exist within the sample that have not yet reached hydrate stability conditions. As a result, the excluded ions diffuse to areas outside the hydrate stability zones, reducing the local salinity until a balance is reached. The rate of diffusion is given by:

$$t \approx \frac{x^2}{2D} \tag{5-8}$$

where x is the distance of diffusion (cm) and D is the diffusion coefficient, 1.33 E-5 cm²/s for sodium (Robinson & Stokes, 1959). It would take a sodium molecule 25 min to travel 2 mm. As

the increase in conductivity happens in 9 min the diffusion process is too slow to cause any significant changes to the measured conductivity.

Hydrate formation is an exothermic event at which energy, in the form of heat, is released. Let's assume we are at the half way point between the onset of hydrate formation and the stabilization point at 4.5°C. At the stabilization point the pressure and temperature are 1376 psi and 4.5°C, respectively, yielding a water saturation of 18% calculated using the Soave-Redlich-Kwong equation (A. Majid personal communication). Therefore, at the half way point between 25 and 18% the water saturation is 21.5%. At this point, the water conductivity is 11.27 S/m (eqs 5-3 and 5-4). We can use this water conductivity value, together with the calculated water conductivity value (7.59 S/m) and known temperature at the start of the experiment to calculate the temperature at the half way point, using:

$$\frac{1}{\sigma_2} = \frac{1}{\sigma_1} \cdot \frac{T_1 + 21.5}{T_2 + 21.5} \quad (5-9)$$

where σ_1 and T_1 , and σ_2 and T_2 are the conductivity (S/m) and temperature (°C) values at the start of the experiment and the onset of hydrate formation, respectively. We find that the temperature at the halfway point has increased significantly to 38.6°C. While this value is heavily dependent on frequency, it is clear that hydrate formation is associated with a significant increase in temperature, which could explain the observed increase in conductivity. Therefore, the bump in conductivity is caused by the exothermic reaction of hydrate formation.

We can calculate the pressure and temperature conditions at the onset of hydrate formation. We find that the onset of hydrate formation starts at 13.1°C (eq. 5-9), corresponding to a calculated pressure of 1450 psi. This is considered the boundary of hydrate stability conditions. The initial increase in conductivity during hydrate formation should be observed in the field and can be used to determine the location of the hydrate formation front.

The increase and subsequent decrease in conductivity values after hydrate formation are observed at all frequencies (Figure 5-5 a). However, the amplitude of this phenomenon is frequency dependent: the higher the frequency, the greater the measured conductivity values. As the low-frequency conductivity values start to decrease, the higher frequencies continue to observe greater conductivity values.

The imaginary part of the conductivity is sensitive to changes along the grains. Figure 5-5 b shows that with the onset of hydrate formation, the imaginary conductivity values increase for 11 min before the values start to decrease, whereas the real part of the conductivity showed changes for up to 30 min. This implies that changes along the grains are resolved more quickly than the bulk changes. Since the changes are due to hydrate formation, and this is known to happen along the outer layers of the water, one would have expected the reverse. However, it is conceivable that once the bulk of the water has been converted into hydrates, there are still layers of water covering the grain surfaces. The imaginary conductivity is now measuring along the surface of the hydrate. However, the small pockets of water below the hydrate are undetected by the imaginary conductivity, yet they are still included in the real part of the conductivity. Micro CT-imaging can give further insight into this problem, but this is beyond the scope of this paper.

Freezing Stage

Between the hours of 20 to 24 the conductivity is constant at a temperature of 4.5°C (Figure 5-3 c), which indicates that hydrate formation has finished. At the 24 h mark, we reduce the temperature to -8.5°C and we see an immediate decrease in conductivity, consistent with previous observations during the cooling phase. During this phase, it is plausible that additional hydrate is forming that could not form at the previous phase because the increase in salinity might have shifted the hydrate stability conditions to lower temperature conditions. But, further hydrate

formation effects are below the resolution capabilities of the electrical measurements, as temperature dependent changes in conductivity might overlay this effect.

At approximately the 26 h mark we can see a sudden decrease in conductivity values. In our closed system, there are only four components: hydrates, mineral grains, gas, and water. Hydrates, mineral grains, and gas would not show abrupt changes in conductivity with decreasing the temperature below 0°C. Water, however, could respond with a sudden change in conductivity when converted into ice. Therefore, the most likely explanation for this sudden decrease in conductivity is that an additional conversion of free water within the sample occurred, whether into ice or additional hydrate. With the presence of hydrates, these free water pockets between the hydrate crystals significantly increase the acoustic wave attenuation properties of hydrate-bearing sediments (Pohl et al., 2017).

Warming Stage

As the sample is brought back to room temperature, there is a steep increase (0.0055 S/m/h) in conductivity (Figure 5-3 d) followed by a slight decrease and a subsequent increase at a reduced rate (0.001 S/m/h). This is the reverse of the same process that we observed during hydrate formation, implying that the hydrate dissociation front can be detected by the same means as discussed in the hydrate formation section.

Assuming that water saturation, at the point where the conductivity continuously increases after the conductivity dip, is equal to that of the water saturation before hydrate formation, we can calculate the change of water conductivity with temperature. We find that this value is equal to 0.3806 S/m/°C, which is approximately double that of the change of water conductivity observed during this phase of the cooling process. This disparity in values could mean that either our assumption of water saturation is incorrect, or that the assumption that the temperature at the

starting point is not 14°C or it could mean that the water conductivity changes more rapidly during the thawing process than it does during the cooling process. If our assumption of an equal water saturation is incorrect, it cannot lead to the significant disparity in the calculated values. If we assume that the change of water conductivity with temperature should be the same in the thawing process (0.1737 S/m/°C), we calculate that the temperature at the starting point should be 6.8°C. At this temperature, hydrates are stable, therefore this cannot explain this disparity. This indicates that the change of water conductivity with temperature must be greater in the thawing process than it was in the cooling process. The endothermic behavior during hydrate dissociation removes heat from the system, inhibiting the warming of the system, retarding the hydrate dissociation process. As our electrodes are on the edges of the sample, remnant hydrate dissociation from the center of the sample could affect the electrical conductivity measurements. Again, as shown in the hydrate formation process, the dilution of the fresh water released from the hydrate dissociation would have a lesser effect on conductivity than the increase in water saturation. However, the effect on conductivity is dominated by the endothermic reaction of hydrate dissociation.

5.7 Conclusions

The beginning of hydrate formation is marked by an increase in conductivity. This increase is the result of a combination of factors such as increased salinity, decreased water saturation, diffusion of ions, and the exothermic reaction of hydrate formation where the latter is the most dominant effect. This increase in conductivity is observed at all frequencies, though the amplitude is greater at higher frequencies, and can be used in the field to monitor the hydrate formation front during CO₂ sequestration. Therefore, we recommend field data be obtained at the highest possible frequency. As the hydrate dissociation is the reverse effect and is as detectable, this method can

also be used to determine the hydrate dissociation front in field data during gas production out of hydrate deposits.

Temperature reduction to below the freezing point of water results in a sudden drop in conductivity values. This indicates that layers of water between the hydrates and sediment grains were still present in the sample. The presence of these free water pockets between the hydrate crystals, explains the increase in acoustic wave attenuation properties of hydrate-bearing sediments.

This work has shown that electrical conductivity measurements can help us detect both hydrate formation and hydrate dissociation fronts. Our results show how the dynamic processes of hydrate formation and dissociation can be captured using complex conductivity. These insights are useful during monitoring gas production from hydrates.

5.8 Acknowledgement

This material is based upon work supported by the U.S. Department of Energy, Office of Science, Office of Fossil Energy, under Award Number DE-FE 0009963.

5.9 References

- Archie, G. E. (1942), The electrical resistivity log as an aid in determining some reservoir characteristics. *Trans. Am. Inst. Min. Metall. Pet. Eng.*, 146, 54–62.
- Berndt, C., Bünz, S., Clayton, T., Mienert, J., & Saunders, M. (2004), Seismic character of bottom simulating reflectors: Examples from the mid-Norwegian margin. *Mar. Pet. Geol.*, 21(6), 723–733, doi:10.1016/j.marpetgeo.2004.02.003.
- Boswell, R., & Collett, T. (2011), Current perspectives on gas hydrate resources. *Energy Environ. Sci.*, 4, 1206–1215.
- Bünz, S., Mienert, J., & Berndt, C., (2003), Geological controls on the Storegga gas-hydrate system of the mid-Norwegian continental margin. *Earth and Planetary Science Letters*, 209(3–4), 291–307.

- Chave, A.D., (2009), On the electromagnetic fields produced by marine frequency domain controlled sources. *Geophys. J. Int.*, doi:10.1111/j.1365-246X.2009.04367.x
- Collett, T. (2002), Energy resource potential of natural gas hydrate. *Am. Assoc. Pet. Geol. Bull.*, 86, 1971–1992
- Du Frane, W. L., Stern, L. A., Weitemeyer, K. A., Constable, S., Pinkston, J., Roberts, J. J., (2011), Electrical properties of polycrystalline methane hydrate. *Geophys. Res. Lett.*, 38, L09313,
- Du Frane, W. L., Stern, L. A., Constable, S., Weitemeyer, K. A., Smith, M. M., & Roberts, J. J. (2015), Electrical properties of methane hydrate + sediment mixtures. *J. Geophys. Res. Solid Earth*, 120, 4773–4783, doi:10.1002/2015JB011940.
- Edwards, R. N., (1997), On the resource evaluation of marine gas hydrate deposits using seafloor transient electric dipole-dipole methods. *Geophysics*, 62, 63–74.
- Guéguen, Y. & Palciauskas, V (1994), Introduction to the physics of rocks, Princeton University Press, Princeton, N.J.
- Evans, R. L. (2007); Using CSEM techniques to map the shallow section of seafloor: From the coastline to the edges of the continental slope. *Geophysics*; 72 (2): WA105–WA116. doi: <https://doi.org/10.1190/1.2434798>
- Hyndman, R.D., Foucher, J.P., Yamamoto, M., Fisher, A., & Shipboard Scientific Party of Ocean Drilling Program Leg 131, (1992), Deep sea bottom-simulating-reflectors: Calibration of the base of the hydrate stability field as used for heat flow estimates. *Earth and Planetary Science Letters*, v. 109, p. 289-301.
- Hyndman, R. D., & Spence, G. D., (1992), A seismic study of methane hydrate marine bottom simulating reflectors. *Journal of Geophysical Research – Solid Earth*, 97, 6683–6698.
- Kerkar, P. B., Horvat, K., Jones, K. W., & Mahajan, D. (2014), Imaging methane hydrates growth dynamics in porous media using synchrotron X-ray computed microtomography, *Geochem. Geophys. Geosyst.*, 15, 4759–4768, doi: 10.1002/2014GC005373.
- Kvenvolden, K., & Lorenson, T. (2001), The global occurrence of natural gas hydrate, in Natural Gas Hydrates: Occurrence, Distribution, and Detection. *Geophys. Monogr. Ser.*, vol. 124, edited by C. Paull and W. Dillon, pp. 87–98.
- Kvenvolden, K. A. (1999), Potential effects of gas hydrate on human welfare. *Proc. Natl. Acad. Sci. U.S.A.*, 96(7), 3420–3426.

- Li, F. G., Sun, C. Y., Li, S. L., Chen, G. J., Guo, X. Q., Yang, L. Y., et al. (2012), Experimental studies on the evolution of electrical resistivity during methane hydrate formation in sediments. *Energy Fuels*, 26, 6210–6217, DOI: 10.1021/ef301257z
- Linga, P., Kumar, R., Englezos, P. (2007) Gas hydrate formation from hydrogen/carbon dioxide and nitrogen/carbon dioxide gas mixtures. *Chemical Engineering Science*, 62, 16, 4268-4276, doi.org/10.1016/j.ces.2007.04.033.
- Maslin, M., Owen, M., Betts, R., Day, S., Jones, T.D., & Ridgwell, A. (2010), Gas hydrates: Past and future geohazard? *Proc. R. Soc. A*, 368(1919), 2369–2393.
- Niu, Q., Prasad, M., Revil, A., and Saidian, M., (2016), Textural control on the quadrature conductivity of porous media: *Geophysics*, 81, E297–E309, <https://doi.org/10.1190/geo2015-0715.1>.
- Pohl, M., Prasad, M. & Batzle, M. L. (2017), Ultrasonic attenuation of pure THF hydrates. *Geophysical Prospecting*, doi: 10.1111/1365-2478.12534
- Pradhan, S., Stroisz, A.M., Fjaer, E., Stenebraten, J., Lund, H.K., Sonstebo, E.F., & Roy, S. (2014), Fracturing tests on reservoir rocks: Analysis of AE events and radial strain evolution. *ARMA* 14-7442
- Priest, J.A., Rees, E.V.L., & Clayton, C.R.I. (2009), Influence of gas hydrate morphology on the seismic velocities of sands. *Journal of Geophysical Research*, 114, B1120
- Ren, S. R., Liu, Y., & Zhang, W. (2010), Acoustic velocity and electrical resistance of hydrate bearing sediments. *J. Petrol. Sci. Eng.*, 70, 52–56
- Revil, A., Florsch, N., Camerlynck, C., (2014), Spectral induced polarization porosimetry, *Geophysical Journal International*, Volume 198, Issue 2, Pages 1016–1033, <https://doi.org/10.1093/gji/ggu180>
- Revil, A., Woodruff, W. F., Torres-Verdín, C. et al. (2013a). Complex conductivity tensor of anisotropic hydrocarbon-bearing shales and mudrocks. *Geophysics* 78 (6): D403-D418. <https://doi.org/10.1190/geo2013-0100.1>.
- Revil, A., Eppheimer, J. D., Skold, M. et al. (2013b). Low-frequency complex conductivity of sandy and clayey materials. *Journal of Colloid and Interface Science* 398: 193-209. <https://doi.org/10.1016/j.jcis.2013.01.015>.
- Revil, A., (2012), Spectral induced polarization of shaly sands: Influence of the electrical double layer. *Water Resources Research*, 48, W02517, doi: 10.1029/2011WR011260.

- Revil, A. Skold, M. (2011), Salinity dependence of spectral induced polarization in sands and sandstones, *Geophysical Journal International*, Volume 187, Issue 2, 1 November 2011, Pages 813–824, <https://doi.org/10.1111/j.1365-246X.2011.05181.x>
- Robinson, R.A. & Stokes, R.H., (1959), *Electrolyte solutions*, Butterworths Scientific Publications
- Ruppel, C. (2007), Tapping methane hydrates for unconventional natural gas, *Elements*, 3(3), 193–199
- Sanyal, S. K., (1972), *The Effect of Temperature on Electrical Resistivity and Capillary Pressure Behavior of Porous Media*. Ph.D. Dissertation, Stanford University,
- Schlumberger, (2009), *Schlumberger log interpretation charts*, Schlumberger, Gen-6, page 8
- Schurr, J. M. (1964). On the theory of the dielectric dispersion of spherical colloidal particles in electrolyte solution. *The Journal of Physical Chemistry* 68 (9): 2407-2413.
- Schwalenberg, K., Willoughby, E. C., Mir, R., & Edwards, R. N. (2005), Marine gas hydrate electromagnetic signatures in Cascadia and their correlation with seismic blank zones. *First Break*, 23, 57–63.
- Schwalenberg, K., Rippe, D., Koch, S., & Scholl, C. (2017), Marine-controlled source electromagnetic study of methane seeps and gas hydrates at Opouawe Bank, Hikurangi Margin, NewZealand. *J. Geophys. Res. Solid Earth*, 122, 3334–3350, doi:10.1002/2016JB013702.
- Schwarz, Gerhard. (1962). A theory of the low-frequency dielectric dispersion of colloidal particles in electrolyte solution1, 2. *The Journal of Physical Chemistry* 66 (12): 2636-2642.
- Seol J, & Lee, H. (2013), Natural gas hydrate as a potential energy resource: From occurrence to production. *Korean J Chem Eng*, 30 (2013), pp. 771-786
- Slater, L. and Lesmes, D. P. (2002), Electrical - hydraulic relationships observed for unconsolidated sediments. *Water Resources Research*, 38, no. 10: 33–46. <https://doi.org/10.1029/2001WR001075>.
- Sloan, E., & Koh, C. (2007), *Clathrate Hydrates of Natural Gases*. Boca Raton, FL: CRC Press
- Spangenberg, E., & Kulenkampff, J. (2006), Influence of methane hydrate content on electrical sediment properties. *Geophys. Res. Lett.*, 33, L24315, doi: 10.1029/2006GL028188.
- Ucok, H., Ershaghi, I., Olhoeft, G. R., & Hand, L. L. (1980), Resistivity of Brine Saturated Rock Samples at Elevated Temperatures, Presented at the 1980 Stanford Geothermal Workshop

- Ussler, W. & Paull, C.K. (1995). Effects of ion exclusion and isotopic fractionation on pore water geochemistry during gas hydrate formation and decomposition. *Geo-Marine Letters* 15: 37. doi.org/10.1007/BF01204496
- Vinegar, H. J. and Waxman, M. H. 1984. Induced polarization of shaly sands. *Geophysics* 49 (8): 1267- 1287. <https://doi.org/10.1190/1.1441755>.
- Weitemeyer, K. A., Constable, S. C., Key, K. W., & Behrens, J. P. (2006), First results from a marine controlled-source electromagnetic survey to detect gas hydrates offshore Oregon. *Geophys. Res. Lett.*, 33, L03304, doi:10.1029/2005GL024896
- Weitemeyer, K. A., Constable, S., & Tréhu, A. M. (2011), A marine electromagnetic survey to detect gas hydrate at Hydrate Ridge, Oregon. *Geophys. J. Int.*, doi:10.1111/j.1365-246X.2011.05105.x
- Yuan, J., & Edwards, R. N. (2000), The assessment of marine gas hydrates through electrical remote sounding: Hydrate without a BSR? *Geophys. Res. Lett.*, 27, 2397– 2400, doi:10.1029/2000GL011585.

CHAPTER 6

CONCLUSIONS

The main objective of this thesis was to provide an understanding of how the physical properties (velocity, attenuation, and complex conductivity) change with the formation of hydrates in sediments. The experimental data allow us to explore connections between changes in rock physics parameters and hydrate saturation. Understanding these changes is crucial for characterizing and monitoring gas hydrate formation and dissociation in the subsurface. In the following, I provide a summary of the conclusions for each chapter:

Ultrasonic Attenuation of Pure THF Hydrates (Chapter 2)

We have shown that THF-water mixture, THF hydrate with residual water, and THF hydrate with frozen residual water are distinguishable by their ultrasonic velocity and attenuation as well as NMR signatures. We conclude that pure, solid THF hydrate phase has negligible attenuation, while elevated attenuation is found in the presence of liquid water. A combination of NMR and ultrasonic measurements allows us to characterize gas hydrate formation as well as dissociation processes.

Investigating the Influence of Clay Content on Ultrasonic Velocities and Attenuation of THF Hydrate-Bearing Sediment (Chapter 3)

Our results for hydrate-bearing clean Ottawa Sand F110 are comparable with literature data. We find that:

- Hydrate formation in any sediment (clean sand, sand-clay) causes an increase in P- and S-wave velocities.

- The pressure dependence of velocities decreases with increasing hydrate saturation and clay content.
- At high hydrate saturation (80%), V_p - V_s ratio mimics cemented sandstones, independent of clay content.
- Hydrate formation in clean sand causes a decrease in Q_p and Q_s
- Q_s is strongly pressure dependent; this pressure dependence is inversely proportional to hydrate saturation. Changes in Q_p are small and less conclusive.

Our results of the effects of clay content and pressure on hydrate-bearing sediments show that a lack of knowledge about the pressure conditions could lead to errors in estimates of hydrate saturation when interpreting field data.

Detecting Cementation and Porosity Loss from a Loss-Diagram (Chapter 4)

We have shown how a loss-diagram can be used to separate hydrates in the pore space from hydrates as a cement within sediments. We find that:

- THF-hydrates can be used as proxy for methane hydrates – Methane hydrate-bearing sediments show the same change in $K_i - \mu_i$ ratio as THF hydrate-bearing sediments.
- Seismic loss mechanisms for fluid-saturated unconsolidated clean sands are independent of pressure changes but sensitive to hydrate saturation.
- At low (0 and 40%) hydrate saturations, the bulk to shear loss is much larger and it does not change with pressure. At higher hydrate saturation (60 and 80%) the bulk to shear loss is lower and reduces further with elevated pressures.
- We derive an empirical equation, $Q_p/Q_s = -0.144(V_p/V_s)^2 + 1.2$, to predict hydrate saturation along a Bottom Simulating Reflector (BSR) which is considered to be at equal pressure.

Our analysis can be used to assess hydrate saturation and presence of gas. For example, we show how well log data from hydrate-bearing sediments in the Mallik well are not comparable with dry or fully saturated sands or sandstone data, but rather with partially saturated sandstone.

Effect of Methane Hydrate Formation on Complex Conductivity Measurements in Sandstone (Chapter 5)

The beginning of hydrate formation is marked by an increase in conductivity. This increase is the result of a combination of factors such as increased salinity, decreased water saturation, diffusion of ions, and the exothermic reaction of hydrate formation where the latter is the most dominant effect. This increase in conductivity is observed at all frequencies, though the amplitude is greater at higher frequencies, and can be used in the field to monitor the hydrate formation front during CO₂ sequestration. Therefore, we recommend field data be obtained at the highest possible frequency. As the hydrate dissociation is the reverse effect and is as detectable, this method can also be used to determine the hydrate dissociation front in field data during gas production out of hydrate deposits.

Temperature reduction to below the freezing point of water results in a sudden drop in conductivity values. This indicates that layers of water between the hydrates and sediment grains were still present in the sample. The presence of these free water pockets between the hydrate crystals, explains the increase in acoustic wave attenuation properties of hydrate-bearing sediments.

This work has shown that electrical conductivity measurements can help us detect both hydrate formation and hydrate dissociation fronts. Our results show how the dynamic processes of

hydrate formation and dissociation can be captured using complex conductivity. These insights are useful during monitoring gas production from hydrates.